CHANGES IN PACIFIC CLIMATE VARIABILITY IN RESPONSE TO FRESHWATER DISCHARGE IN THE NORTH ATLANTIC

Master's thesis

Faculty of Science
University of Bern

presented by
Siswanto
2010

Supervisor:
Prof. Dr. Thomas F. Stocker

Co-supervisor:
PD. Dr. Christoph C. Raible
Climate and Environmental Physics, Physical Institute, and Oeschger Center for Climate Research, University of Bern

Advisor:
Prof. Dr. Martin Grosjean
Graduate School of Climate Science, and Oeschger Center for Climate Research, University of Bern

July 2010

Acknowledgements

This thesis project would not have been possible without the support of many people. The author wishes to express his gratitude to his supervisor, Prof. Dr. Thomas F. Stocker, for interesting and stimulating discussions, whose encouragement, guidance and support from the initial to the final level enabled him to develop an understanding of the subject and extensive insights throughout the work, PD. Dr. Christoph C. Raible who was abundantly helpful and offered invaluable assistance, support and guidance for keeping him on track during the whole year. Special thanks for Prof. Dr. Martin Grosjean, the Studies Director of Graduate School, who gave advice and understanding while the author belonged to the Graduate School. Deepest gratitude is also due to the members of the modeling and climate variability group, Dominik Hofer, Thomas Frölicher, and Flavio Lehner, without whose knowledge and assistance, the technical problems would not have been successfully solved. Special thanks also to all my graduate friends in the Graduate School of Climate Sciences, especially KUP group members for sharing the literature and invaluable assistance. Not forgetting to his best colleague "The Dungeon Crew" who always been there in cell B15, Flavio, Sofie and Claudia.

The author would also like to convey thanks to the ESKAS, the Federal Commission for Scholarships for Foreign Students (FCS), for providing him a 2-year grant and the financial means during his study in Switzerland. He is thankful to his institute, National Agency for Meteorology, Climatology and Geophysics of Republic of Indonesia, who permitted him out of work during his study.

The author wishes to express his love and gratitude to his beloved families for their understanding and endless love, through the duration of his studies. This thesis is dedicated to his Mom, who had passed away when the author was completing his study. Peace always be upon her.

Contents

Abstract

The Atlantic Meridional overturning circulation (AMOC) is widely believed to affect climate. The links between AMOC variability and climate system impacts, especially those relating to climate variability, sea ice, marine ecosystems, the ocean carbon budget and sequestration, and regional and global sea level, has been broadly studied. This study investigates the climate variability changes in the Pacific's basin in regard to the resumption process of the AMOC due to freshwater hosing experiments using a comprehensive coupled climate model. A freshwater perturbation of 2 Sv is applied to the North Atlantic between 50°N - 70°N leading to a substantial weakening of AMOC and a two-phase recovery of the AMOC. Period A denotes the period when the maximum perturbation is applied and results in the AMOC nearly collapsed, whereas two-phase recovery is denoted by Period B and C. Period A exhibits cooling of the North Pacific, particularly along the oceanic frontal zone, and deepening of the wintertime Aleutian Low, southward displacement of the Pacific's Inter Tropical Convergence Zone (ITCZ), consistent with paleoclimate reconstructions. The analysis identifies both oceanic and atmospheric pathways from the Atlantic to the North Pacific as well as an atmospheric teleconnection remotely from the tropical Pacific to the extratropical Northern Hemisphere. The oceanic teleconnection via the Bering Strait throughflow contributes substantially to the North Pacific cooling. This cooling is also suggested to be remotely driven from the tropics through an "atmospheric bridge" and air-sea interaction mechanisms. In addition, the atmospheric bridge from the tropical North Atlantic is important to lead changes of the mean state of sea surface temperature (SST) in the eastern tropical Pacific. This basic state change is associated with a shallowing thermocline and enhanced vertical stratification of the equatorial Pacific ocean, which in turn leads to an intensification of the seasonal cycle of tropical SST and changes in ENSO frequency and its characteristics. Besides finding the changes on the ENSO variability and its properties, this study revealed changes on the 2^{nd} leading mode of North Pacific SST, as well as the enhanced AO-like and PNA patterns in the Northern Hemisphere geopotential field. The analysis showed that changes in the North Pacific climate mode are associated with the shifting into high frequency of ENSO.

Chapter 1

Introduction

1.1 Background of knowledge

The Intergovernmental Panel on Climate Change (IPCC) has reported that abrupt climate change, such as the collapse of the West Antarctic Ice Sheet, the rapid loss of the Greenland Ice Sheet or large scale changes of ocean circulation system are not considered likely to occur during the 21^{st} century. However, the occurrence of such changes becomes increasingly more likely as the perturbation of the climate system progresses (*IPCC*, 2007). One example of abrupt climate change is the potential collapse, or shut-down of the Gulf Stream, which in turn can influence the meridional overturning circulation in the North Atlantic (AMOC). The AMOC has been the subject of many studies which focused on its role for the past (*Stocker*, 2000), as well as for future climate change (*IPCC*, 2007). A consistent result from climate model simulations is that if the density of surface waters in the North Atlantic decreases due to warming or reduction in salinity, it increases the surface buoyancy. The reduction in salinity can be caused by a large freshwater flux anomaly from melting land ice or pursuant to an intensification of the hydrological cycle. Moreover, increasing the surface buoyancy can inhibit deep water formation in the North Atlantic. A strong and sustained reduction in the North Atlantic Deepwater Formation (NADW), could induce a more substantial reduction, or even more, a complete shut-down of the AMOC.

Paleoclimate studies and proxy evidence show that the AMOC plays an important role in the millennial climate variations during the last glacial period. These are hints that sudden changes of the AMOC cause large and abrupt climate changes over many parts of the globe during the last glacial and interglacial period. The effects of an AMOC reduction to the climate system have received considerable attention in the last decade. *Rooth* [1982] and *Broecker et al.* [1985] are among the first to propose a connection between rapid climate changes and the AMOC. Their idea is supported by a number of paleoclimate studies indicating that reduced production of North Atlantic deepwater is accompanied by stadial conditions in the North Atlantic region (*McManus et al.*, 2004; *Denton et al.*, 2010). Indeed, during the last glacial period, the climate passed through several rapid transitions of stadial and interstadial states and the ocean-atmosphere system underwent dramatic and abrupt changes with widespread consequences (*Stocker et al.*, 2001). Oxygen isotope measurements in Greenland ice cores demonstrate that a series of rapid warm and cold oscillations called Dansgaard-Oeschger (DO) events punctuated the last glaciation (*North GRIP Mem-*

bers, 2004). A comparison of stable-isotope ($\delta^{18}O$) records from the Byrd Station (West Antarctica) ice core and the Greenland Ice Sheet Project 2 (GISP2) and Greenland Ice-core Project (GRIP) ice cores, revealed that the Northern Hemisphere Younger Dryas (YD) was preceded, by about 1000 years, by a Southern Hemisphere "Antarctic Cold Reversal" (ACR) (*Blunier et al.*, 1998). *Blunier and Brook* [2001] demonstrated that the relationship observed between the ACR at Byrd and the YD in Greenland is repeated for virtually all the stadial-interstadial climate-change events over the last 90 kyr. The archetype of this kind of climate change is the beginning of the YD at 12.9 kyr, which is known to have followed a major pulse of meltwater from the Laurentide ice sheet into the North Atlantic (*Broecker and Denton*, 1989). Those paleo records from the Greenland ice core revealed evidence that DO and YD events are associated with substantial changes in the AMOC (see *Dansgaard et al.*, 2003 and *McManus et al.*, 2004). Air temperature, SST and salinity variations in the North Atlantic have been associated with major changes in the thermohaline circulation. A core from the margin of the Faeroe-Shetland channel covering the last glacial period reveals numerous oscillations in benthic and planktonic foraminifera, oxygen isotopes and ice-rafted detritus (*Rasmussen et al.*, 1996). These oscillations correlate with the DO cycles, showing a close relationship between the deep ocean circulation and the abrupt climatic changes of the last glaciation. Warm episodes were associated with higher SST and the presence of oceanic convection in the Norwegian-Greenland Sea. Cold episodes were associated with low SST and salinity and no convection in the Norwegian-Greenland Sea (*Rasmussen et al.*, 1996). Evidence from marine sediment shows that NADW decreased during times when the Greenland was cold, and increased rapidly during Greenland warming events (see e.g., *Bond et al.*, 1993). Enhanced ventilation during cold periods is also suggested by ocean sediments from the Santa Barbara basin (*Behl and Kennett*, 1996) and the Northeast Pacific (*Lund and Mix*, 1998).

Several studies implied that during colder stages in Greenland, changes in other parts of the climate system occurred: the Atlantic intertropical convergence zone (ITCZ) was displaced southward (*Schmidt et al.*, 2006), Indian and Asian summer monsoons were weakened (*Wang et al.*, 2001), and the eastern equatorial Pacific was colder (*Kienast and McKay*, 2001). Moreover, the Pacific ITCZ was displaced southward (*Leduc et al.*, 2007) as well as the Walker circulation weakened (*Stott et al.*, 2002). Outside the tropics, large SST variations closely related to the Greenland records are reported in different parts of the North Pacific (*Kienast and McKay*, 2001; *Okumura et al.*, 2009). For the atmospheric circulation, recent studies of lake sediments show decreased (increased) moisture availability in the western (central) part of southern Alaska during the Younger Dryas, implying that the Aleutian Low was stronger in comparison to present-day conditions (see *Hu et al.*, 2006 for the analysis of lake sediments from southwestern Alaska).

In spite of this wealth of high-quality paleoclimate information, there are major limitations that seriously hamper progress (*Stocker et al.*, 2001). The most important one is the relatively poor database outside the North Atlantic region. In particular, the tropics are not well represented although probably important processes for abrupt change may originate there. Practically, nothing is known about the long-term variability in the tropics; it is not known whether the El Niño-Southern Oscillation (ENSO) cycle persisted in the glacial, or whether the tropics may have resided in a phase-locked state similar to La Niña. It would also be ex-

tremely important to know whether the statistics of the ENSO cycle are subject to long-term changes over the millennia, as modeling suggests (*Clement et al.*, 1999). Thus, a complete understanding of the mechanisms of abrupt change requires inclusion of processes at both low and high latitudes, as well as the potential for feedbacks between them (*Clement and Peterson*, 2008).

The currently most promising hypothesis regarding the characteristic surface temperature pattern associated with abrupt climate change is the "bipolar seesaw" (*Stocker and Johnsen*, 2003; *EPICA Community Members*, 2006), which is based on the observation that the AMOC causes a substantial south-to-north heat transport in the Atlantic Ocean. The concept of the thermal bipolar seesaw, in which the Southern Ocean integrates the North Atlantic signal, has solved the controversy of lead and lag between climate signals in the northern and southern hemispheres (*Stocker and Johnsen*, 2003). Based on this, it has been argued that a shutdown of the AMOC affects the coupled atmosphere-ocean climate system on a global scale (*Stocker et al.*, 2007). This hypothesis is supported by many modelling studies using coupled GCM that showed the response of global climate to the anomaly of AMOC (*Stouffer et al.*, 2006). In the models, when the AMOC is forced to slow down, it has been associated with a reduction in northward heat transport that causes sea surface temperatures (SST) to decrease over the North Atlantic, and to increase over the tropical South Atlantic (*Dong and Sutton*, 2002). In general, cooling surface air temperature, which is much dominated in the Northern Hemisphere and a slightly warming of the Southern Hemisphere, leading to maximum global cooling of 0.9°C (*Vellinga et al.*, 2002). The surface salinity of the northern North Atlantic appeared higher than that of the northern North Pacific (*Manabe and Stouffer*, 1988). The weakening of the AMOC also results in a southward shift of the ITCZ over the Atlantic and Pacific, an El Niño-like pattern in the southeastern tropical Pacific, and weakened Indian and Asian summer monsoons through an airsea interactions (*Zhang and Delworth*, 2005). The results are consistent with paleo-evidence of the global synchronization of millennial-scale abrupt climate change.

Concern to the Pacific basin, the remote response to the North Atlantic abrupt changes during lowering AMOC could be seen in a strong cooling that occurs along the North Pacific oceanic frontal zone (*Stocker et al.*, 2007) and intensification of the wintertime Aleutian Low which establishes quickly within a few decades (*Okumura et al.*, 2009). Through additional experiments with CCSM2 and CAM2, *Okumura et al.* [2009] proposed the mechanisms for both oceanic and atmospheric teleconnections. For the oceanic teleconnection, part of the freshwater applied to the North Atlantic flows through the Bering Strait into the North Pacific, where the anomalously cold and fresh water is advected by mean ocean currents. The resulting extratropical oceanic cooling strengthens the north easterly trade winds, reducing the tropical North Pacific SSTs and shifting the Pacific ITCZ southward through the wind-evaporation-SST feedback, and therefore, suggesting a strong connection between the AMOC and North Pacific climate. Due to the rapid rate of North Pacific SST changes associated with the North Atlantic climate anomalies (*Kienast and McKay*, 2001), atmospheric teleconnections are likely to have played a crucial role in the AMOC-North Pacific linkage during the last glacial period (*Okumura et al.*, 2009), however, oceanic connections cannot be ignored. *Mikolajewicz et al.* [2007] showed that the atmospheric circulation anomaly in their water-hosing experiment projects strongly on the leading internal mode over the North Pa-

cific sector, which represents changes in the strength and position of the Aleutian Low. They suggest that the Aleutian Low response is a combination of remote influence from the Atlantic and local air-sea interactions in the North Pacific. Meanwhile, *Hu et al.* [2007] showed that a part of the freshwater flux anomaly applied to the North Atlantic is transported into the North Pacific through the Bering Strait by reversing the hydraulically-controlled throughflow. This inflow of cold and fresh Arctic water may have a significant impact on the heat and salinity balance in the North Pacific through ocean teleconnections.

Other studies, which are addressing the climate in the Pacific region, had revealed that the existence of the present-day tropical Pacific cold tongue complex and the annual cycle in the eastern equatorial Pacific is partly controlled by the strength of the AMOC (*Timmermann et al.*, 2007). When the AMOC slows down the amplitude of the equatorial Pacific cold tongue annual cycle is reduced, and the ENSO cycle is intensified. In an ensemble of coupled model simulations, *Dong and Sutton* [2002] showed that an intensification of El Niño was systematically initiated 6-7 years after the AMOC was abruptly slowed. Lately, *te Raa et al.* [2009] showed that the modeled connection between AMOC and ENSO depends strongly on the frequency and/or the amplitude of the AMOC variations. In addition, multidecadal SST variations of the AMOC have been suggested also as a possible explanation for low-frequency ENSO variability in the tropical Pacific (*Timmermann et al.*, 2007). However, the AMOC-ENSO connection is still not fully understood. AMOC variations on different time scales and an AMOC collapse are associated with entirely different responses in the Pacific Ocean.

Stocker et al. [2007] and *Renold et al.* [2010] used the coupled atmosphere ocean model CCSM3 to perform a control and a series of sensitivity experiments with an artificial freshwater discharge in the North Atlantic. The finding in their studies is a strong reduction of AMOC and a warming in the South Atlantic and a cooling in the North Pacific. The cooling in the North Pacific remains unclear and left some questions such as:

- What is the impact of this cooling to the atmosphere-ocean coupled modes such as the Pacific Decadal Oscillation and ENSO?
- Which processes and mechanisms are involved and play a role in those climate modes, whether it is an atmospheric tropical-extratropical connection (atmospheric bridge) or alternatively through ocean dynamics such as the ocean Kelvin and Rossby waves?
- How does the change in sea surface temperatures affect the ocean circulation in the Pacific?

Therefore, it is important to investigate the possible changes of Pacific climate variability such as the ENSO, PDO, and other teleconnection patterns in the different periods in response to freshwater discharge in the North Atlantic.

1.2 Pacific Climate Variability

The Pacific Ocean exhibits prominent SST variations on time scales that range from a few years to decades. This variability is classified into two frequency bands: inter-annual variations and decadal variations. Therefore, this study will follow this classification and present

results of the Pacific inter-annual variability and Pacific decadal variability, separately.

1.2.1 Pacific Inter-Annual Variability, El Niño-Southern Oscillation (ENSO)

Within the Pacific basin, inter-annual variability is dominated by El Niño Southern Oscillation (ENSO) which has its largest signature in the tropics, particularly in the eastern tropical Pacific (*Giese and Carton*, 1999). ENSO is the most important global coupled ocean-atmosphere phenomenon with worldwide impacts. ENSO is not periodic but has a characteristic time scale of 3-8 years. The ocean part is the El Niño phenomenon, which has long been known to fishers living at the west coast of equatorial South America where during such events the water was warm and the fish populations were reduced. El Niño usually occurred around Christmas (El Niño means "the Child"). The atmospheric part is the Southern Oscillation (SO) which has been discovered by Sir Gilbert Thomas Walker (1923) (see *Katz*, 2002). SO is a large-scale pressure oscillation in the tropical Pacific. The tropical atmosphere has a strong zonal asymmetry in diabatic heating caused by differences in heat distribution between ocean and land. The air follows a closed circulation in the zonal and vertical directions referred to as Walker Circulation.

During normal conditions, strong up-ward motion (low pressure, increased precipitation rate) over the maritime-continent region is compensated by downward motion (high pressure, dry) over the eastern Pacific basin (see Figure 1.1). The surface pressure difference between east and west is strongly associated with trade winds (winds that flow toward the equator) which push the warm water pool towards the west. Along the equatorial Pacific, during this normal condition, the basic state of averaged sea surface temperature (SST) has been higher over Indonesia (western basin) and colder in the eastern Pacific (see *Bjerknes*, 1969; *Ramage*, 1975; *Sadler*, 1980) as well as along the South American coast. This cold anomaly is maintained by upwelling since the oceanic Ekman transport associated with the easterly wind drives water to the right (northwards) in the Northern Hemisphere and to the left (southward) in the Southern Hemisphere. This results in a westward ocean flow and a divergence, compensated with upwelling from below bringing cold water upward. The thermocline slope moves upward from west to east and sea level moves downward from west to east.

During El Niño (Figure 1.1), the Walker circulation and precipitation are shifted toward the east of Pacific and surface pressure gradient between east and west is weaker and reduces the trade winds. The warm pool approaches the eastern Pacific and the thermocline slope is smaller than during the normal conditions. The opposite state of El Niño is La Niña. La Niña is more comparable to the normal condition. However, the warm pool is further west than usual. The trade winds blow from east to west across the coastal waters of the eastern Pacific and drag the warm surface waters of the equatorial Pacific with them. The thermocline has a larger slope than during the normal condition.

El Niño and La Niña appear primarily as a result of interactions between the tropical oceans and the overlying atmosphere (*Philander*, 1990) and thus produce SST and heat content anomalies that are concentrated in the tropics. This "air-sea interaction" is accompanied by the circulation of large internal waves (waves that have their peak in the interior of the ocean)

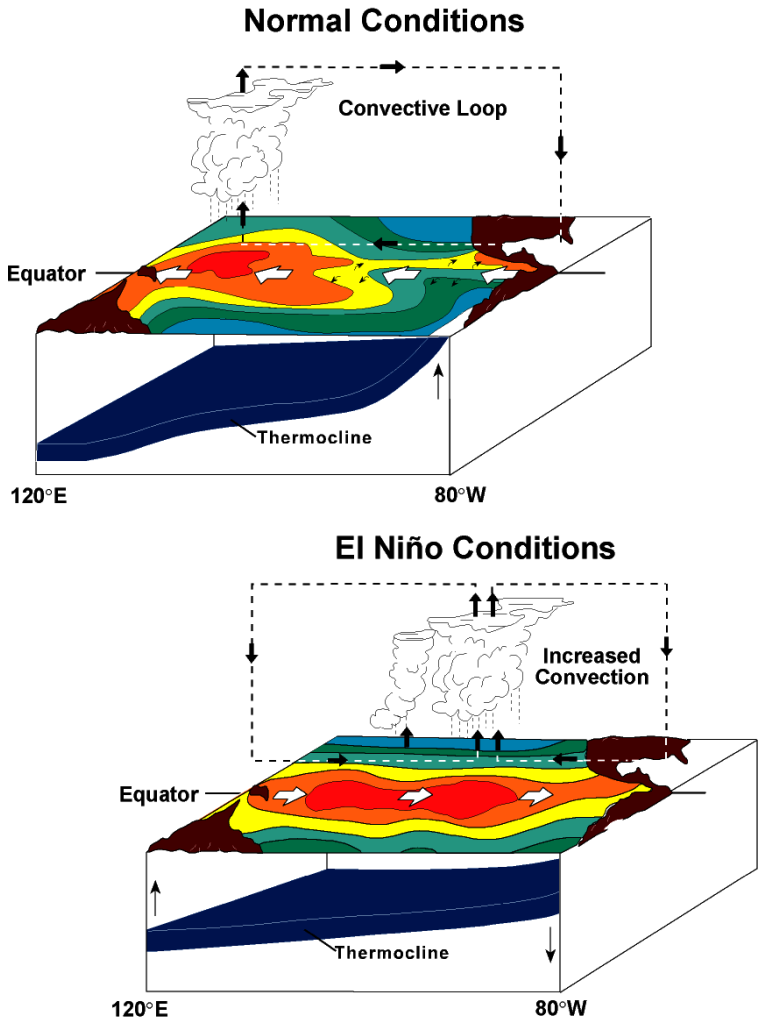

Figure 1.1: Schematic of normal and El Niño conditions in the equatorial Pacific (figure from *www.pmel.noaa.gov*)

across the Pacific ocean, mainly in the equatorial region. These internal waves are referred to as Kelvin and Rossby waves. Kelvin waves travel eastward along the equator, whereas the Rossby waves travel westward and are a result of changes that the Kelvin waves introduced to the area. Rossby waves travel up to about three times slower than Kelvin waves. Further explanations of these two internal waves can be found in *Gill* [1982].

Various studies using observational data revealed that ENSO is an annual to inter-annual phenomenon of basin-scale, seasonal air-sea interaction modes in the tropical Pacific (e.g.*Barnett*, 1977, *Spencer et al.*, 2007,*Toniazzo*, 2006). Although inter-annual variability has its largest expression in the Tropics, some studies have explored significant inter-annual variations in the North Pacific associated with ENSO events (e.g., *Wallace and Gutzler*, 1981; *Alexander*, 1992; *Zhang*, 1996) as well as its contribution to the spatial patterns of decadal ENSO-like variability (*Vimont*, 2005) which will be discussed in the following paragraph. Inter-annual

variability in the North Pacific is often described as a result of atmospheric teleconnection patterns and has recently been explained as resulting from an "atmospheric bridge" by *Lau and Nath* [1996]. The atmospheric bridge mechanism is a well known explanation of how ENSO affects the northern extratropical oceans which are not only felt in the surface heat flux, but also dynamically through Ekman transport (*Jin and Kirtman*, 2010) and is primarily related to the excitation of the Rossby wave train (*Luo and Alexander*, 2007).

Additionally, there are several seasonal to inter-annual variability phenomenon that operate in the Pacific ocean such as Madden Julian Oscillation (MJO), Quasi Biennial Oscillation, and Monsoon system, which will not be discussed in this study.

1.2.2 Pacific Decadal Variability

Observed tropical Pacific decadal variance is dominated by variability with a spatial structure that bears a strong resemblance to the inter-annual ENSO phenomenon in both the tropics and midlatitudes (*Trenberth*, 1990; *Zhang et al.*, 1997; *Vimont*, 2005). Based on this similarity, *Zhang et al.* [1997] has labeled tropical Pacific decadal variability as " ENSO-like" variability (*Vimont*, 2005), while *Mantua et al.* [1997] labeled this structure of decadal variability as the Pacific Decadal Oscillation (PDO).

The Pacific Decadal Oscillation (PDO) is one of the two leading patterns of SST variability that pronounces in the Pacific's climate state. The PDO pattern is marked by widespread variations in Pacific basin and North American climate with two different regimes warm and cold as defined by ocean temperature anomalies in the northeast and tropical Pacific Ocean (Figure 1.2). A warm PDO means SSTs in central Pacific Ocean are warmer with cool water in the west, north and south. During warm or positive PDO, cold water in central Pacific supports a trough over central Pacific, and warm water along eastern North Pacific supports a ridge over the west coast of North America. A warm PDO may result in more El Niños, more precipitation, and fewer typhoons (*Mantua et al.*, 1997). During the cool phase, the central waters are cool and the peripheral waters are warm. Warm water in the central Pacific supports a ridge over the central Pacific and a strong Pacific Jet. Cool water along the west coast supports a trough over the west coast of North America and a mild eastern United State's winter. A cool PDO result in cool air and less precipitation, particularly in the western United States (*Mantua et al.*, 1997). During the last three decades of the 20th century, the PDO showed a warm phase. It has been argued that a new regime shift occurred in the late 1990s in the North Pacific associated with the PDO (*Peterson and Schwing*, 2008).

Some studies suggested a linkage between PDO and ENSO and described the PDO as a long-lived El Niño-like pattern of Pacific climate variability (*Zhang et al.*, 1997; *Mantua et al.*, 1997). There are at least two main characteristics, which distinguish the PDO from ENSO. First, while ENSO is an inter-annual phenomenon, the PDO has a preferred time scale of 20 to 30 years during the last century(*Mantua et al.*, 1997; *Minobe*, 1997). Second, the SST pattern related to PDO are dominant in the North Pacific/North American sector, while secondary signatures exist in the tropics - the opposite is true for ENSO.

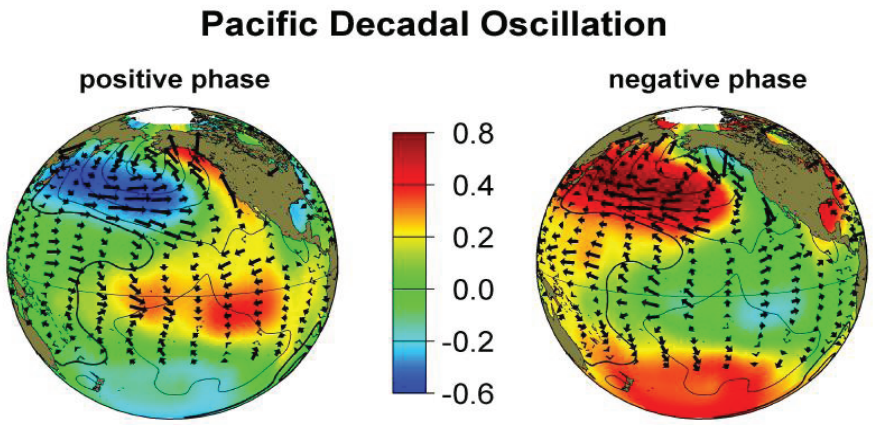

Figure 1.2: Pacific Decadal Oscillation. Typical wintertime sea surface temperature (colors), sea level pressure (contours), and surface wind stress (arrows) anomaly patterns during positive and negative phases of the Pacific Decadal Oscillation (PDO). Temperature anomalies (colors) are in degrees Celsius (*Mantua et al.*, 1997). (figure from *www.usgcrp.gov/.../ocp2006/ocp2006-hi-water.htm*)

The latest observational and coupled modeling studies tend to indicate an inter-basin teleconnection over the North Atlantic and the North Pacific associated with both atmospheric and oceanic variability (*Li et al.*, 2009). However, there are several hypotheses providing an explanation of causes and origins of Pacific decadal variability (*Wu et al.*, 2003). One hypothesis suggests that Pacific decadal variability is generated primarily within the North Pacific (*Latif and Barnett*, 1996; *Barnett et al.*, 1999) and may teleconnect to the tropics via the atmosphere (*Barnett et al.*, 1999; *Pierce et al.*, 2000) and/or ocean (see e.g.,*McCreary and Lu*, 1994; *Liu and Philander*, 1995; *Lysne and Deser*, 2002). Another hypothesis suggests that low-frequency variability in the Pacific is generated over the entire extratropical-tropical climate system in conjunction with feedbacks associated with extratropical-tropical interactions in the ocean by the slow meridional overturning circulation in the upper ocean and/or in the atmosphere via an atmospheric bridge (*Gu et al.*, 1997; *Kleeman et al.*, 1999). It has also been hypothesized that Pacific decadal variability is intrinsically tropically driven (*Tziperman et al.*, 1997; *Knutson and Manabe*, 1998; *Schneider and Cornuelle*, 2005) and may affect the midlatitudes through atmospheric teleconnections (*Trenberth*, 1990; *Graham*, 1994). Finally, the low-frequency variability in the Pacific may also be a consequence of the reddening effect of atmospheric stochastic forcing by the ocean (*Hasselmann*, 1976; *Frankignoul and Hasselmann*, 1977; *Saravanan and McWilliams*, 1997; *Weng and Neelin*, 1998).

So far, the scientific understanding has revealed that the Pacific decadal variability may be composed of two different modes, most notably, a decadal to bidecadal tropical Pacific (ENSO-like) and the North Pacific multidecadal mode (*Zhang et al.*, 1997; *Nakamura et al.*, 1997; *Minobe*, 1997; *Wu and Liu*, 2003). Furthermore, *Wu and Liu* [2003] propose that the ENSO-like bidecadal tropical Pacific mode (TPM) and multidecadal North Pacific mode (NPM) are generated mainly internally within the tropical and North Pacific, respectively. Other studies reveal that the atmospheric variability in the North Pacific is expected as the

origin of the stochastic forcing on ENSO, which mediated to the tropics via a subtropical air-sea interaction mode (*Chiang*, 2009). The extratropical impact on tropical climate or vice versa is accomplished mainly through the atmosphere (Hadley circulation). Changes in the extratropics can also impact the tropical climate through the upper ocean subtropical gyre at decadal and longer time scales.

Despite observational and theoretical studies, modeling studies have identified many mechanisms that may produce decadal variations in the tropical Pacific, including chaotic and stochastic variability of ENSO (*Thompson and Battisti*, 2001; *Timmermann et al.*, 2003), variations of tropical or ENSO dynamics (*Yukimoto et al.*, 1996; *Vimont*, 2005), and remote forcing from the midlatitudes (*Gu et al.*, 1997; *Vimont et al.*, 2003). Later, *Wu et al.* [2007] reveal that recent tropical Pacific decadal variability tends to be associated with extratropical North Pacific through relay teleconnections of a fast coupled ocean-atmosphere bridge and a slow oceanic tunnel. These studies indicate the possibility of multiple origins and mechanisms for decadal climate variability in the Pacific. However, the causes and origins of the Pacific's climate variability are difficult to identify directly from observations, since there is a difficulty in separating out all the complex feedbacks.

1.2.3 Pacific Ocean Circulation

The Pacific Ocean is the largest ocean basin on Earth. It extends from the Arctic in the north to the Southern Ocean in the south, bounded by Asia and Australia in the west, and the Americas in the east. The Pacific, including adjoining seas, has an area of about 64,186,300 square miles (166,241,700 square km). It makes up almost 33% of the earth's total surface and 46% of its water surface, and is larger than all land areas combined. The ocean is commonly divided at the Equator into the North and the South Pacific. The North Equatorial Current flows westward in the general area of the northeast trades, and the South Equatorial Current follows a similar path in the region of the southeast trades. Between these two, the weaker North Equatorial Countercurrent sets toward the east, just north of the equator. As a result, warm equatorial water is constantly transported poleward along the Asian and Australian coasts, while cold water is flowing toward the equator along the coasts of North and South America. Thus, the currents have distinct climatic effects on nearby continents. In some areas, such as the coast of Chile and Peru, they cause a cooling, whereas in others, such as southern Japan, they lead to warmer dominate conditions. In the North Pacific, the Kuroshio carries large quantities of warm tropical water to higher latitudes, and then curves toward the east as a major part of the general clockwise circulation in the Northern Hemisphere. As it does so, it widens and slows, continuing on between the Aleutians and the Hawaiian Islands, where it becomes known as the North Pacific Current. The northern branch of the North Pacific Current curves in a counterclockwise direction to form the Alaska Current, which generally follows the coast of Canada and Alaska.

The surface temperature of the Pacific Ocean can vary on all time scales. Much of the short-term temperature variation is directly induced by the sun, including the diurnal and seasonal cycle. The wind and pressure systems of the Pacific conforms closely to the planetary system, i.e., the patterns of air pressure and the wind patterns that develop due to thermal forcing in

the atmosphere of the Earth and modified by Coriolis.

Due to radiation from the sun, the ocean and atmosphere are heated and transport on average roughly the same amount of heat from low to high latitudes. However, this is achieved in a remarkably different manner. The atmosphere transports heat, mainly by transient eddies in the middle latitudes, whereas, the ocean heat transport is achieved mainly by boundary currents, large gyres (wind-driven to a large extent) and the vertical overturning of the ocean. Since the climate variability is not only driven by, and occurs in, the atmosphere, the ocean circulation plays an important role in moderating and modifying the atmospheric climate.

As part of global ocean conveyor belt or global thermohaline circulation (Figure 1.3), a fraction of the deep waters in the Southern Ocean flows into the Pacific Ocean, where they return to the surface. The surface waters then flow through the Indian Ocean, around Africa, and back to the tropical Atlantic, thus closing the loop of the conveyor belt. Most models of the thermohaline circulation involve sinking in the northern Atlantic, and rising motion everywhere else, but in reality, it is not known where the cold water rises back to the surface. The ocean conveyor circulation in the North Atlantic is referred to as the Atlantic meridional overturning circulation, whereas in the Pacific is referred to as Pacific meridional overturning circulation. It is a feature of both the thermohaline and wind-driven components of the oceanic circulation. The wind-driven circulation penetrates to a depth of a few hundred meters at most, while at greater depths, the oceanic thermal structure depends on processes associated with the depth thermohaline circulation. Hence these two components are complementary. Jointly, they determine the oceanic thermal structure and satisfy the constraint of balanced oceanic heat budget. That constraint determines the depth of thermocline such that the gain of heat in low latitudes balances the loss heat in low latitudes (*Boccaletti et al.*, 2004; *Barreiro et al.*, 2008). In response to a change in the loss of heat, the ocean adjusts by

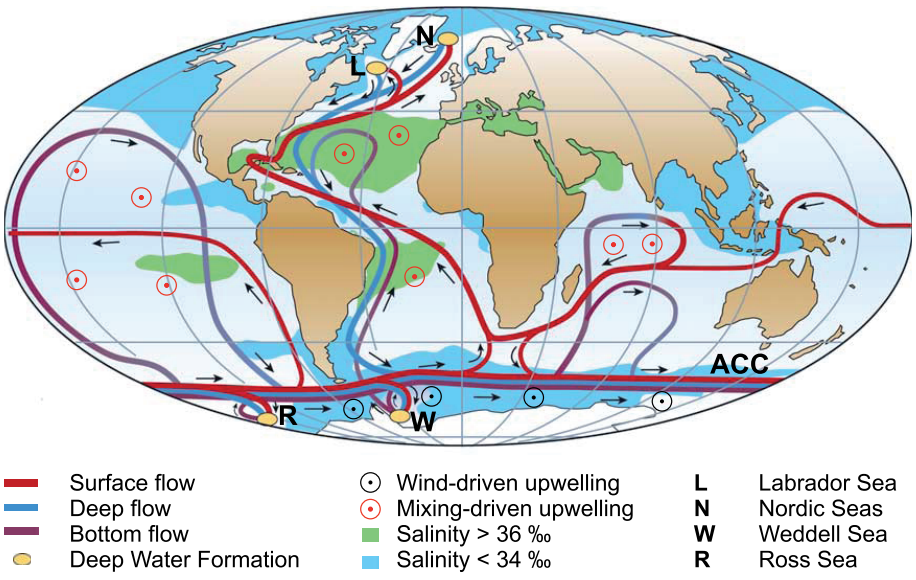

Figure 1.3: Simplified Conceptual Model of the Thermohaline Circulation (figure from *Kuhlbrodt et al.*, 2007)

changing the depth of the thermocline.

Within the North Pacific Ocean, there are no deep water sources and the intermediate water sources are weak (*Talley*, 2008). Therefore, the North Pacific is actively ventilated to no more than about 2000 m depth. Circulation below that depth must be thermohaline due to remote deep water formation in the southern ocean and Atlantic (*Talley*, 2008). The wind forcing for the North Pacific consists of westerlies at latitude north of about 30°N, and easterly trades to the south. The ITCZ is centered at about 10°N. The mean winds create Ekman divergence between 5°N and 15°N. These patterns drive Sverdrup transport, which is northward in Ekman divergence regions and southward in Ekman convergence regions. Because the return flow for this interior ocean transport must be in western boundary currents, this produces cyclonic circulation in the north (subpolar gyre), anticyclonic at the mid-latitude (subtropical gyre), and meridionally narrow cyclonic circulation centered at 10°N. The western boundary currents associated with these three gyres are: East Kamchatka current (Oyashio), Kuroshio, and Mindanao current. In addition, the dominant pattern of atmospheric circulation north of 30°N is associated with the Aleutian Low. Further descriptions can be found in *Talley* [1988], *Talley et al.* [1995],*Talley* [2003], and *Talley* [2008].

1.2.4 Freshwater hosing experiment over the North Atlantic and its impact to Pacific Ocean and Climate Variability

Within the North Atlantic ocean, high density of the surface water in deep water formation area is crucial to initiate the deep water formation. Densification is achieved through either cooling or increasing salinity, or both. The existence of the high salinity surface waters which are transported from the south and hence cooling, induce densification. Changes of the surface water density around the NADW formation region are naturally obtained when the freshwater budget of the North Atlantic is changed through precipitation/evaporation or through ice melting and formation. In order to compensate an excess of precipitation and runoff over evaporation, the winter surface waters from which the deep water formed would have to be cooled by an additional 1.4°C (*Broecker*, 1997). But even if this were satisfied, the salt budget would be disrupted and there would be a mismatch between re-densification and de-densification of the deep sea. However, this would trigger a reorganization of the global circulation system. In freshwater hosing experiments performed with climate models of different complexity, the ocean is perturbed with a freshwater flux. Many studies showed that the AMOC is sensitive to fresh water input (*Manabe and Stouffer*, 1988).

A wide range of modeling studies had demonstrated a weakened AMOC in response to freshwater forcing at North Atlantic Deep Water (NADW) formation sites (e.g., *Stommel*, 1961; *Weaver et al.*, 1993; *Stocker et al.*, 2007, *Yoshimori et al.*, 2010, *Renold*, 2007; *Renold et al.*, 2010); specifically, an increased freshwater flux creates more stably stratified surface water, which reduces deep water formation and its concomitant meridional heat transport, producing a cooling of Northern Hemisphere climate. Accordingly, by applying freshwater discharge experiments in the climate models, the picture of interhemispheric coupling to investigate aspects of the bipolar seesaw can be examined. One of the aims of the freshwater hosing experiments is to provide a firmer foundation of hypotheses regarding the behavior of the

AMOC during the last ice age (*Stocker et al.*, 1992; *Vellinga and Wood*, 2002; *Renold et al.*, 2010).

In the case where the North Atlantic surface waters are freshened, the AMOC and associated northward oceanic heat transport is weakened (*Stouffer et al.*, 2007). In the Antarctic surface freshening case, the AMOC is mainly unchanged with a slight weakening toward the end of the integration. This weakening is associated with the spreading of the fresh sea surface anomaly from the Southern Ocean into the rest of the World Ocean. There are two possible mechanisms that may be responsible for such a weakening of the AMOC. First, the sea surface salinity (SSS) contrast between the North Atlantic and North Pacific is reduced. And, second, when freshwater from the Southern Ocean reaches the high latitudes of the North Atlantic Ocean, the sinking of the surface waters is reduced or even stopped, leading to the weakening of the THC (*Stouffer et al.*, 2007).

Shutdown of the thermohaline circulation by freshwater hosing is usually only temporary in sophisticated climate models: Once hosing ends, the circulation recovers in temporal scale of decades to centuries. In a model inter-comparison study on freshwater hosing experiments, *Stouffer et al.* [2006] showed that a few experiments reveal no resumption of the MOC for a strong freshwater forcing and with a resumption in most of them with a significant overshooting of the AMOC by more than 30% compared with the control experiment. In the glacial freshening experiments, *Otto-Bliesner and Brady* [2010] showed that the less dense freshwater provides a lid on the ocean water below, suppressing ocean convection and interaction with the atmosphere above and reducing the AMOC. This is the case, whether the freshwater is added directly to the area of convection south of Greenland or transported there by the subtropical and subpolar gyres when added to the Gulf of Mexico.

The AMOC reduction is weaker for the smaller freshwater forcing, but is not linear with the size of the freshwater perturbation. After the AMOC is suppressed, it is suggested that the intermediate water formation tends to resume in the North Pacific (*Timmermann et al.*, 2005; *Krebs and Timmermann*, 2007; *Mikolajewicz et al.*, 1997). Regarding the MOC recovery, it has been argued also that it depends strongly on the through-flow of the Bering Strait (*Hu et al.*, 2008). *Hu et al.* [2008] implied that the recovery is at least a century earlier in an open Bering Strait than if the Bering Strait is closed. From this experiment, it seems that Pacific ocean is somehow linked to the AMOC recovery and react to the cooling in the North Atlantic. The analysis of the sensitivity experiments of the coupled atmosphere ocean model CCSM3 with artificial freshwater discharges in the North Atlantic (*Stocker et al.*, 2007; *Timmermann et al.*, 2007; *Renold et al.*, 2010) showed a strong cooling of the North Pacific. However, the North Pacific cooling leaves some issues i.e., whether the change in sea surface temperatures affects the ocean circulation in the Pacific and how the atmosphere-ocean coupled modes in the Pacific basin will behave in response to freshwater discharge in the North Atlantic are among the interesting questions.

1.3 Objective

This study will analyze the Pacific climate response to the North Pacific cooling due to an AMOC slow down induced by freshwater discharge in the North Atlantic. The study explores a potential inter-annual to inter-decadal change of the Pacific's climate variability using state-of-the-art of CCSM3 coupled model. The freshwater hosing sensitivity experiment FN20 (without salt compensation) for 1000 years run is presented with analysis of three distinct periods. Period A covers model years 50-210, Period B: 450-900 and Period C covers model years 950-1000.

This thesis will address questions such as:

- How stable is the Pacific's climate variability response to a rapid weakening of the AMOC and its three quasi-stable periods of resumption in terms of its climate pattern, magnitude, seasonality, and temporal evolution?
- What is the origin of North Pacific cooling during AMOC slow down?
- What is the impacts of this cooling to the inter-annual to multi-decadal natural variability in the Pacific area such as changes in properties of ENSO and PDO?
- Is the climate going to be locked in a climate equilibrium?
- What are oceanic and atmospheric dynamical processes involved in the teleconnection?

In addition, this thesis examines teleconnections in the latitudinal direction, notably tropical-extratropical and discusses the time scales of climate state during perturbation and resumption of MOC, in particular, the associated climate impacts on sea surface temperature, wind field and atmosphere-ocean circulation and feedbacks will be analyzed.

The thesis is organized as follows: Chapter 1 is intended to give a brief overview on the existing background of knowledge of the AMOC and its important to abrupt climate change, a brief understanding on Pacific climate variability including ENSO and PDO phenomenons, Pacific Ocean circulation, and a short discussion on freshwater hosing experiment over the North Atlantic and its impact to Pacific Ocean and climate variability. Chapter 2 addresses the model description, experimental design and data analysis used in this study. A set of comparison between observation and model simulation is performed in Chapter 3 to assess the model performance. Thus, in Chapter 4 the analysis results of the Pacific's climate system response to 2 Sv freshwater discharge in the North Atlantic were presented. Chapter 5 will draw some discussions and conclusions forwarding the possible mechanisms involved due to the results in Chapter 4. Finally, Appendix gives a short review of theoretical background of analysis techniques used in this study.

Chapter 2

Data and Methods

This study used a set of simulations performed by a state-of-the-art coupled climate model CCSM3. In this chapter, a brief overview on CCSM3 and its component are presented. The experimental setting of the freshwater flux simulation is discussed. Further on, the statistical analysis tools, which are used to describe climate variability of the Pacific Ocean, are introduced briefly.

2.1 CCSM3 Model Description

The Community Climate System Model version 3.0.1, known as CCSM3, was used in all simulations in this study. This model was developed by the National Center for Atmospheric Research (NCAR) released in June 2004 and was used at high-resolution in the IPCC 4th Assessment Report (AR4) in 2007. The CCSM3 is classified as an Atmospheric Ocean General Circulation Model (AOGCM), which constitutes today's most complex tool in climate modeling. The CCSM model is comprised of a system of four geophysical components, (atmosphere, land, ocean, and sea ice). A flux coupler (the CCSM Coupler Version 6.0) connects all components without flux corrections. The coupler is also responsible for remapping the boundary-exchange data in space and time. An overview of the CCSM3 is provided by *Collins et al.* [2006]. The ocean component has two possible resolutions; nominal 1° horizontal with 40 vertical levels (high resolution) and nominal 3° horizontal with 25 levels (low resolution), which has roughly 17 times fewer grid points. This study uses the low-resolution version of CCSM3. The low-resolution fully coupled configuration is the most economical configuration where an ocean at nominal 3° horizontal is coupled to an atmosphere model at T31 resolution. There are climate biases associated with the relatively coarse grids, yet the coupled solution remains comparable to higher-resolution CCSM3 results (see e.g., *Yeager et al.*, 2006).

2.1.1 CCSM3 Model Components

The atmospheric component is the Community Atmosphere Model version 3.1 (CAM3), which is based on the primitive equations with a spectral resolution of T31. This means that triangular truncation is set to the zonal wavenumber 31, which corresponds to a resolution 3.75° $\times$ 3.75° (96 longitudes - 48 latitudes) and 26 levels hybrid coordinate system. The 26 hybrid

sigma-pressure levels are divided into three parts. The upper most levels are represented as pure pressure (2.917 hPa to 83.1425 hPa). The levels in between are hybrid sigma levels, whereas the bottom levels are simulated as sigma pressure levels (*Collins et al.*, 2006).

The ocean component of CCSM3 is represented by the so called Parallel Ocean Program version 1.4.3 (POP) which is a descendant of the Bryan-Cox-Semtner models. The POP employs primitive equations, using the hydrostatic and the Boussinesq approximations to describe the ocean dynamics (*Smith and Gent*, 2004). The finite difference scheme is applied to discretize onto a dipole grid with a latitudinal resolution of 3°, while the longitudinal resolution varies in space (1.8° average and maximum refinement 0.9° in the tropics) to better resolve certain areas. In contrast to the previous version, CCSM2 and CCSM3 have an orthogonal grid with two arbitrarily located poles. The numerical poles of non-regular grid are placed over Antarctica at the true South Pole and over Greenland at 77.36°N/39.18°E. This displacement of the North Pole onto an adjacent land mass (such as Greenland), therefore, can resolve the Arctic Ocean in a singularity-free grid. The vertical resolution covers 25 unevenly spaced levels, adding up to a 4750 m depth at the maximum (the uppermost 8 levels within the first 100 m and 16 levels for the top 1000 m).

The Community Land Model (CLM3) serves as the land surface model and shares the same horizontal resolution on a Gaussian grid as in the CAM3. For each grid box is further divided into a hierarchy of land units (involving the glaciers, lakes, wetlands, urban areas, and vegetated region), soil columns, and up to 16 different vegetation types. It consists of ten sub-surface soil layers, in which temperature and moisture are calculated. The CLM interacts with the River Transport Model (RTM), a two-dimensional model with an independent grid, which simulates the horizontal transport of water in the CLM3. The documentation of the CLM3 component can be found in *Bonan et al.* [2002], *Collins et al.* [2006], and *Bonan and Levis* [2006].

The fourth component of CCSM3 is the sea ice component where The Community Sea Ice Model version 5.0 (CSIM5) has been applied. The CSIM5 consists of the elastic-viscous-plastic ice rheology and is divided into five categories of sea ice thickness. The model is discretized with the same horizontal resolution and the grid size as the POP grid size points and employs a thickness-space evolution the horizontal transport of ice. The computation of thermodynamics and dynamics of multi-category ice thickness distribution are split and carried out separately to enhance the performance. An additional feature in the CSIM5-CCSM3 is that the sea ice albedo has been altered since in the previous version (CCSM2) sea ice was too thick in the central Arctic and too extensive in the northern Hemisphere (*Collins et al.*, 2006). The cold and warm snow albedo has been decreased from 0.49 and 0.42 to 0.77 and 0.65, respectively (*Yeager et al.*, 2006).

More detail and comprehensive descriptions of the model and its components can be accessed at the NCAR CCSM web page (*http://www.ccsm.ucar.edu/models*).

2.1.2 Model improvements in CCSM3

CCSM3 has some additional improvements in comparison to its ancestor such that the representation of precipitation, clouds and aerosol, which has been improved in the atmosphere component (*Boville et al.*, 2006). Further progress has been made in the parameterization of radiation (*Collins et al.*, 2006) and the simulation of new "ice-phase" processes. Improvement in simulating aerosols eventually supports a more realistic representation of volcanic eruptions (cf. *Moelg et al.*, 2006). Improvement in the sea ice component with the new x3ocn grid gives a more accurate representation of surface stress on ice, which is important to represent advection processes of sea ice in the GIN Seas and Labrador Sea (*Yeager et al.*, 2006). In addition to numerical improvements of the ocean mixed layer which improved simulation of marginal sea ice, updates for the salt and freshwater exchange between the ocean and sea ice has been implemented. This, furthermore, is responsible for the closing of the salinity budget in the sea-ice-ocean system.

In order to have more realistic Pacific climate variability, another improvement of the CCSM3 had been made by integrating a diurnal cycle, which penetrated the uppermost layer of the ocean that eventually damped an existing cold anomaly, which extended too far to the west in the Pacific in CCSM2. This anomaly in prior was responsible to too large variability in the sea surface temperature (*Kiehl and Gent*, 2004). The low resolution model of CCSM3 was first improved in a similar manner to the models with higher resolutions (T42, T85), but it has been found that the integration of the diurnal cycle of solar heating led to several side effects. The simulation of ENSO variability became rather weak in the eastern Pacific and in the western, upper ocean discrepancies have been detected (*Danabasoglu et al.*, 2006; *Yeager et al.*, 2006). In its eventual, amelioration described anomalies in the low resolution of CCSM3 has been conducted by removing the diurnal cycle. But, the drawback is still the cold anomaly in the Pacific Ocean. Further discussion explaining biases of CCSM3 can be found in *Yeager et al.* [2006].

2.2 Experimental Design

Since the aim of this study is to investigate how the Pacific Ocean responds to the perturbation of the AMOC, it is important to consider which resolution of the model is used. A study by *Oka and Hasumi* [2006] revealed that the higher resolved experiments showed stronger currents through the Iceland and Scotland passages, and the stronger West Spitsbergen Current contributed to a better representation of the salinity distribution in the GIN Seas. They reported that resolution higher than 1.25° seems to be required in their model to simulate a realistic overturning without flux adjustment. The authors found significant dependencies of the inflow and outflow currents on the topography in the Greenland-Iceland-Norway narrow sills, which means that small changes in topography had consequences for the AMOC. For this case, the strength of the AMOC can be tuned by manipulating the narrow sill (*Oka and Hasumi*, 2006).

The control simulation of CCSM3 was integrated over 800 model years at perpetual AD 1990 present-day conditions. The ocean was initialized with the observational data taken from

Levitus et al. [1998]. Corrections were made at model year 133 due to a freshwater imbalance in the Baltic Sea. Additional 100 model years have been performed in the study of *Renold* [2007] to serve as a starting point for freshwater experiments (*Renold*, 2007; *Timmermann et al.*, 2007; *Stocker et al.*, 2007; *Renold et al.*, 2010).

The CCSM3 was forced by a freshwater discharge pulse into the North Atlantic to explore the response of the AMOC to different perturbation strengths. In order to be consistent with the Coupled Model Intercomparison Project (CMIP) of the WCRP Working Group on Coupled Models, the Atlantic Ocean region between 50°N-70°N was chosen as the experimental area (*Stouffer et al.*, 2006). However, the selected area is a rough idealization and contains some limitations in dealing with a large amount of water entering in small areas caused constrictions in simulating ocean inflows. Nevertheless, this does not seem to be unrealistic, with reference paleoclimate evidence of D/O events where the marine sediment layer show that iceberg and Laurentian ice shield had been distributed over a large area in the North Atlantic. This also in respect to the melting of the Norwegian and Greenland ice shield has contributed to the freshwater during Heinrich's events in the entire North Atlantic (*Hemming*, 2004).

The freshwater flux simulations in CCSM3 consist of five experiments (*Renold et al.*, 2010): the control simulation (CTRL), perturbed ocean with salt compensation (FC05, FC10, and FC20) for 0.5 Sv, 1 Sv, and 2 Sv respectively, and without salt compensation (FN20) by 2 Sv (1 Sv = 10^6 $m^3 s^{-1}$). The control experiment (CTRL) is performed for perpetual 1990 A.D. conditions where in all experiments, external forcing parameters (greenhouse gas concentrations, total solar irradiance, and orbital parameters) are kept at 1990 A.D. levels (*Renold et al.*, 2010). After the spin-up experiment, the subsequent 180 years are used in the analysis. This control experiment serves as a reference for all sensitivity experiments. The simulated climate of CTRL is discussed in detail in *Yeager et al.* [2006]. In the meantime, spanning 200 model years, freshwater discharge linearly increased to the maximum and after half of the period decreased back to 0 Sv. The perturbation was switched off after model year 200 allowing the model to respond to the forcing during the subsequent period (*Renold et al.*, 2010). The freshwater flux of 1 Sv is due to estimates of short meltwater release during deglaciation (*Clarke et al.*, 2003) and is equivalent with about 9 m sea level rise, while the largest value of about 2 Sv is equivalent to a sea level rise of about 18 m and is the range of estimates for the last ice age (*Stocker et al.*, 2007).

In order to have an outlook of Pacific Basin response in terms of climate variability response to freshwater discharge in the North Atlantic, the presented freshwater flux simulation in this thesis uses the experimental design that had been conducted in *Renold* [2007]. In those simulations, salt was uniformly taken out of the uppermost layers in the forcing area and evenly distributed to the rest of the ocean (*Renold*, 2007; *Stocker et al.*, 2007; *Timmermann et al.*, 2007; *Renold et al.*, 2010). The chosen method was applied to assure that the global salt content remains constant. To carry out water hosing experiments, at least two possibilities exist to simulate the freshwater input: applying freshwater directly into the uppermost layer of the Northern Atlantic or to release an equivalent of freshwater to the surface as a virtual salt flux (*Stouffer et al.*, 2006). Both methods have been used routinely in the past and for weak forcing, and no significant discrepancies have been reported in the literature. More

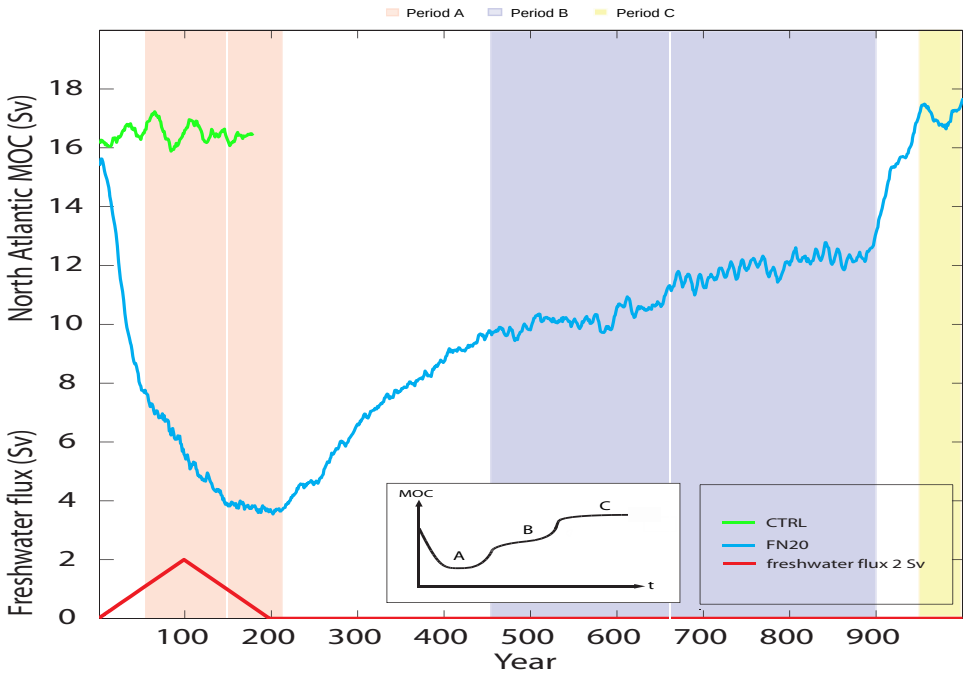

Figure 2.1: Response of the North Atlantic maximum meridional overturning circulation to 2 Sv freshwater forcing (FN20) into the North Atlantic. Time series are smoothed with a 10-yr running mean. The inset schematically separates the resumption process of the experiments into three consecutive phases (A to C). The freshwater forcing, which is applied to the North Atlantic (50°N to 70°N) over 200 years, is denoted at the bottom-left corner. (modified after *Renold et al.*, 2010)

details information due to the used parameterization and the adjustments, the forcing files, the modified code, and the mask files documentation, it can be found in the supplementary material of *Renold* [2007].

This study will focus only on experiment FN20 where there is no applied salt compensation in the simulation. The FN20 simulation does not satisfy the global salinity budget. The response of the AMOC to the artificial freshwater forcing is shown in Figure 2.1 with three periods of the AMOC state. The minimum state is reached within 150 to 200 years after a rapid decline caused by the freshwater forcing, and after, the AMOC resumptions to recover back to as the normal state and lasts for about 50 years (*Renold et al.*, 2010). The minimum state is denoted as Period A where AMOC reached a minimum below 4 Sv by the end of perturbation, followed by period B, which is characterized by a quasi-stable plateau at about 10 Sv during years 450-900. Period C is depicted by the last 50 years when the AMOC has rapidly switched to a state at about 1 Sv stronger than the initial strength in the CTRL simulation. We revisit the unresolved issues of the linkage between the AMOC slow downs and cooling in the North Pacific and look at the three-period time scale of AMOC under non compensated-freshwater hosing experiment (FN20) in the CCSM3 model.

2.3 Methods

2.3.1 Regridded model output

As mentioned in advance the ocean and sea ice component of the CCSM3 operates on a non-regular grid. Thus the output has to be regridded (or remapped) onto a regular grid. This regridding process was performed by employing the NCAR Command Language (NCL) built-in function "PopLatLon" and the corresponding mapping weight file *map_gx3v5_to_1x1d_bilin_da_040122.nc*. The first step in the grid transformation "regridding" is to define a relationship between the input and output grids within a common frame of reference or coordinate system. Regridding bases the inter-grid relationship on "world" coordinates, and the NCL map between CCSM3 grid coordinates (i,j) and world coordinates (lon, lat). Regridding process uses two basic methods for doing the transform that are box averaging or interpolation. The analysis in this thesis uses the box averaging method. Box averaging is simply the area-weighted integral of all input grid boxes which intersect an output grid box, divided by the area of the output grid box. Area-weighted integrals and the interpolating procedures of the data from one grid onto the other inherit a small error which is not addressed any further in this study. For further detailed description of the bilinear regridding procedure, the reader is suggested to refer *Jones et al.* [2001].

2.3.2 Analysis Technique

The climatological monthly SST data from the Simple Ocean Data Assimilation (SODA) reanalysis on 0.5° grid (see *Carton et al.*, 2000 for description) and geopotential field from the European Centre for Medium-Range Weather Forecasts (ECMWF) ERA40 reanalysis (2.5° grid resolution) have been used to compare with the model output of CTRL simulation in CCSM3. The aim is to examine the degree of conformity between model performance and the observation to simulate climate variability in the Pacific region. To simulate the Pacific's climate variability, the 198 years of CTRL simulation and 1000-year of FN20 simulation model runs are calculated into monthly and yearly weighted averaged to perform several proposed simulation using ocean and atmosphere variable such as Potential Temperature (TEMP), Zonal and Meridional Wind Stress (TAUX, TAUY), Sea Level Pressure (PSL), Geopotential Height (Z3), Convective and Large-scale Precipitation (PRECC and PRECL), etc. Some analysis methods, which are used in this study include compositing, linear regression and correlation analysis, wavelet and spectral Fourier transform and Empirical Orthogonal Function (EOF) analysis. The description of these statistical methods is briefly presented in the Appendix. Monthly anomalies are defined by subtracting the long-term monthly means from the individual monthly values for a given year. Annual anomalies are defined by subtracting the long-term means from the individual year values for a given year. It should be noted that in order to have the same references, the long-term means values are taken from the CTRL simulation for comparison purposes in some analysis as will be mentioned in the analysis and data interpretation.

All analyses on the data set described above have been performed by employing some sophisticated software such as Climate Data Operators (CDO), NetCDF Operators (NCO), and NCAR Command Language (NCL). CDO is a collection of UNIX-based command line opera-

tors to process and analyze a climate data series. It has been developed by the Max Planck Institute for Meteorology (*http://www.mpimet.mpg.de/fileadmin/software/cdo/*). NCO is command line executables specifically designed for multi-file bulk processing on NetCDF data (*http://nco.sourceforge.net*). And NCL is an interpreted computer language developed by NCAR and is highly suited for meteorological and climatological data processing and visualization. NCL handles netCDF, GRIB, and HDF data formats with ease and is officially supported by an online library (*www.cgd.ucar.edu/csm/support/*).

Climate Indices and Teleconnection

It is well known that ocean, atmosphere and land processes are highly coupled. This is understandable since climate phenomena occurring in one location can affect the climate at a far away location. Understanding these climate teleconnections is critical for finding the answers to questions such as how the Earth's climate is changing and how ecosystems respond to global environmental change. A common way to study such teleconnections is by using climate indices, which distill climate variability at a regional or global scale into a single time series.

Scientists use climate indices in their attempt to characterize and understand the various climate mechanisms that culminate in our daily weather and are used to represent the essential elements of climate. Climate indices are generally identified or devised with the twin objectives of simplicity and completeness, and each typically represents the status and timing of the climate factor they represent. By their very nature, indices are simple, and combine many details into a generalized, overall description of the atmosphere or ocean which can be used to characterize the factors which impact the climate system. Because the climate indices are generally determined from measurements made in a localized area, they can have impacts in other areas around the globe, through teleconnections. Climate indices, in the form of time series, are able to summarize the behavior of selected regions of the Earth's oceans and atmosphere. In the past, Earth scientists have used observation directly,but more recently, eigenvalue analysis techniques, such as principal components analysis (PCA) and singular value decomposition (SVD) are used to discover climate indices and teleconnections. However, eigenvalue techniques are only useful for finding a few of the strongest signals. Furthermore, they impose a condition that all discovered signals must be orthogonal to each other, making it difficult to attach a physical interpretation to them. Finally, these analysis tools do not contain any physical information or assumptions regarding climate processes.

ENSO Indices

The phenomenon of ENSO and inter-annual climate variability associated with it have been extensively studied since Rasmusson and Carpenter (1982) gave a comprehensive description of a composite El Niño using surface wind and SST data from 1949 to 1976. Most of ENSO studies, however, focused on the eastern Pacific anomaly patterns since its inter-annual anomalies in the eastern and central Pacific are large and well observed. To represent the inter-annual and decadal variability in the tropical Pacific, we defined an area-weighted average of the SST anomalies over the eastern-central tropicalPacific (5°S-5°S, 170°E-120°W).

Anomalies are obtained by subtracting the monthly SST with the long-term climatology monthly mean. The resulted series are normalized by their temporal standard deviation. The area is referred to as the Niño3.4 region which is one of the several Nino region indicators commonly used for representing tropical Pacific SST variability associated with the ENSO (*Trenberth*, 1997) and its long-term variations. The Niño3.4 region has large variability on El Niño time scale, and is close to the region where changes in local sea surface temperature are important for shifting the large region of rainfall typically located in the far western Pacific. An El Niño or La Niña event is identified if the five-months running average of the Niño3.4 index exceeds +0.4°C for El Niño or -0.4°C for La Niña for at least 6 consecutive months, according to the definition proposed by *Trenberth* [1997].

PDO Indices

The PDO is often quantified using the PDO Index, which is defined by spatially averaging the monthly sea surface temperature (SST) of the Pacific Ocean north of 20°N. The global average anomaly is then subtracted to account for global warming (*Hare and Mantua*, 2000). Normally only October to March values are used in calculating the PDO index because year-to-year fluctuations are most apparent during the winter months (*Mantua and Hare.*, 2002). When the PDO Index is positive, waters in the north central Pacific Ocean tend to be cool, and waters along the west coast of North America tend to be warm. The opposite is true when the PDO Index is negative. The effects of the PDO strongest in the Pacific Northwest. In this region, a positive, or warm-phase PDO, generally correlates with lower than average rainfall and higher than average air temperatures. Likewise, a negative, or cool phase PDO, correlates with relatively high precipitation rates and low air temperatures (*Mantua and Hare.*, 2002).

In this study, the method for computing the PDO index has been adopted from *Zhang et al.* [1997]. The analysis used the sea surface temperature (SST) time series from monthly and yearly model output of control runs 933-1133 and FN20 run 0-1000. The general steps are as following: monthly SST data fields, both for CTRL run and FN20 simulation, for all grid points were, firstly, annual weighted average to avoid the effect of seasonality, and an area weighted average regards to irregular boxes latitudinally. Annual weighted average is an averaging process which calculates monthly values to annual values weighted by the number of days in a month. SST anomaly was created by subtracting annual SST with yearly mean global SST time series. The resulted series are normalized by their temporal standard deviation. The second step is creating a "residual SST anomaly" field for the North Pacific by subtracting the global mean anomaly from each North Pacific grid point (20°N-70°N, 140°E-120°W). The third step is computing the EOFs of the North Pacific residual SST anomaly fields. And eventually, the PDO index is therefore, the leading PC of the above analysis. To have an overview of PDO changes during the freshwater hosing experiment, the PDO index values are achieved by projecting North Pacific residual SST anomalies of FN20 onto the leading eigenvector (the "PDO pattern" of SSTs).

Teleconnection

Teleconnection pattern is defined as a regional or planetary scale pattern of correlated and anti-correlated anomalies. It may be induced either by internal atmospheric dynamics or by coupling with other components of the climate system (mainly the tropical oceans). It means that although a linear interpretation of teleconnection is adequate in most cases, nonlinear effects should not be neglected. So far, inter-annual climate variability can be explained through teleconnections. Teleconnections related to ENSO are well modelled in the tropical and extra-tropical region. Prediction of tropical rainfall teleconnections, however, require accurate modelling of heat-flux feedbacks from the ocean mixed layer and land surface. Nowadays, there are several teleconnection patterns that have been discovered through studies using both observational data and modeling approaches i.e., ENSO global teleconnections, the North Atlantic Oscillation (NAO), the Indian Ocean Zonal Mode (or Indian Ocean Dipole, IOD), the Pacific/North American (PNA) pattern, and Eastern Atlantic (EA) pattern, Arctic Oscillation (AO), etc (*Stoner et al.*, 2009).

Chapter 3

Pacific Climate Variability in the CCSM3

In this chapter, the performance of CCSM3 to represent climate variability in the Pacific basin is examined. Therefore, the CTRL1990 simulation is compared with observational data. Observational data consists of Simple Ocean Data Analysis (SODA reanalysis) for representing SST over the period of 1957-2004, and reanalysis data from ERA40 for the period 1960-2001 for the 500-hPa geopotential field. The EOF/rotated EOF analysis is applied to SST and 500-hPa geopotential height over the Pacific, particularly in the tropical Pacific and the North Pacific. The power spectral and wavelet analysis are presented to compare the dominated time scale.

3.1 Pacific Sea Surface Temperature

The mean SST patterns over Pacific for observation and the CTRL simulation are shown in Figure 3.1. In general, the seasonal cycle of the SST distribution is simulated reasonably well, except in the tropical region. Compared with observation, the simulation gives a common feature of interhemispheric SST distribution in the Pacific northern and southern hemisphere for all seasons, except the tropical region, in particular the eastern Pacific cold tongue is less pronounced in the model and is displayed to the central Pacific during spring. Moreover, despite a less pronounced eastern Pacific cold tongue in the model, spring mean SST pattern over the tropical region shows a positive difference which is centered in the central Pacific. The extension of the warm pool region over the western Pacific is too narrow and centered along the equator during spring (MAM). The structure of warm SST in the eastern Pacific off the equator (west coast of central America) are also failed to be simulated in the model during fall (SON) and winter (DJF). The difference maps of SST distributions from SODA relative to CTRL simulation show that, in general, for all seasons, the North Pacific simulated SST is colder than observed. It is also prevailed in the tropical region during spring to summer. The structure of the eastern Pacific cold tongue is relatively warmer in the simulated SST compared with observation.

Pacific SST Mode in CCSM3

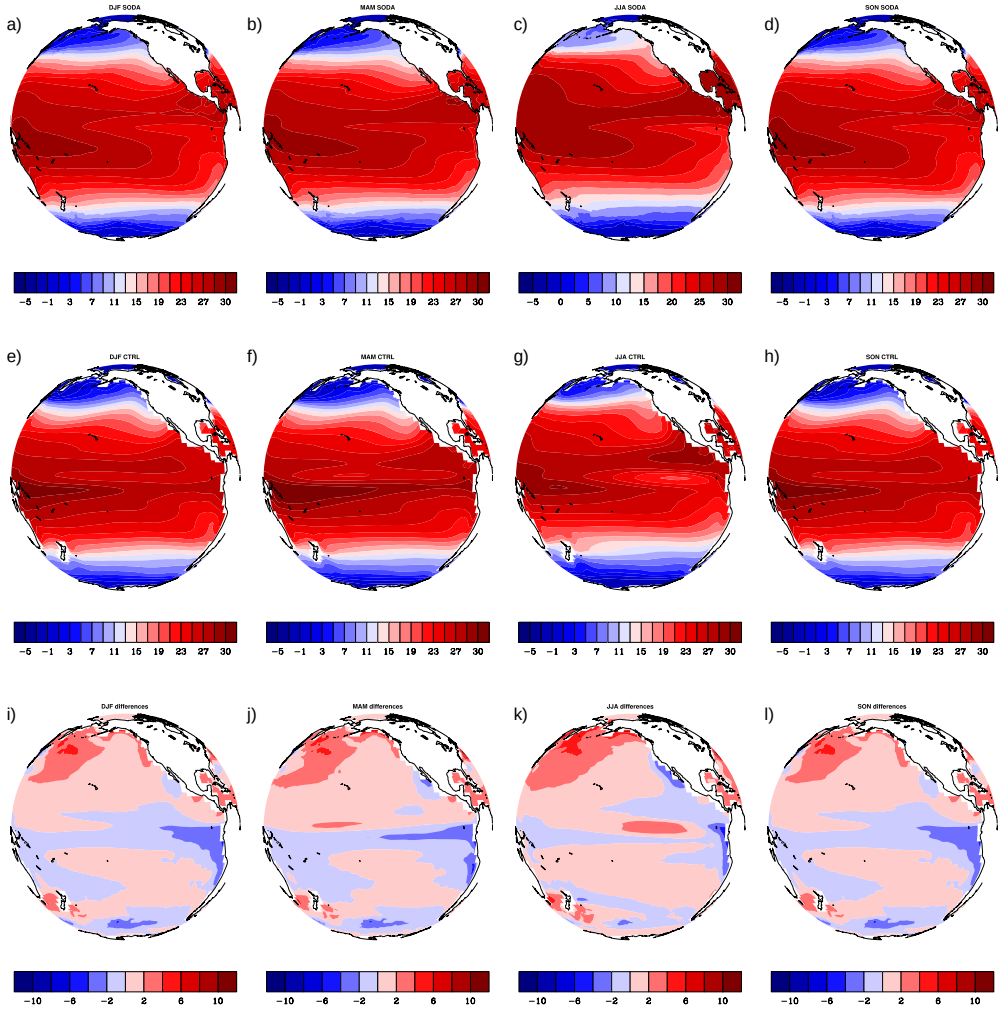

Figure 3.1: Seasonal mean SST pattern for the observation (top panel) and the CTRL simulation (middle panel). The long-term seasonal mean is based on monthly mean recorded data from SODA reanalysis 1957 - 2004 (see *Carton et al.*, 2000 for description) and CTRL 1990 simulation of 198 model years. The winter (DJF) is displayed in (a, e, i), spring (MAM : b, f, j), summer (JJA : c, f, k), and fall (SON : d, h, l). The seasonal differences SST are obtained by subtracting the SST of CTRL simulation from observed SODA (bottom panel).

To evaluate the CTRL simulation with respect to the SST variability, we focus on the dominant modes of the Pacific. Therefore, an EOF analysis is applied to the entire Pacific region i.e. 20°S-80°N, 140°E-120°W. The three leading EOF modes for observation and CTRL simulation and their associated time series are shown for summer and winter in Figure 3.2 and Figure 3.3, respectively.

In the observation data, the first EOF which explains about 29% of the total variance is characterized by an ENSO-like pattern (Figure 3.2; left panel). The pattern is similar to the "ENSO-like decadal mode" from *Zhang et al.* [1997], which is clearly seen both during

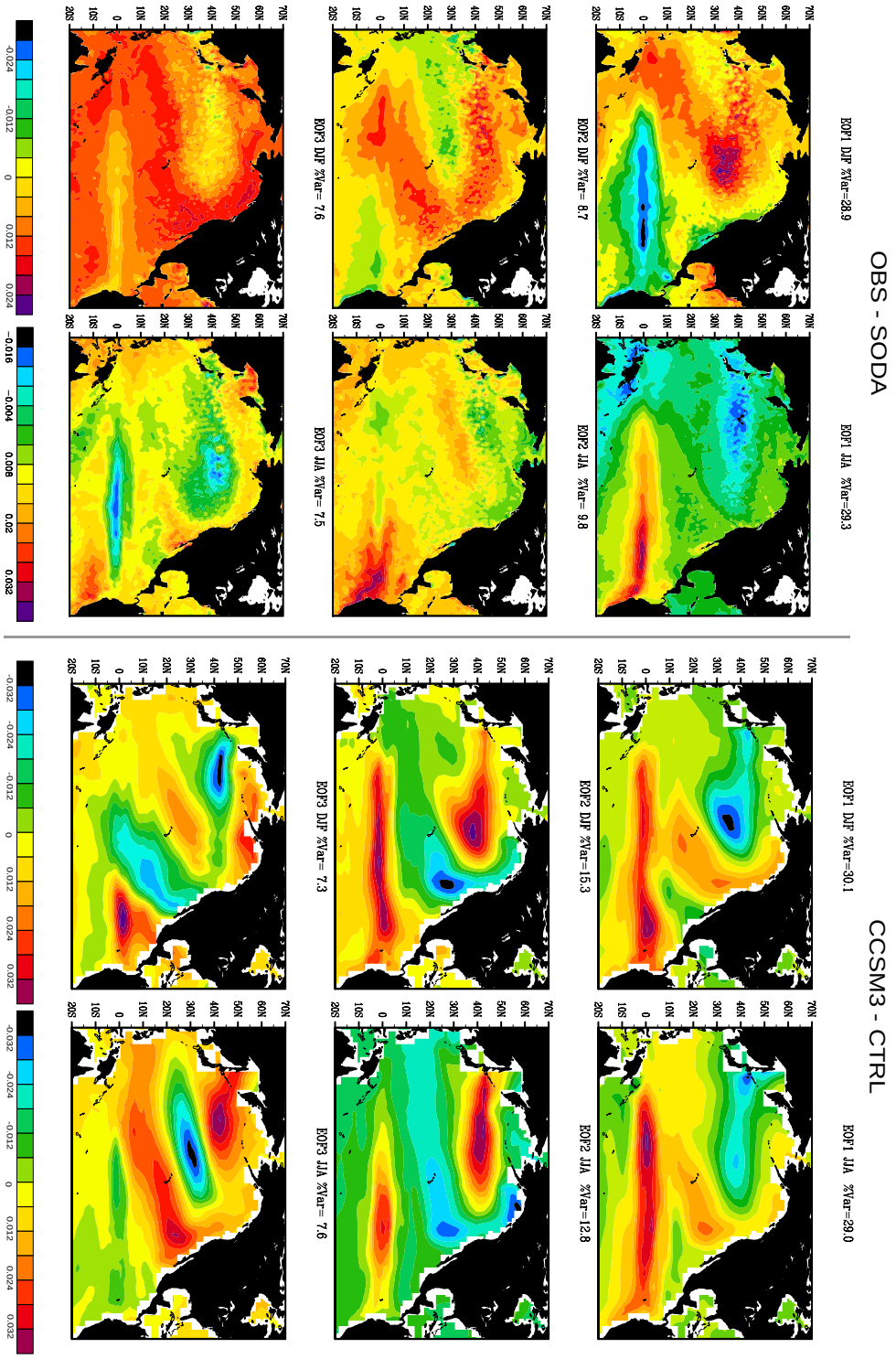

Figure 3.2: The three leading EOF patterns of winter (DJF) and summer (JJA) for observed SST and the CTRL simulation in the Pacific north of 20°S. The EOF patters are computed via a covariance matrix and presented as normalized eigenvector (see appendix 1).

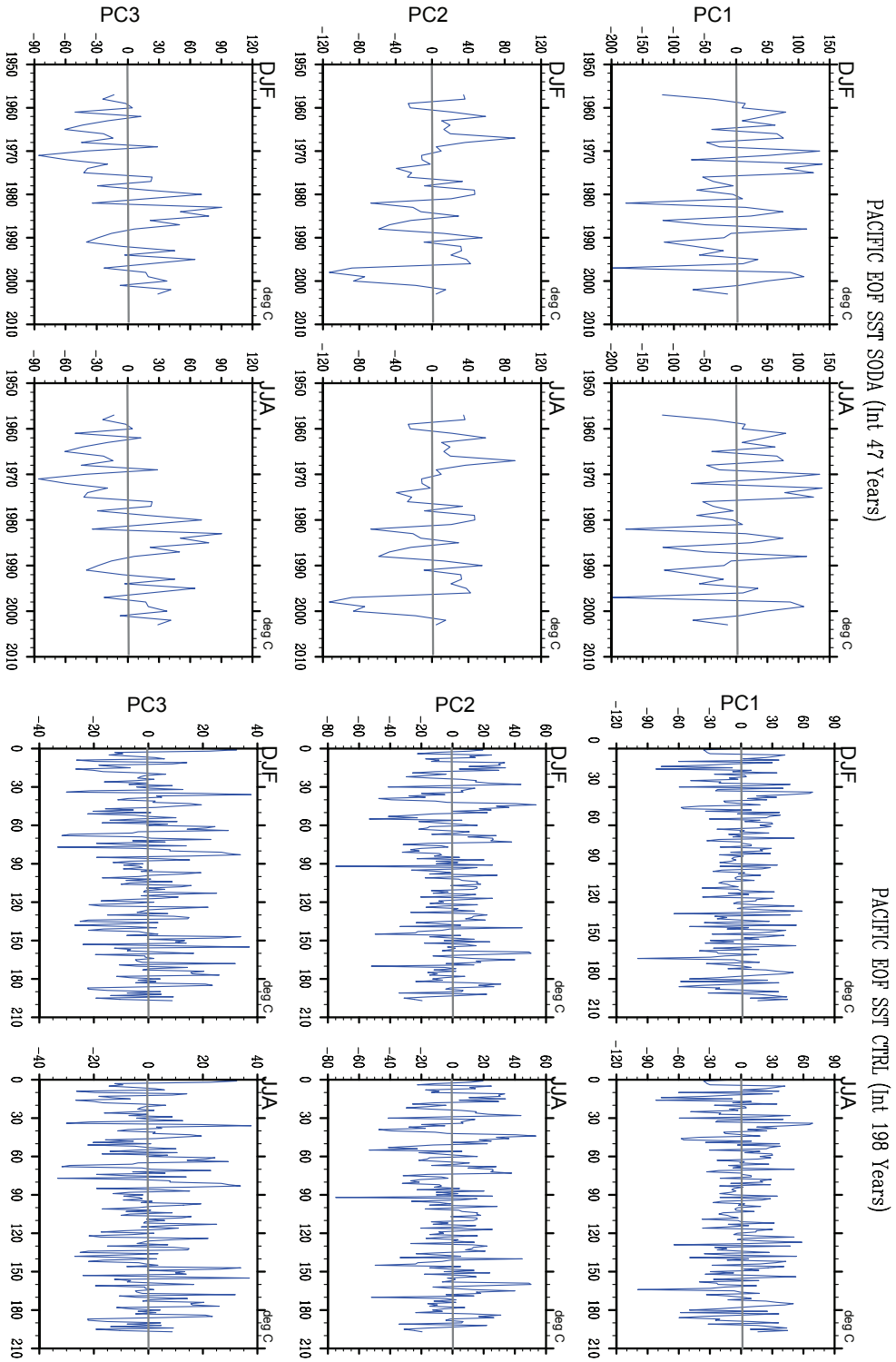

Figure 3.3: The PC time series of the first three EOFs for winter (DJF) and summer (JJA) for observations (left panels) and the CTRL simulation (right panels).

winter time (DJF) and summer (JJA). The leading mode shows a predominantly feature along the tropical region which is known as the "ENSO tongue" pattern (sometimes the so called tropical Pacific Mode, TPM) and the 2^{nd} dominant feature is in the western to central North Pacific tongue (sometimes referred to as North Pacific Mode, NPM). In winter time, the leading mode is marked by a dipole pattern between the warm (cold) SST in the tropical region and the cold (warm) SST in the central to west North Pacific extended to around north east of maritime-continent. The dipole pattern with opposite conditions is obtained as well in the summer SST variability. The 2^{nd} and the 3^{rd} EOF modes of the observed SST explain less than 10% of the total variance. The 2^{nd} mode shows a pattern along the subpolar region and the south-east North Pacific sector, which is seen as "a horse shoe-like" structure. This pattern is marked by warm (cold) SST over those areas, while cold (warm) SST is pronounced over the western North Pacific and eastern tropical Pacific. This mode is shown as a quadrilateral pattern over western North Pacific, subtropical region and eastern tropical Pacific and is significant during winter. The 3^{rd} EOF shares only about 8% explained variance with a predominantly tripole pattern as a diagonal structured across northern Pacific basin.

In the CTRL simulation, similar patterns are found but winter and summer are less distinct (Figure 3.2; right panel). The ENSO-like pattern is clearly found in the first EOF in both seasons. The 1^{st} EOF shows a structure with predominantly west-central Pacific during summer. This leading mode shares about 30% of the explained variance and the pattern is similar to the observed TPM pattern. The spatial correlation between simulated and observed pattern is 0.7. It should be noted that if the associated PC time series of that EOF is then regressed onto global SST, the obtained pattern is the NPM and has come to be known as Pacific Decadal Oscillation/PDO pattern (*Mantua et al.*, 1997) as depicted in the next part. The simulated 2^{nd} EOF leading mode explains about 15 and 13% of the total variance for winter and summer, respectively. As for the first EOF, the distinction between both seasons is less clear than in the observation. It seems that the 2^{nd} simulated mode is rather similar to the 3^{rd} leading mode in the observation with regards to the pattern of eastern tropical Pacific and western North Pacific tongue. The "horse shoe" structure is also displayed rather similar with the 2^{nd} observed mode, particularly during winter time. However, the eastern Pacific tongue operates further north and is centered in the north off-equatorial eastern Pacific in comparison to observation. The 3^{rd} EOF which only explains 7% of the total variance shows a quadrilateral pattern with a center of action near subpolar front, subtropical sector and eastern tropical Pacific.

The associated time series of EOF 1 (PC1) of the Pacific's basin SST is characterized by inter-annual to decadal variability (4-year periods in the observation and 2-4 and 20 years period in the simulation). The PC1 time series of the observed SST in both seasons show a climate shift i.e., a rather warm phase from 1957 to 1976 succeeds a cold phase from 1977 to mid-1990s. The warm and cold episodes have a period of about 20 years, which is consistent with previous studies (*Mantua et al.*, 1997; *Minobe*, 1997; *Wu et al.*, 2003; *Wu and Liu*, 2003). The PC2 time series also shows inter-annual to decadal variability (8-year periods in the observation and 2-3 and 20 years period in the simulation). The resemblance between the 2^{nd} EOF CTRL simulation with the 3^{rd} EOF observed SST is also confirmed by the power spectra analysis (not shown) which has inter-annual variability (2-3 years cycle), although bidecadal variability appeared in the model and have not seen in the observation. The PC3 time series

shows rather a shift as in PC1 and exhibits a 2-3 and 8 years period in the simulation. The dominant periods of the PC time series indicate that the NPM has inter-annual variability, which is possibly forced by the high and low frequency variability of ENSO (*Vimont*, 2005).

Tropical Pacific Mode and ENSO

In order to have a general perception of the tropical Pacific SST mode, here the EOF analysis of the tropical Indo-Pacific is also performed. The three leading patterns annual SST variability in the covered domain area of (7.5°N-7.5°S, 50°E-60°W) for observation and CTRL simulation are compared in Figure 3.4. In the observed SST, the 1^{st} EOF which accounts for 49% of the total variance explained the dominant SST variability over the domain. The equatorial "cold tongue" is strongly pronounced in the eastern equatorial Pacific. It extends from the coast of Peru to about 170°W and is clearly seen as the largest SST anomaly variance. The 2^{nd} EOF with 21% explained variance shows the largest SST anomalies in the central Pacific. The two leading SST patterns are most probably associated with the two types of ENSO those are the eastern Pacific (EP) type and central Pacific (CP) type (*Kao and Yu*, 2009). The ENSO CP type has been observed in the last two decades, in which the usual place of the temperature anomaly is not affected, but an anomaly arises in the central Pacific (*Larkin and Harrison*, 2005). The phenomenon is also called the "dateline" El Niño (because the anomaly arises near the dateline), or El Niño "Modoki" (Modoki is Japanese for "similar, but different") (*Ashok et al.*, 2007). The 3^{rd} EOF which explains 6.2% of the total variance, shows an SST structure centered along the central to the west equatorial Pacific and a dipole structure in the north-south off east equatorial Pacific as well as an anomaly of the equatorial cold tongue in the west.

The first EOF of the CTRL simulation has its major center of action over central equatorial Pacific and explains 46% of the total variance. Thus, the simulated leading mode is dominated by an ENSO CP type, which is in association to the 2^{nd} mode in the observation. The CP ENSO marked by SST anomalies over central Pacific and is related to Warm Pool area displacement (*Kao and Yu*, 2009; *Kug et al.*, 2010). The 2^{nd} and the 3^{rd} EOF which are explained by 10% and 8% of the total variance, respectively, exhibit the anomaly of the east Pacific cold tongue and dipole structure of SST variation off the central equatorial Pacific (similar to ENSO EP type). The 2^{nd} EOF of CTRL simulation is more comparable with the leading pattern in the observation, and vice versa for the 1^{st} EOF. The 2^{nd} and 3^{rd} EOF may represent the variability of Cold Tongue El Niño type that has been known as a conventional El Niño. Moreover, the equatorial Pacific tongue in the CTRL simulation is strongly pronounced in the central Pacific and seems to be centered far too west than observed. This characteristic is also confirmed by the spatial distribution of the SST standard deviation over the same domain in Figure 3.5 whereby the simulated cold tongue variability is stronger and displaced to the west compared to observed. However, this feature is the best CCSM3 model performance as has been reported in *Deser et al.* [2006]. The authors stated that the CCSM3 simulation has already an improvement regarding to the cold tongue bias compared to the previous version. Accordingly, the bias is due to the inclusion of the diurnal cycle in penetrating solar radiation in the ocean model component (see *Danabasoglu et al.*, 2006; *Deser et al.*, 2006).

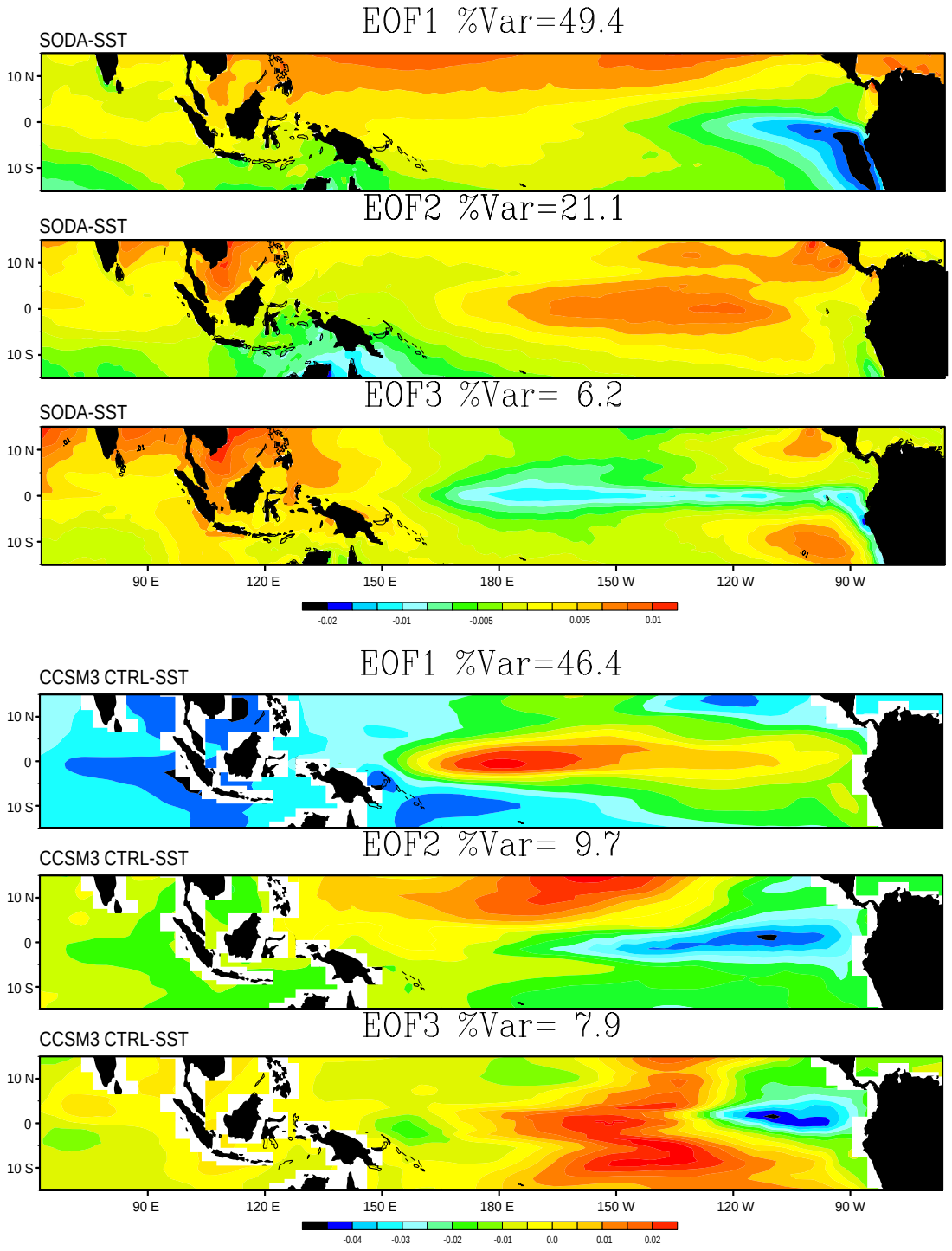

Figure 3.4: Three leading pattern of tropical SST for observations and the CTRL simulation. The EOF patterns are obtained similar to Fig 3.2 with color interval 0.01.

The Niño-3.4 SST index is a commonly used index for representing tropical Pacific SST variability associated with ENSO. The index is defined as the area average of monthly SST anomalies in the region 5°N-5°S, 170°E-120°W (*Trenberth*, 1997). This region is located within the area of maximum SST variance (*Deser et al.*, 2006) and also lies within the center of SST anomalies of the leading EOF pattern of monthly tropical Pacific SST (Figure 3.4). Figure 3.6 shows time series of the Niño-3.4 SST index for the observation and the CTRL simulation. An arbitrary segment of 40 years from CTRL simulation is shown together with the period of record available for SODA data (1960-2000; 40 years). A comparison reveals that the simulated variability is too regular and shows a period of 2.5 years, whereas the dominant observed periods are in the range of 3-8 years. The amplitude of the Niño-3.4 SST variability in CCSM3 is overestimated ($\sigma = 0.74$°C for model with regard to the model years 0-100) in comparison to observation ($\sigma = 0.47$°C for recorded year 1957-2004). Still, this model performs a more realistic ENSO than in its previous version (see e.g.,*Deser et al.*, 2006; *Kiehl et al.*, 1998).

In order to quantify the frequency and the amplitude of ENSO variability, the power spectrum analysis is applied to the entire time series for both observation and CTRL simulation (Figure 3.7). Consistent with the visual impression of the time series, the dominant frequency in the simulated CTRL power spectra (1.6 - 2.5 years cycle) is relatively too high in comparison to the observation (2.5 - 8 years cycle). This inter-annual periodicity is also depicted by global wavelet spectrum where the Niño-3.4 SST index has a frequency peak at about 2.3 years and at 20 years, while the observed peaks are at about 3.2 years and 14 years.

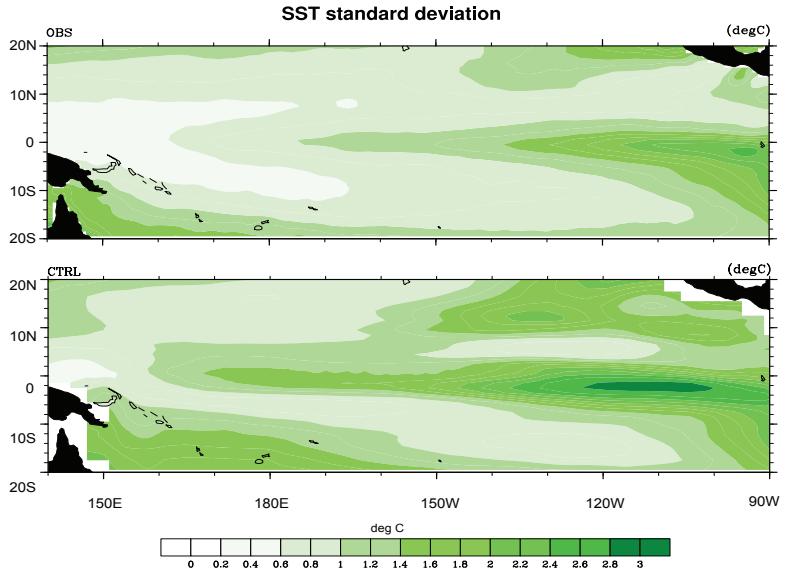

Figure 3.5: Standard deviation of the tropical Pacific SST for observations (top) and the CTRL simulation (bottom). Standard deviations are computed based on the monthly data and describes the population standard deviation as the square root of the average value of $(x - \mu)^2$. Color scales is given at the bottom of the map.

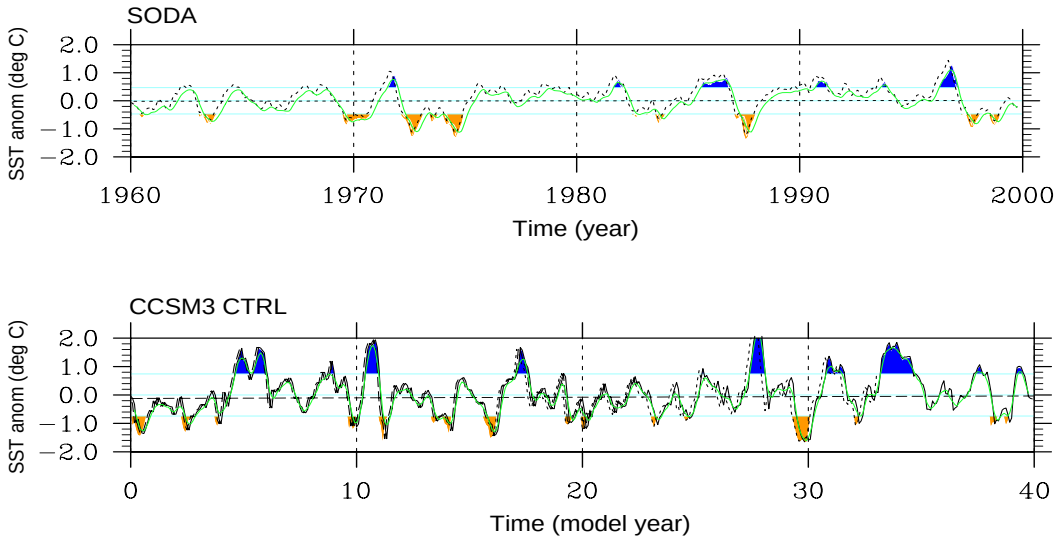

Figure 3.6: Time series of monthly SST anomalies (°C) of the Niño-3.4 index for observation (top) and CTRL simulation (bottom). A 40-year segment is shown for each time series (1960-2000 for SODA and 40-80 model year for CTRL simulation). The standard deviations are given as light blue lines and 5-month running means are denoted by green lines. The blue (orange) shading classifies the warm (cold) ENSO years.

The seasonal cycle of the monthly averaged within Niño-3.4 region SST and its standard deviation are shown in Figure 3.8. The observed Niño-3.4 index peaks in the late fall (May) and shows lower SSTs during winter time (DJF). The simulated seasonal cycle is quite similar to the observation, except during the DJF season where the SST has a second peak. In general, the model shows a warming from fall to winter and a spring time cooling followed by warming in the early summer and then cools during summer to fall. Thus, two peaks (January and April) exist in the model, while only one peak is detected in the annual cycle of observation. It can also be seen that generally the model overestimates the SST during winter (DJF) and underestimates it over the rest months of the year. The observed seasonal cycle of the standard deviation exhibits minimum variability during April-June and maximum in the early boreal winter (ONDJF). This seasonal variation is marked by "V" cycle. The simulated seasonality of the standard deviation also deviates from the observation. The model tends to underestimate the standard deviation by approximately a factor of 2 during winter (DJF) and overestimates the standard deviation strongly in April and May.

The corresponding SST pattern to the Niño-3.4 SST index is obtained by correlating and regressing from the Niño-3.4 SST index onto the global SST field (Figure 3.9). This pattern confirms the model performance that has been discussed in the previous paragraphs where

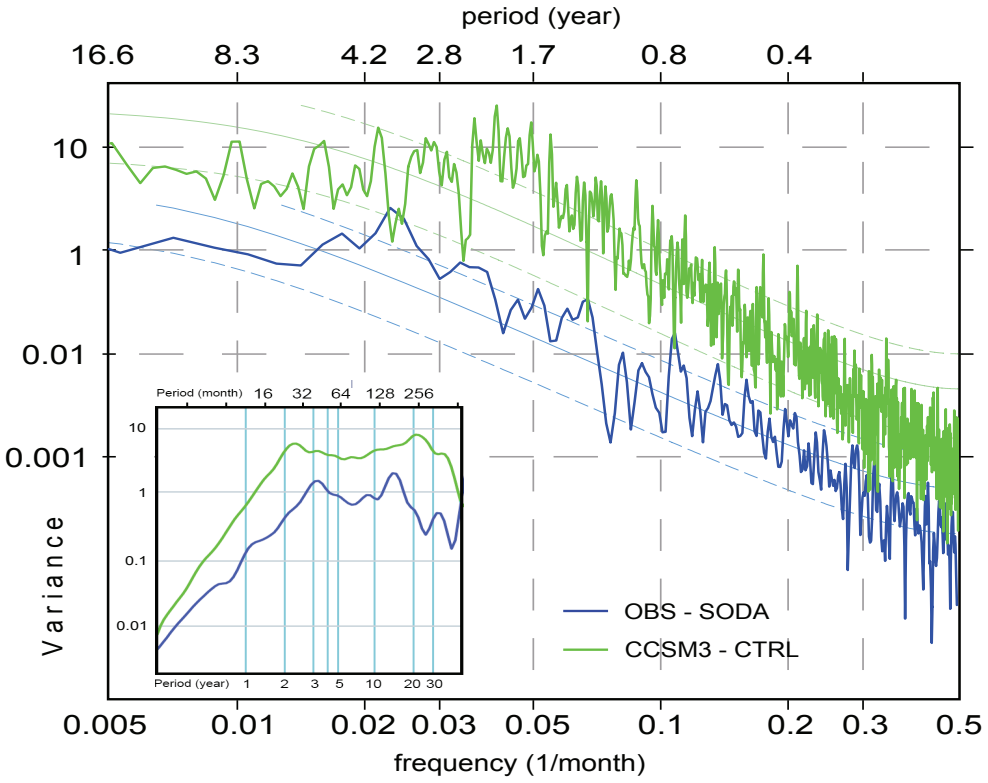

Figure 3.7: Power spectra of the monthly Niño-3.4 SST anomaly time series for full period from Observation (SODA, 47 years) and CTRL simulation (198 model years). Dashed lines indicate the 90% and 10% and the solid middle lines indicate 50% of confidence interval, respectively. (Insert : global wavelet spectrum for the same time series).

simulated tropical Pacific SST is too narrow and too far to west relative to the observation. However, the correlation map between the Niño-3.4 SST index with global SST shows a very similar coefficient (0.5-0.8) located in central to west Pacific for both simulations. From both regression maps one can get an impression that somehow the Niño-3.4 SST index has a linkage to the North Pacific SST variability i.e., that the regression map showed a positive coefficient with the SST field over the eastern Pacific west cost America as well as SST field in the sub-tropical gyre region. It is also visible that the Niño-3.4 SST index is related linearly with the negative regression coefficients of the SST field over the western Pacific i.e. subpolar region.

Warm minus cold ENSO composite difference maps of annual SST are shown in Figure 3.10. Warm (cold) years were identified based on the criterion that the Niño-3.4 SST index exceeds one standard deviation (is less than -1 standard deviation) as described in Figure 3.6. For the observation, the cold ENSO event composites are : 1971, 1974, 1976, 1985, 1989, 1999, 2000 and the years used for the warm event composites are: 1958, 1966, 1973, 1983, 1987, 1992, 1995, 1998. In the CTRL simulation warm and cold event composites are represented for the 40-year segment as in Figure 3.6. In general, the warm-minus ENSO composite in the CTRL simulation is in agreement with observed SST. Over the tropical Pacific, the observed SST

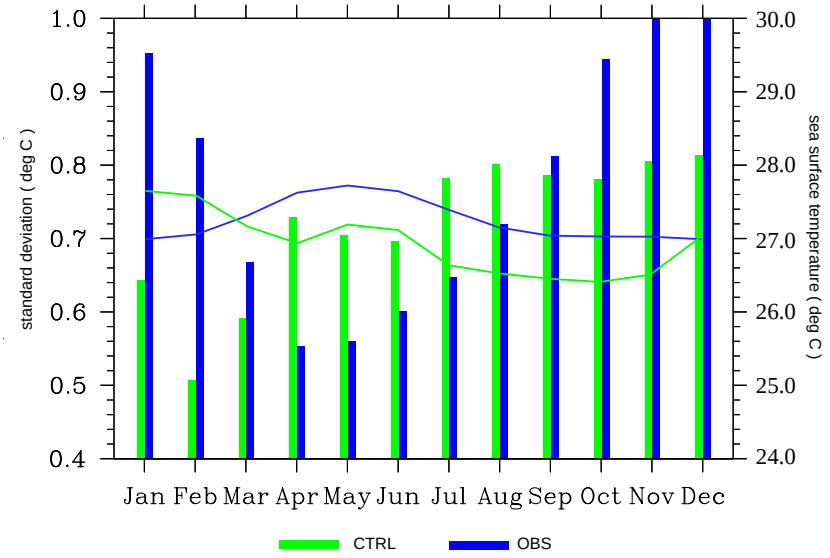

Figure 3.8: Seasonal cycle of the monthly mean (line) and standard deviation (bar) of the SST over the Niño-3.4 region for observations (SODA) and CTRL.

consists of positive anomalies, which are larger confined in the south off - central Pacific than in the CTRL simulation, whereas the equatorial eastern Pacific is featured as the negative anomalies. The negative anomaly is collocated with the location of the cold tongue usually observed. The simulated CTRL SST shows a symmetry dipole positive anomaly in the eastern off-equatorial Pacific. The negative anomaly is also shown in the west cost central America which does not appear in the observations. The negative anomaly is more centered in the central equatorial Pacific with less negative anomalies in the equator line in comparison to observation. Therefore, that the annual ENSO amplitude is relatively weaker in the simulated SST rather than in observed SST. However, it should be noted that if the monthly SST is used, the CTRL simulation shows a stronger anomaly than observed (not shown).

The yearly temperature variations of the top 300 m in the ocean are meridionally averaged over 4°N-4°S, 140°E-60°W during warm (El Niño), cold (La Niña) event and the 30-year averages and are shown in Figure 3.11a. The composite warm and cold ENSO years follow the criteria in the previous paragraph. From the zonal cross-section profile, thermocline depth can be estimated. Thermocline depth here is defined as the isotherm layer of 15°C and 20°C of subsurface ocean temperature in respect to permanent and seasonal thermocline depth, respectively. Looking at the vertical profile of subsurface temperature, particularly the isotherm of 15°C and 20°C, it is possible to distinguish the differences between the warm and cold events, where by definition warm ENSO (El Niño) is identified as the deepest ther-

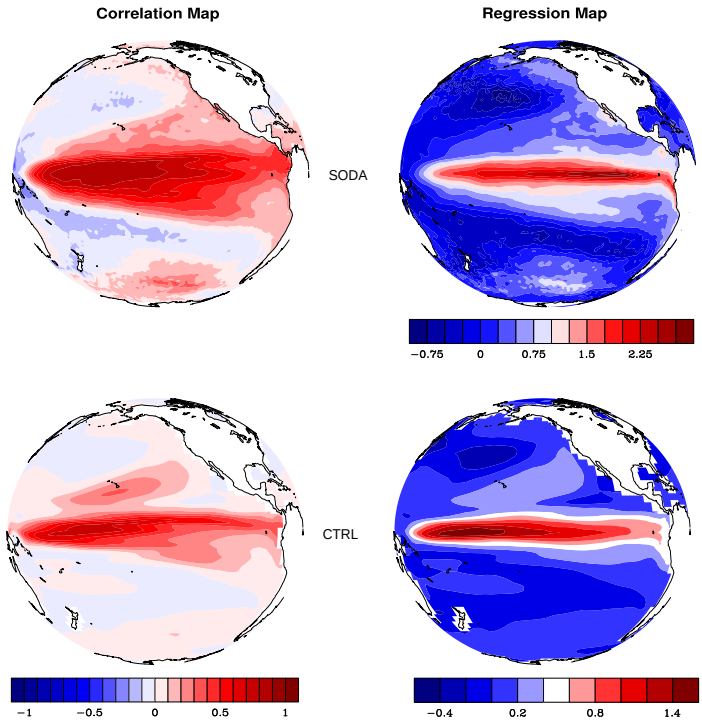

Figure 3.9: Correlation and regreesion map of the Niño-3.4 SST index with global SST for observations and the CTRL simulation. Correlation and regression coefficients are given as color scales at the bottom of the map.

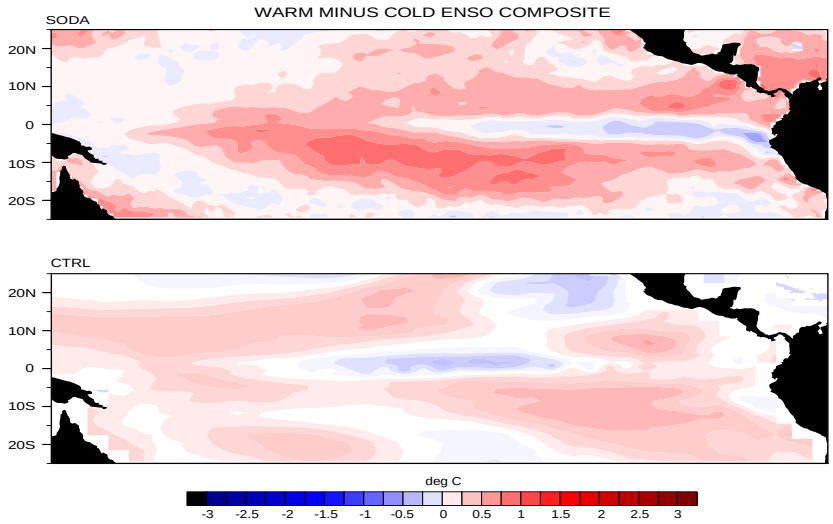

Figure 3.10: Warm minus cold ENSO anomaly composites of annual mean SST for observation and the CTRL simulaion. Details of the compositing procedure are given in the text.

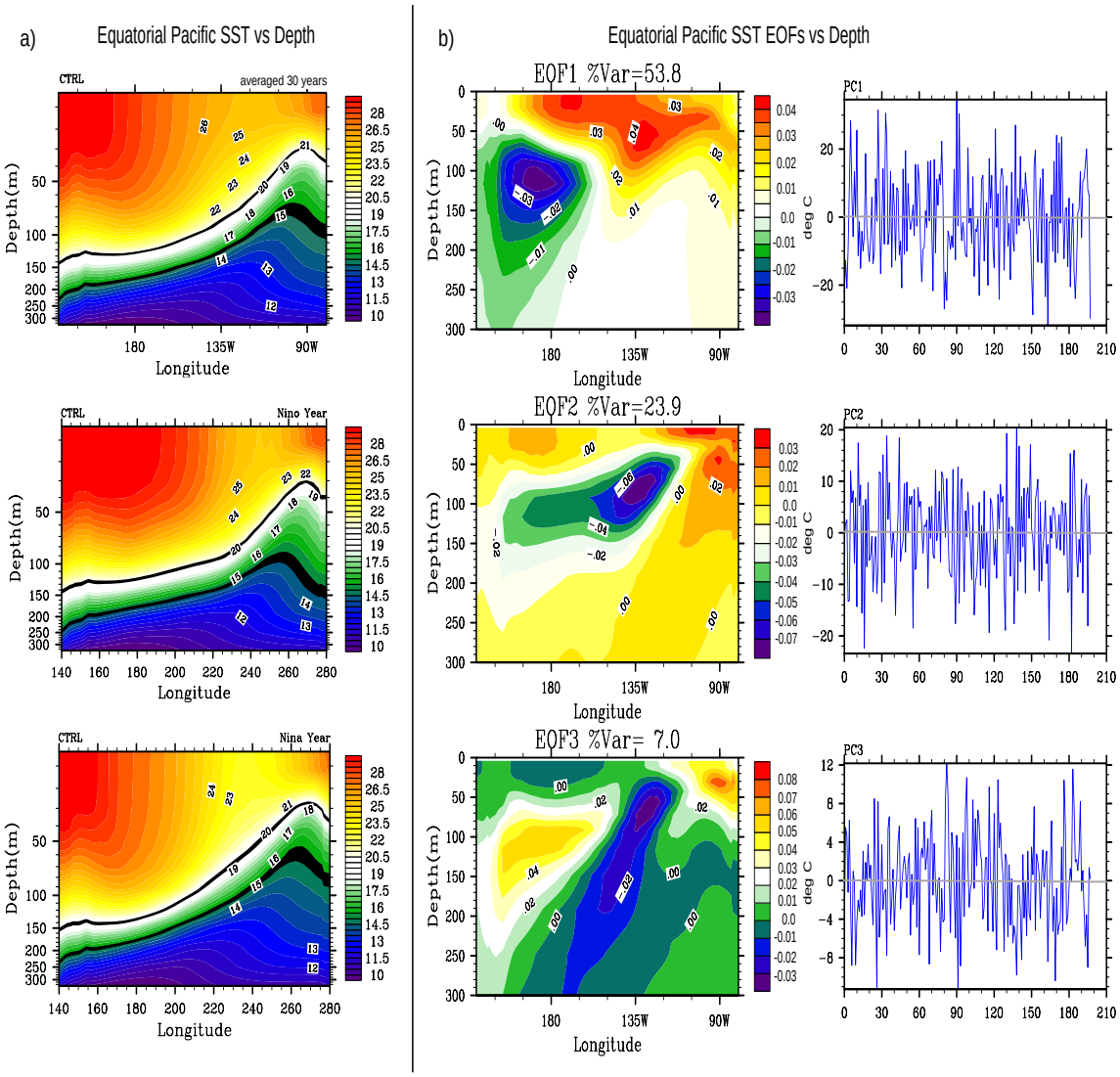

Figure 3.11: a : The ocean temperature-depth profile for 30 years averaged, Nino year and Nina year (left column). The thermocline depth is identified as the depth of the isotherm 20°C (seasonal thermocline) and depth of the isotherm 15°C (permanent thermocline) and are highlighted with a solid black line. b : Three leading EOFs mode (middle column) and its PC time series (right column) of zonal cross-section of the ocean temperature vertical profile for entire time series CTRL simulation. The Equatorial Pacific is the area of 5°N-5°S, 120°E-80°W.

mocline depth in the eastern Pacific and shallower in the western Pacific, and the opposite is true for cold ENSO (La Niña). In other words, the thermocline is rather flat during El Niño and having a steeper slope during La Niña event. The slope of the simulated isotherm can be identified from the isoline along 160°E-95°W. However, the subsurface temperature above 50 meters depth is much easier to be compared during the warm and cold event. During the warm event, the intrusion upwelled water occurs in the eastern Pacific (along 110°W for all seasons, while during the cold event seems to move towards west). From the seasonal subsurface ocean temperature distribution (not shown), the 30-year average subsurface ocean temperatures exhibit a similar structure like cold ENSO condition during spring to summer, but showing a warm ENSO characteristic during the fall to winter.

In Figure 3.11b, three leading EOFs mode of vertical profile ocean temperature in the CTRL simulation based on annual SST data up to 300 meters depth are displayed. Generally, three EOFs of the CTRL simulation show a variability of ocean temperature at a depth of 110 meters in the west (around date line), in central Pacific (around 135°W) at 80 meters depth, and variability at surface ocean up to 50 meters depth in the east (90°W). The first EOF which explains 54% of the total variance shows a dominant structure of upper ocean temperature between eastern and western equatorial Pacific. The dipole pattern between east and west describes the general feature of thermocline depth mentioned above. The 2^{nd} EOF exhibits a variability for the central Pacific subsurface ocean temperature, which is explained by 24% of the total variance. While the 3^{rd} EOF only explains 7% of the total variance.

Overall, the amplitude and zonal extent of equatorial SST variations associated with ENSO are relatively well simulated in CCSM3 with respect to observations in spite of the standard deviation of the Niño-3.4 SST index, which is increased in the simulations. It should also be noted that the ENSO periodicity in CCSM3 is shorter than observed. Moreover, the main deficiency of the CTRL simulation is the excessive equatorial confinement of SST responses relative to observation.

North Pacific SST Mode (PDO)

The computed EOFs based on the annual SST over the North Pacific (20°N-80°N, 140°E-120°W) are shown in Figure 3.12 both for observation and the CTRL simulation. As in the case of Pacific variability in the previous section, a comparison of the leading pattern, PC time series and power spectrum analysis are presented.

As expected, the leading EOF within the region resembles the pattern of the North Pacific Mode/NPM which is referred also to as the PDO pattern (*Mantua et al.*, 1997). The PDO is marked by a "see saw" warm-cold relation between the western and the eastern North Pacific ocean. The 1^{st} EOF of observed SST explains ∼22% of the total variance. The feature is similar to the leading mode and linked to ENSO-like Pacific decadal variability pattern which was discussed in the previous section. The second mode, which accounts for about 12% of the total variability, is marked by the SST fluctuations along the subtropical front with an opposite sign of SST variability over Gulf of Alaska and Bering Sea. The third mode with a weak monopole structure accounts for 10% explained variance.

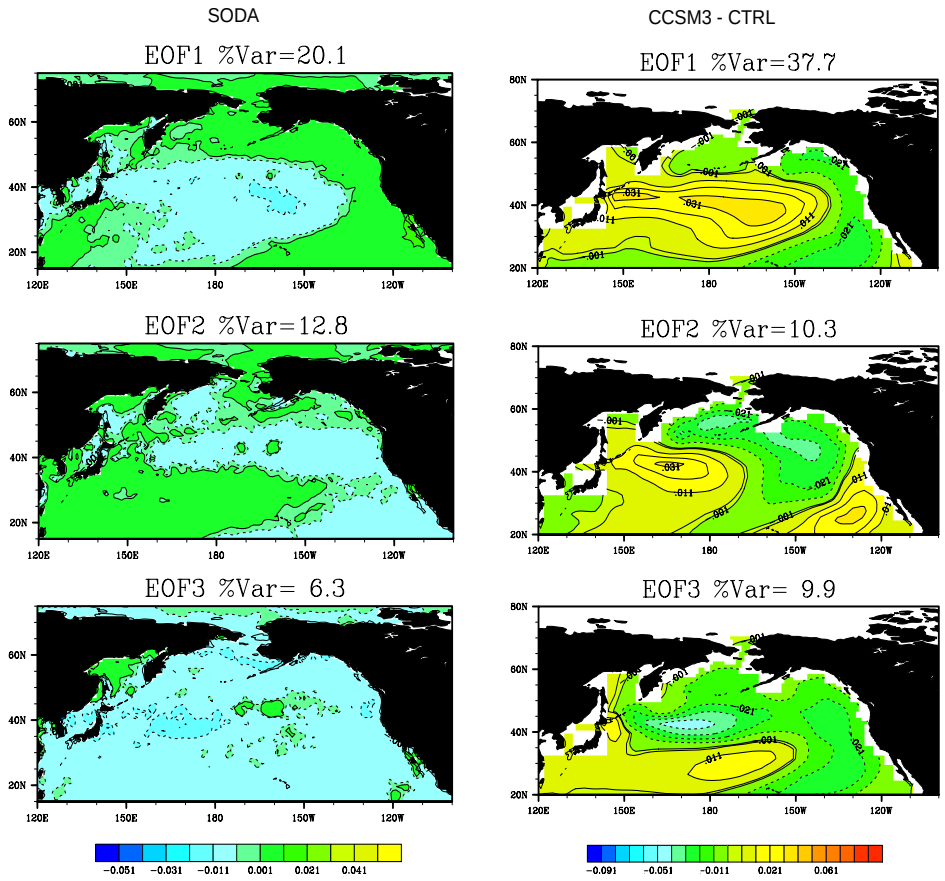

Figure 3.12: North Pacific leading EOF pattern of annual SST for observations and the CTRL simulation. The EOF patterns are obtained as in Figure 3.2 with contour interval 0.01.

Compared to observations, PDO patterns over the 198 years of the CTRL simulation show relatively similar features. The 1^{st} EOF presents a PDO structure explaining 39% of the total variance. The spatial correlation among them is 0.74 (Table 3.1). The 2^{nd} EOF which accounts for about 11% of the total variance shows an independent structure and has no association with the three leading modes in the observation. The 2^{nd} mode is pictured by the opposite sign of SST variability over Gulf of Alaska and Bering Sea with SST over the western North Pacific and south east Pacific sectors. The 3^{rd} EOF, which explains ~10% of the total variance, seems to be in an association with the structure of the 2^{nd} mode of the observed SST. This structure has a correlation of about 0.64, however, it is also correlated with the 3^{rd} mode with 0.53. The opposite sign between subpolar - subtropical North Pacific with tripole structure SST appears rather strongly in comparison to observation.

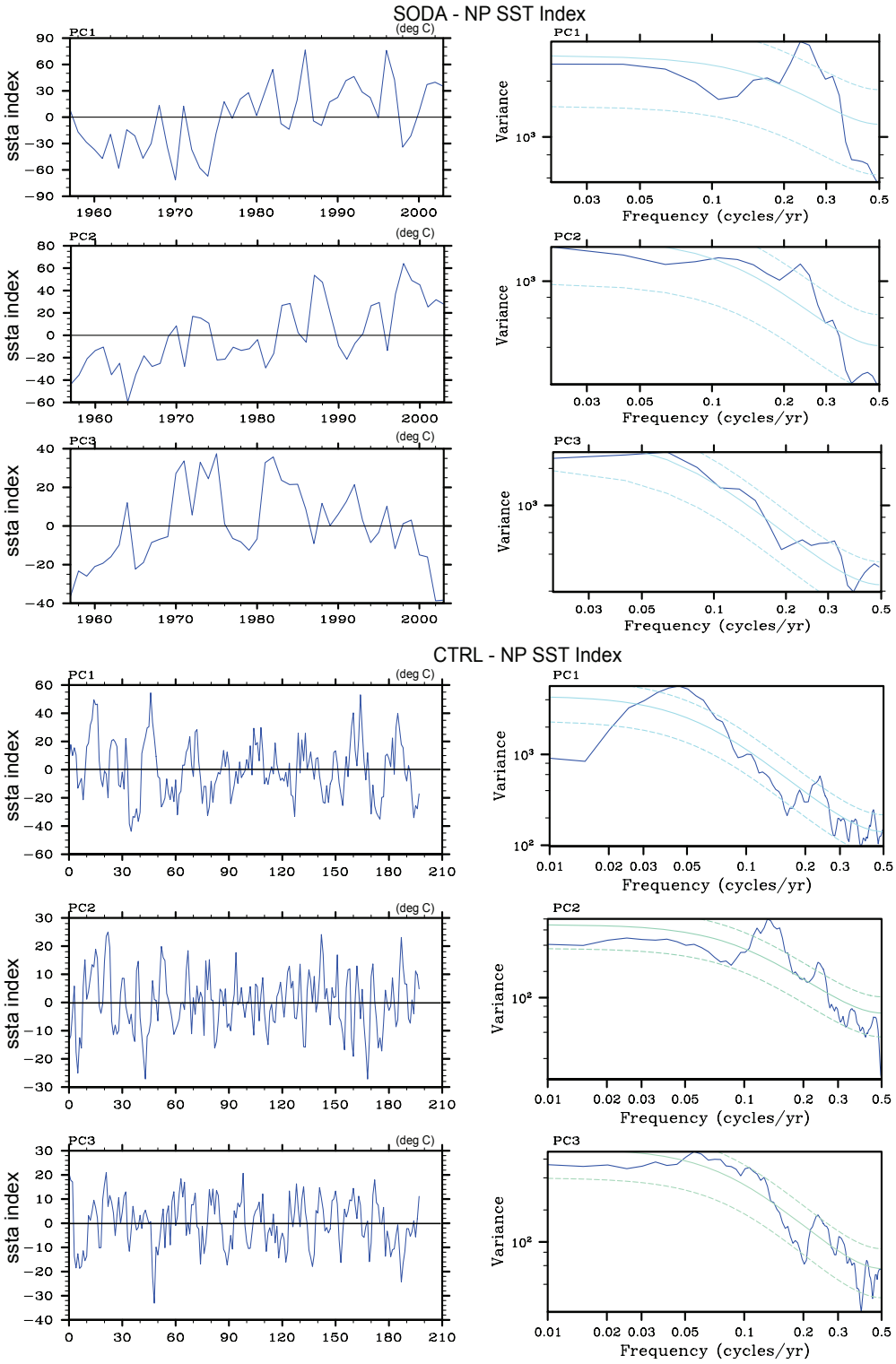

Figure 3.13: Left panels: time series of the North Pacific SST Index (PC series). Right panels: power spectra analysis for observations and the CTRL simulation; upper half SODA, lower half CTRL simulation.

SODA/CTRL	EOF1	EOF2	EOF3
$EOF1$	0.74	0.01	0.20
$EOF2$	–0.42	–0.17	0.64
$EOF3$	0.10	0.34	0.53

Table 3.1: Spatial EOF pattern correlation of North Pacific SST : Observations vs CTRL simulation.

The PC1 time series of observed SST shows a decadal variation with the dominant period of ∼10 and ∼24 years. However, the power spectral analysis shows that an inter-annual variability (∼5 years cycle) is enhanced (Figure 3.13) and the decadal variability is not in a significant variation (within red noise). It perhaps due to the observed SST time series which is too short, so that the low frequency variability does not appear significantly. From the PC1 time series, the climate shift from a cold regime (1957-1976) to a warm regime (1977 to 1996) is clearly visible. The PC2 time series exhibits inter-annual to decadal variations such in the leading mode, which is also shown by the power spectra analysis. The PC3 time series shows a similar variability. Additionally, it should be noted that in the observation, that the basic variability is essentially red noise.

In the model, the PC1 time series is associated with a decadal periodicity of ∼22 years as well as inter-annual variability of ∼4 years. However, the simulated CTRL PC time series fluctuate with a strong oscillation. The PC2 time series has inter-annual variability (4 and 7 years). The PC3 time series also shows an inter-annual to decadal variability.

3.2 Northern Hemisphere 500 hPa Geopotential teleconnection pattern

The traditional formulations of the Atmospheric teleconnection patterns are described by EOF/rotated EOF formulations that use time variations of fixed pressure or geopotential patterns. To examine model performance on atmospheric teleconnections over the Northern Hemisphere, the ERA40 reanalysis data is used for comparison. The rotated EOF (REOF) analysis has been applied to annual winter averaged (DJF) 500 hPa geopotential height. The domain area is the Northern Hemisphere north of 20°N. The output of conventional REOF analysis are spatial patterns (REOFs) which is orthogonal and time series. The REOF patterns are presented with their associated time series as well as power spectral analysis.

Figure 3.14 and Figure 3.15 show three leading patterns in the ERA40 dataset and in the CTRL simulation, respectively. The first leading mode of ERA40 data presents the structure of the North Atlantic Oscillation (NAO) which is dominant over the North Atlantic ocean and west Europa continent (*Barnston and Livezey*, 1987). This feature is similar to the NAO pattern of *Hurrell et al.* [2003] as well as to the pattern of the Northern Annular Mode (NAM) of *Wallace and Thompson* [2002], which is also referred to as the Arctic Oscillation (AO). There

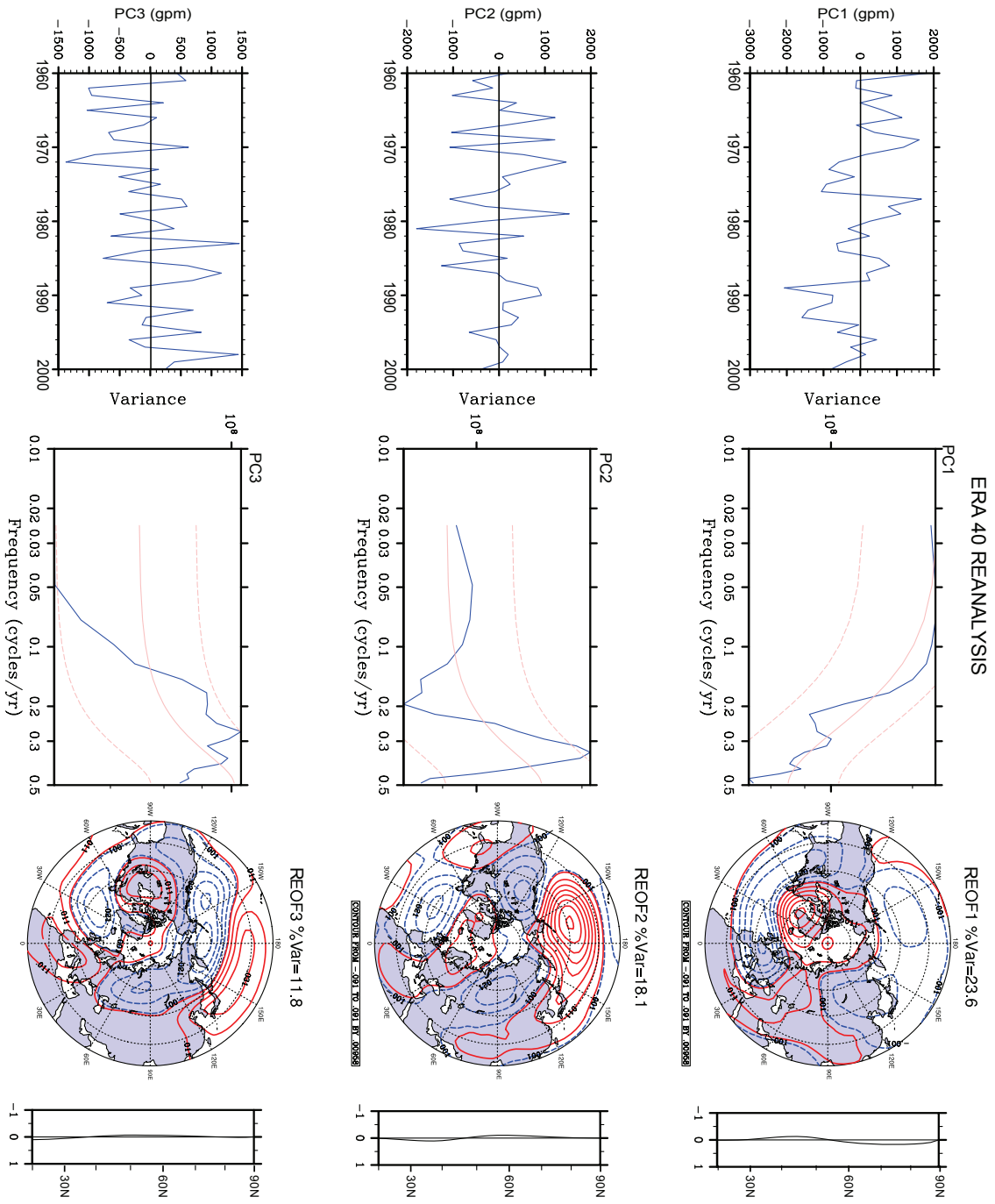

Figure 3.14: From left to right : PC time series, power spectral analysis, REOF pattern and zonal average of Northern Hemisphere winter 500 hPa geopotential height leading REOF for Observation (ERA40 reanalysis). Rotated EOFs is applied by using Kaiser row normalization and the varimax criterion (see description in the Appendix 7.1). The REOF patters are computed via a covariance matrix and presented as normalized eigenvector with contour interval 0.01. Solid red (dashed blue) line denoted a positive (negative) eigenvector.

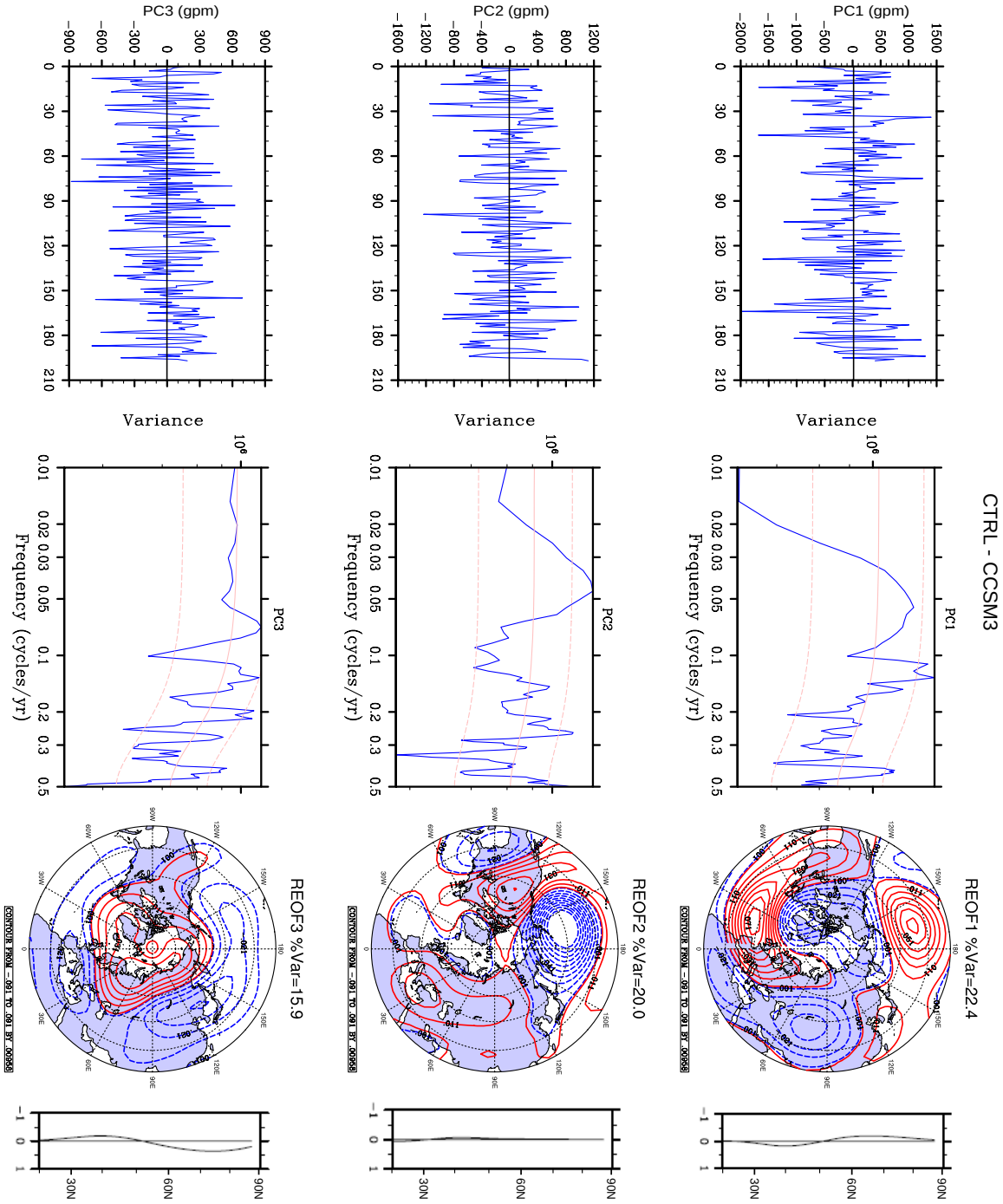

Figure 3.15: Northern Hemisphere 500 hPa geopotential height leading rotated EOF pattern for CTRL simulation. The description is the same as in Fig 3.14.

has been controversy in the literature as to whether the Northern Annular Mode (NAM) or the North Atlantic Oscillation (NAO) represents the better paradigm for explaining climate variability over the North Atlantic/Europe region (*Wallace and Thompson*, 2002). In this case, since the center of action in the North Pacific remains weak, hence, here the first EOF is defined as the NAO pattern. The NAO pattern in the leading mode explained 24% of the total variance within the domain. The associated PC time series and the spectral analysis of the observed leading pattern exhibit decadal (5 - 20 years) and inter-annual (3 year) variability, however, this variability is not significant as it lies within the red noise. The 2^{nd} REOF shows a dominant pattern over the North Pacific region and the Rossby wave train could also be detected which propagates from the North Pacific-North America-and ends up in the west Atlantic. This pattern is also very similar to the PNA teleconnection pattern described by *Wallace and Gutzler* [1981] and comparable with *Straus and Shukla* [2002]. The PNA teleconnection pattern is a climatological term for a large-scale weather pattern with two modes, denoted positive and negative, and which relates the atmospheric circulation pattern over the North Pacific Ocean with the one over the North American continent specially during winter time. This PNA pattern accounts for 16.6% explained variance and has variability at about 3 years. The 3^{rd} REOF shows apparently a structure of North Pacific Dipole mode, which is characterized by a north-south dipole of 500-hPa geopotential anomalies over the West North Pacific sector. The 3^{rd} mode is explained by 14% of the total variance and has a periodicity about 3 year cycle. However, this mode has less signal over the west Atlantic but the propagation of Rossby wave is moved towards polar region.

In the model, the REOFs analysis shared teleconnection features and rather distinct with observation. The 1^{st} REOF which accounts for 30% explained variance seems to represent a NAM - like pattern with a strong center of action over the North Pacific and over the Euro - Atlantic sectors. The NAM-like structure of the 1^{st} REOF is rather centered towards Canada. By definition, the Northern Annular Mode (NAM) is the first EOF of sea-level pressure (SLP) north of 20°N (*McAfee and Russell*, 2008). Positive values of the index are associated with higher pressure in the mid-latitudes, lower pressure over the pole and stronger, more zonal westerly winds. The associated time series PC1 shows that this pattern has predominantly inter-annual variability (2 and 8 years). The 2^{nd} REOF exhibits a PNA pattern which is visible with a strong negative signal over Canada and the Aleutian region and is significantly more zonally localized than the leading REOF. This pattern explains 18% of the total variance with a periodicity of inter-annual variability (4 years) as well as low frequency variability (25 years). The 3^{rd} REOF shows a distinct pattern with a strong signal dominating over the Arctic ocean which is virtually identical to the Arctic Oscillation pattern obtained in *Thompson and Wallace* [1998] as well as described in *Corti et al.* [1999]. The features of the AO are shown as the dominant variability over Arctic ocean surrounded by opposite sign of normalized geopotential field over North Pacific and North Atlantic either a polar low surrounded by a high pressure belt, and a deep dipole pattern, or vice versa. This pattern is characterized by a significantly stronger zonal asymmetry in the 60°-90° latitude band. The PC3 time series shows a modulation either an inter-annual variability (2-8 years) as well as low frequency (15 years).

Chapter 4

Response of the Pacific's climate system to 2 Sv freshwater discharge in the North Atlantic

4.1 Response of Pacific ocean

Freshwater discharges in the North Atlantic generally yield a global response of the climate system to the magnitude of the perturbation, i.e., to the reduction of the AMOC as well as in the Pacific basin's SST. In this chapter, changes in the ocean circulation in the Atlantic and Pacific-Indian ocean will be investigated. First, altered meridional overturning circulations are analyzed with respect to their structure and their time scale. Then, the climate variability on inter-annual and decadal time scales will be discussed, in particular during phases of an abrupt drop in SST in the North and in the equatorial Pacific. Moreover, the possible mechanisms, which are involved in those changes will be explored.

Response of Atlantic and Pacific MOC to freshwater forcing

The time series of AMOC intensity which is defined as the maximum meridional overturning stream function value is presented for the North Atlantic (30°-90°N), and North Pacific oceans (30°-80°N) as seen in Figure 4.1. For the North Atlantic, the represented region describes the area where the formation of North Atlantic Deep Water takes place. While for the North Pacific, the represented region is associated with a "shallow" meridional overturning cell, as described in *Nof* [2002]. From time series in Figure 4.1a, the maximum of AMOC ranges from 14 - 18 Sv in the CTRL simulation, while in the FN20 simulation is varies in the range of 3 - 18 Sv. Three periods of the AMOC resumption can be readily distinguished. In response to the freshwater forcing, the temporal evolution of the AMOC shows a strong reduction of the AMOC from the start of the perturbation up to about model year 150. The AMOC reaches a nearly collapsed state within 100 years (when the maximum 2 Sv freshwater perturbation is delivered in the North Atlantic) and its intensity is reduced to about 2-4 Sv. The period during which the AMOC is nearly collapsed is denoted as Period A. Period A is followed by two recovery phases, those are Period B and C. From Period A to B, the AMOC intensity ranges from 4-12 Sv with an steady increase. Period B is denoted by a quasi-stable climate

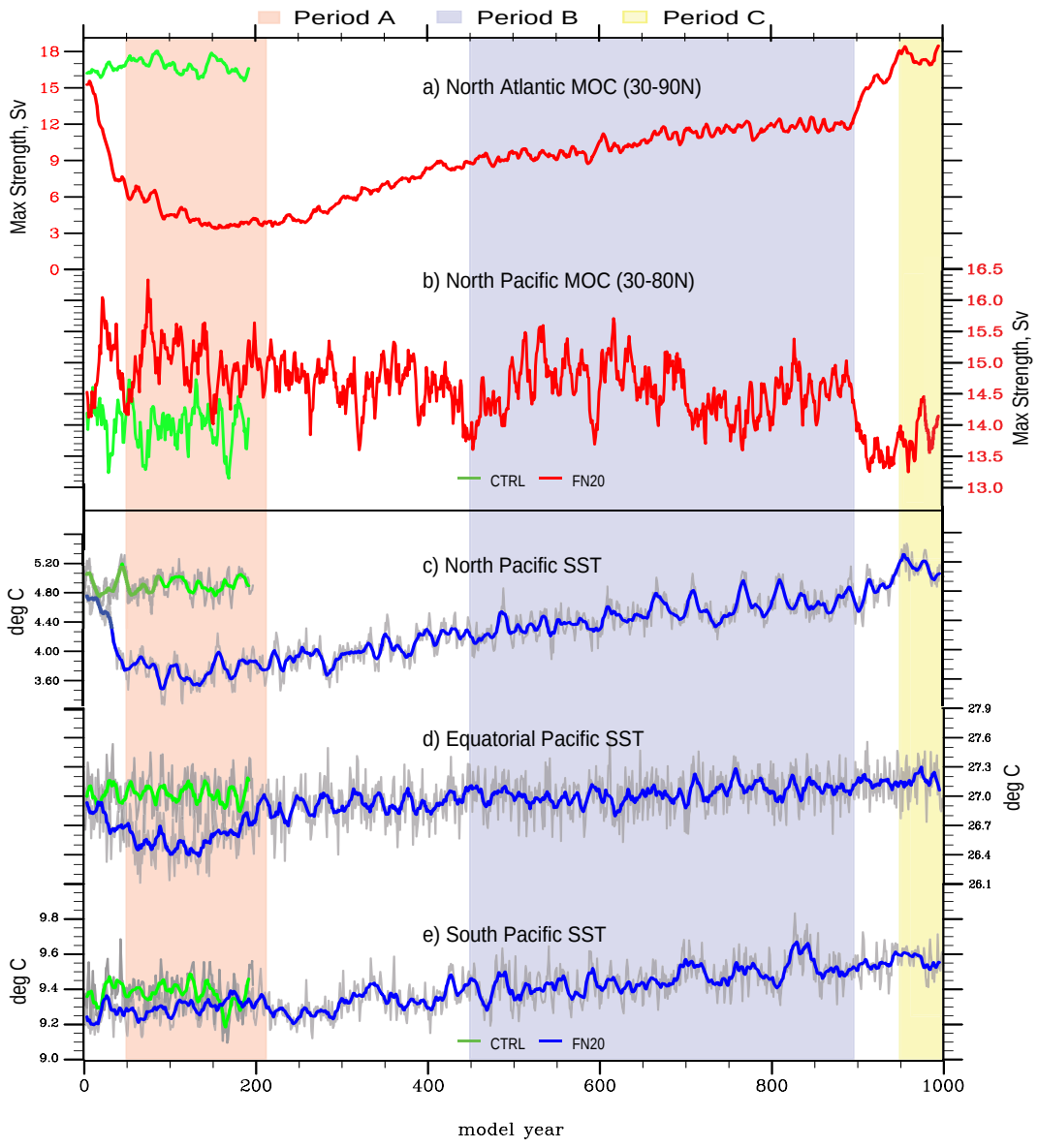

Figure 4.1: Time series of North Atlantic, and North Pacific ocean maximum MOC (a,b) and sea surface temperature in the North, Equatorial, and South Pacific (c,d,e) in response to freshwater discharge in the North Atlantic. Time series are smoothed with a 10-yr running mean. The background color indicates the three consecutive phases (A to C) of resumption process of the experiments.

equilibrium from model year 450 to 900. After an abrupt increase of the AMOC, Period C is again similar to the CTRL conditions. The mechanisms involved in the recovery are discussed in *Renold et al.* [2010].

Since in the POP model the computed MOC is only available for Global and Atlantic basin, and to calculate the MOC for every basin need some parameters, which are not available in

the CCSM3 model output i.e., bolus advection, here therefore, we assess the Pacific MOC from global and Atlantic MOC variables. To investigate the response of the Pacific and Indian ocean circulation to the freshwater perturbation in the North Atlantic, the residual world MOC is computed by subtracting the Atlantic MOC from the Global MOC in the POP model.

To describe the maximum strength of the North Pacific meridional overturning circulation (PMOC), the area has been limited to 30°N - 80°N to cut out the Indian Ocean MOC. The resulted MOC is assumed to represent the PMOC. From Figure 4.1b, the maximum strength of North Pacific ocean exhibits about 13 - 14 Sv for the CTRL simulation and range from 13 - 16.5 Sv in the FN20 experiment. The time series shows a different behavior from the one in the North Atlantic. The PMOC shows an increase in its maximum strength during Period A and B in comparison to CTRL. The highest fluctuation appears during the perturbation period. The strength of PMOC fluctuates in a range of 14.0 to 16.5 Sv. It has been argued that decadal time scale variations suggest a possible "bridge" involving fluctuations in the shallow PMOC, which links to the tropical pycnocline to the regions of subtropical subduction (equatorward flows in the pycnocline), equatorial upwelling, and poleward surface Ekman flows (*Liu and Philander*, 1995; *Zhang and McPhaden*, 2006). Period B shows a similar behavior with a reduced PMOC intensity in range of 14.0 to 15.5 Sv.

The similar way has been used to achieve the annual mean of Eulerian stream function in the Pacific basin, that is subtracting the Atlantic MOC from the Global MOC. The resulted MOC is assumed to represent the Pacific and Indian Ocean MOC. From Figure 4.2b, the structure of Pacific and Indian ocean interior water flow is described by general southward transport resulted from an anticlockwise upward motion to a range-depth of about 1 to 4 km depth and northward transport in the surface ocean for upper 800 m in the CTRL simulation. Its feature is similar with the suggested (shallow) Pacific-Indian MOC (*Nof*, 2002; *Wunsch et al.*, 1983). In Period A, the Pacific-Indian MOC shows a strengthening of surface shallow MOC up to about 14 Sv, particularly in the tropical-subtropical region 20°S-20°N. The intensification of shallow MOC is also shown in the region of 50°-55°N which is probably associated to the intensification of the circulation in the subpolar gyre. During Period A, the North Pacific Subpolar gyre exhibits a deepening of the mixed layer depth (MLD), which appeared around Gulf of Alaska. The deepening of the MLD in the area of Gulf of Alaska may indicate an intensification of the Alaska Current, while the shallow MLD in the east of Japan might be related to a weakening of Oyashio Current and Kamchatka Current. The deepening of the MLD in the subtropical gyre north off-equatorial Pacific indicates the intensification of the North Equatorial Current. The intensification of the ocean current is driven by intensified atmospheric circulation anomalies over the subarctic front (around 40°N-42°N) and in the north equator subtropical front which is eventually increasing the shallow PMOC of the upper ocean and intermediate water. As it has been suggested in several studies that the intermediate/deep water formation tends to resume in the North Pacific when the AMOC is suppressed (*Timmermann et al.*, 2007; *Krebs and Timmermann*, 2007; *Mikolajewicz et al.*, 2007). Moreover, the structure of southward intermediate water transport is shown to be suppressed by the intensification of upper ocean circulation up to 1.5 km depth (in the CTRL simulation it is about 800 m). From Period B to Period C, structure of meridional cross-section of MOC is relatively similar to CTRL simulation, and the differences are gradually reduced and eventually yields less differences in the period C.

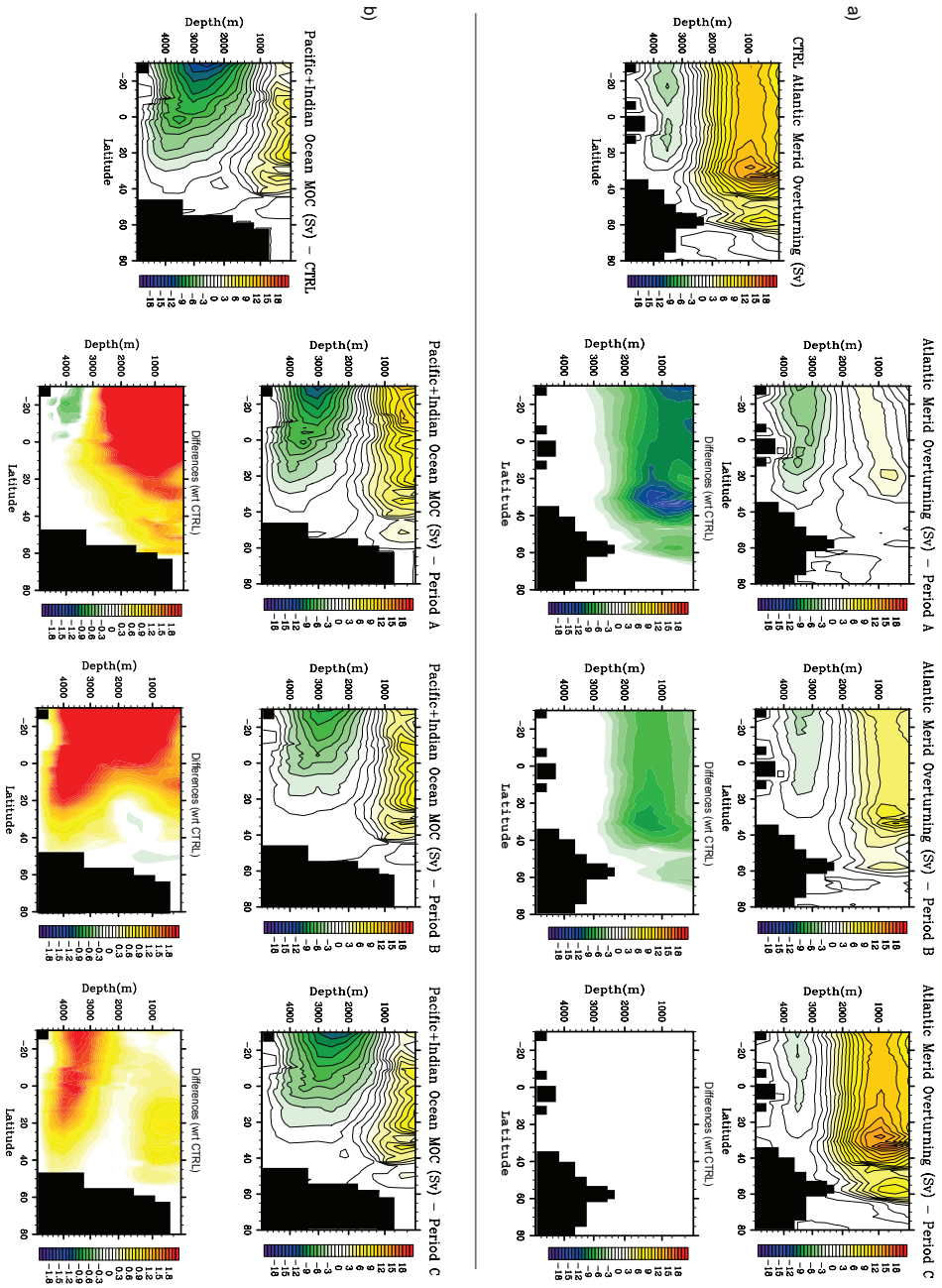

Figure 4.2: The annual mean of Eulerian stream function of Atlantic MOC (a) and Pacific+Indian Ocean MOC (b). The Pacific+Indian Ocean MOC is obtained by subtracting the Atlantic MOC from Global ocean MOC. Positive (negative) values show a clockwise (anticlockwise) circulation. Contour interval is 1 Sv. The differences of each period are calculated with reference to each basin's CTRL MOC simulation.

Response of ocean temperature and wind stress field

The response of Pacific Ocean SST is depicted in Figure 4.3. The 20-year averaged SST anomaly exhibits a general cooling over Northern Hemisphere and warming over Southern Hemisphere during Period A. During this period (Figure 4.3a), a decrease of the SST is found over the North Pacific 40°-60°N particularly over East Japan and in the Subpolar region and over the west coast North America. A decrease of SST is also found in the equator-tropical region. In contrary, in the Pacific Southern Ocean shows a different feature of SST, where an increase of SST is found around subtropical region (10°-645°S), in particular in the west coast of Peru to Chile and around New Zealand and south of Australia. However, the Antarctic circum polar region shows a decrease of SST.

Period B shows a similar feature as in Period A but with less amplitude of SST differences (Figure 4.3b). In general, reduced amplitude are shown in those area mentioned previously. During Period C, an increase of SST is found in the most Pacific's basin except a cool SST in the North Pacific east of Japan which shows and warm SST in the eastern Pacific (Figure 4.3c). A slightly cool SST is also found in the eastern Pacific.

Apparently, the degree of cooling (warming) in the North Pacific coincides with the degree of cooling (warming) in the North Atlantic as shown in the three periods of AMOC resumption. These results are in qualitative agreement with the study of *Trenberth et al.* [2006], where the North Pacific is observed to have a cooling trend over 50 years and is suggested to be associated with a cooling (warming) trend in the North (South) Atlantic that it might be caused by a weakening of AMOC. Accordingly, an atmospheric teleconnection or oceanic interconnection between North Atlantic and North Pacific is suspected as a possible cause (*Trenberth et al.*, 2006).

Figure 4.4 shows seasonal SST differences with respect to the CTRL simulation for each period. During Period A, the North Pacific's SST, e.g., in the subpolar region, eastern North Pacific and north off-equatorial Pacific region are decreased (by up to 5°C) in all seasons except in the summer time (JJA). During summer, SST are increased (up to 2°C) in the eastern equatorial Pacific but colder in the west. The excessively cold SST is shown in the spring time (MAM) over those regions, particularly in the North Pacific subpolar region and the entire equatorial Pacific. During Period B, the decrease of SST in the North Pacific is reduced but remains a cold spot in the Bering Sea, while in the Period C, the seasonality of SST shows no significant differences but slightly warming in the North Pacific subpolar region.

A 20-year SST and seasonal differences of each period with respect to the CTRL simulation confirm that the strong and widespread North Pacific cooling is in association with the cooling over the North Atlantic (see *Renold*, 2007). These inter-basin cooling occurred a few years after the freshwater discharged reaching the maximum perturbation of 2 Sv in model year 100. Generally, the SST responds differently over the North Pacific and South Pacific which is similar to the response of North Atlantic and South Atlantic (see *Stocker et al.*, 2007; *Renold et al.*, 2010). This feature describes a north-south oceanic seesaw link during abrupt climate change, which has been suggested as the seesaw theory (see *Stocker and Johnsen*, 2003). The North Pacific and the tropics show a significant response during freshwater discharge, while

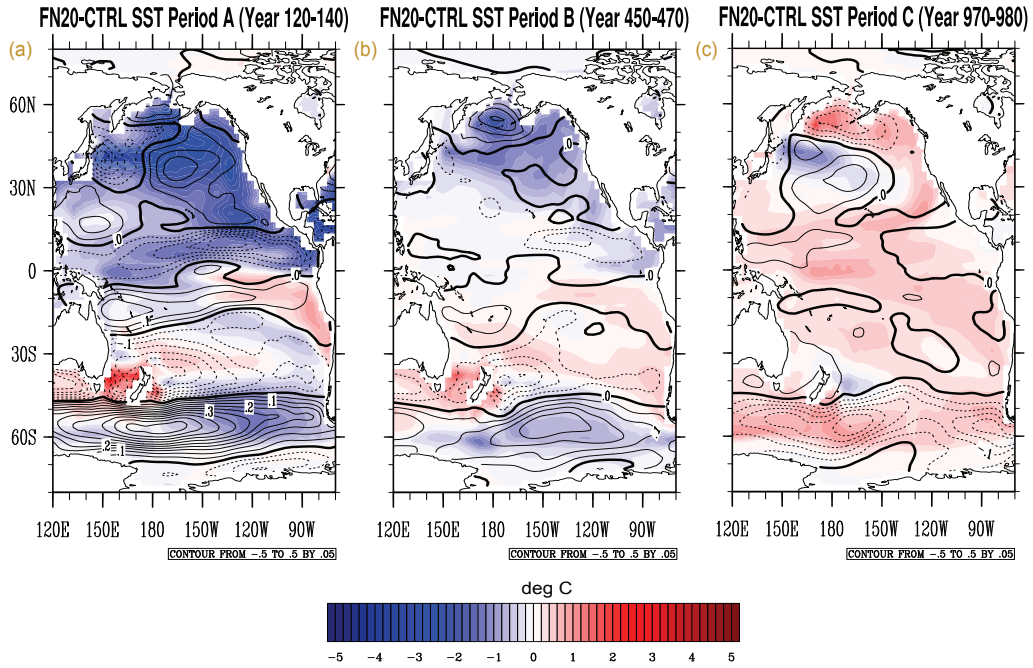

Figure 4.3: Pacific's SST and zonal wind stress difference pattern of (a) Period A, (b) Period B and (c) Period C with the CTRL simulation. SST are shaded with colour interval 0.05°C and zonal wind stress anomalies are contoured with interval 0.02 dyne.cm^{-2}.

the southern Pacific does not react as strongly as those parts.

Over the North Pacific, a decreased SST in the North Pacific region is associated with a strengthening of westerly component of the zonal wind stress over the subpolar front region. A large positive zonal wind stress difference over the Bering Sea and the Northeast Pacific is collocated with the maximum SST cooling during Period A. Reducing zonal wind stress enhancement in Period B and C are concurrent with reduced cooling in the North Pacific. The west coast of North America shows a feature of SST patterns that varies along three periods. The cold subsurface ocean temperature at 150 m depth is found in the west coast of California extends westward to the north off the equator (not shown) as a consequence of the subtropical gyre. It seems to be more intensive during Period A and B, while strong cooling east of Kamchatka Peninsula extends eastward along the oceanic front of 160°E apparently as a consequent upon an intensified subpolar gyre.

Within the tropics, Period A shows a large negative zonal wind stress difference, which indicates a strengthening of easterly along north equatorial Pacific. The enhanced of easterly component may indicate an increased activity of north-easterly trade winds, which occur a few decades after termination of freshwater perturbation. Increased north-easterly trade wind speed in the north east Pacific basin is also found with an enhanced easterly component across

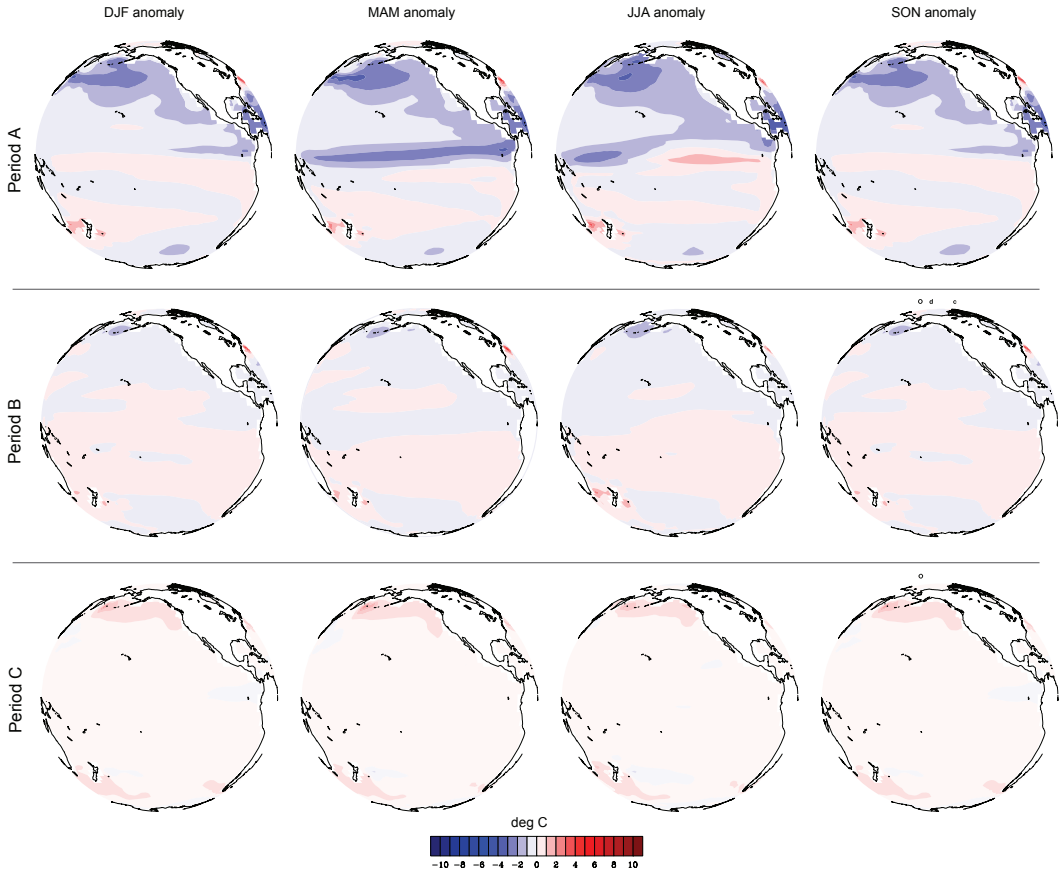

Figure 4.4: Seasonal mean of SST anomalies (shaded with colour interval 0.05°C) with respect to CTRL simulation.

the Isthmus of central America (not shown). The enhancement of the zonal component of wind stress field is collocated with enhanced cooling in the north off-equatorial Pacific. Since the subtropical gyre is weakened during Period A, which can be assumed from the shallowness of the MLD, it might be that the intensified north-easterly trade wind is mainly responsible for the cooling in the north of equatorial Pacific. This result is similar to previous studies, which implied that the intensified north-easterly trade winds across the Central American Isthmus advects anomalously cold and dry air from the Atlantic and decreases SST in the eastern tropical North Pacific by enhancing surface turbulent heat fluxes, mixing, and upwelling with a distinct seasonality (*Zhang and Delworth*, 2005; *Okumura et al.*, 2009). On the other side, during Period A and B, the southeasterly trade winds from Peruvian coast seem to be stronger than in CTRL or Period C. This intensification of the south easterly trade wind extended up to South West Pacific.

Our results of these ocean-atmosphere interaction features agree with the pattern associated with North Pacific Decadal variability (e.g. *Trenberth*, 1990; *Mantua et al.*, 1997). Wind stress extension and its magnitude over the subpolar front region are suspected to play a role (*Mc-*

Gregor et al., 2007; *McGregor et al.*, 2008) in the SST decadal variability. The overall cooling of the Northern Hemisphere is likely to suppress the regional warming in the eastern Pacific nearby west coast America during Period A, while it appears gradually in the Period B and C.

Over all, intensified westerlies in the subpolar region and enhanced easterly wind over north off-equatorial Pacific region is responsible for the cooling in those areas. The same is true for the subpolar westerly wind and subtropical easterly wind in the Southern Hemisphere. Nevertheless, *Okumura et al.* [2009] reported that the North Pacific cooling is not preceded by westerly wind anomalies and the cooling tends to develop simultaneously in the CCSM2 simulation. This means that there is an internal oceanic process which initiates the rapid SST cooling. However, in contrast to all model simulations in their study, the ECHAM5-OMI simulation showed that westerly wind anomalies are associated with multi-decadal variations and appear to lead the SST cooling (*Okumura et al.*, 2009).

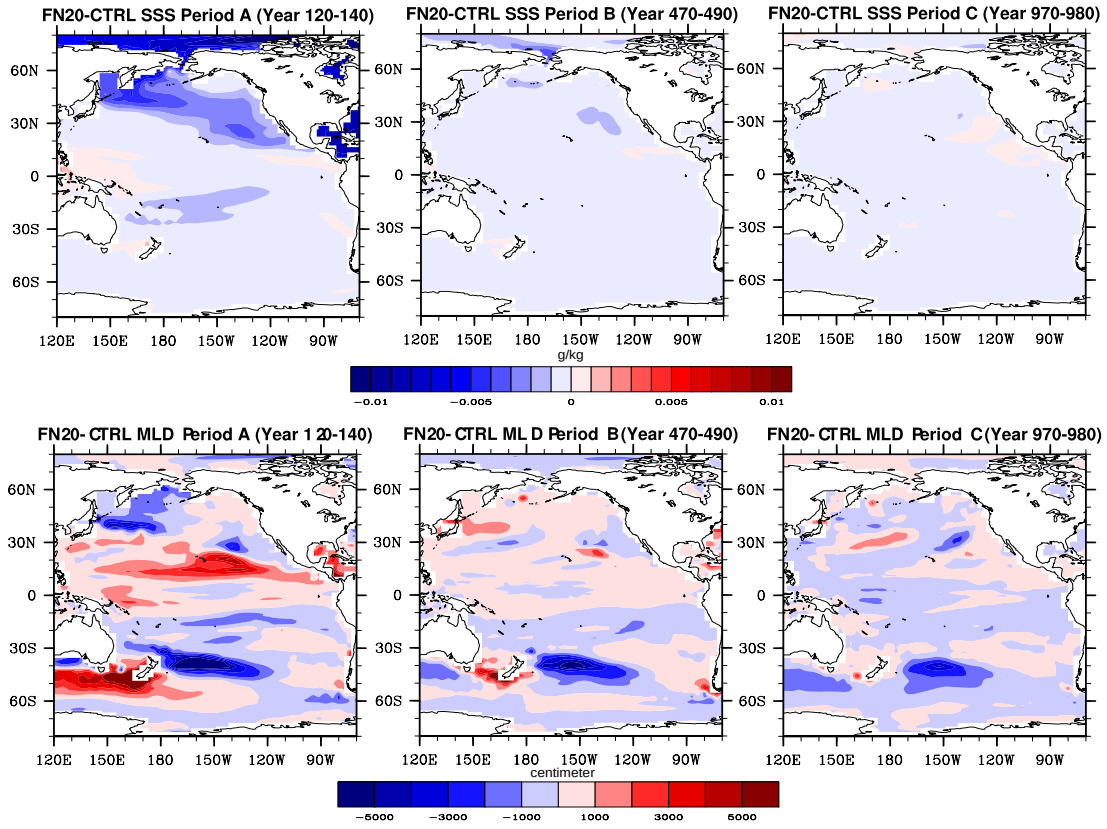

Figure 4.5: Sea surface salinity (top) and mixed layer depth (bottom) difference patterns between Period A, B, C and the CTRL simulation.

Salinity and Mixed Layer Depth

To assess the oceanic processes due to decreasing SSTs over the North Pacific, the sea surface salinity (SSS) is shown in Figure 4.5 (upper panel). During Period A, the SSS difference over the North Pacific subpolar region decreased (negative SSS anomaly) by about 0.004 g/kg, while in the North Atlantic and Arctic ocean, negative SSS anomaly reaching up to 0.01 g/kg. It seems that a freshening of ocean surface over this area is due to an intrusion freshwater from Arctic ocean through Bering Strait flow. Since this anomaly does not appear in the other periods, this supports an argument that there is an oceanic interconnection between North Pacific and Arctic ocean through Bering Strait by reversal hydraulically-controlled throughflow (*Hu et al.*, 2007), which transports part of cold and fresh Arctic water as a watercourse from North Atlantic (which is colder and fresher in comparison to North Pacific) during weakened AMOC. This is in agreement with *Hu et al.* [2007] who showed that a part of the freshwater flux anomaly applied to the North Atlantic is transported into the North Pacific through the Bering Strait by reversing throughflow. This inflow of cold and fresh Arctic water may have a significant impact on the heat and salinity balance in the North Pacific. The decreased SSS over the North Pacific subpolar region indicates reduced density differences (salinity contrast) between North Pacific - North Atlantic where it has been suggested as one of the possible mechanisms that may responsible or as an impact for such weakening of AMOC (*Stouffer et al.*, 2007).

Another indicator to investigate these cooling SST due to oceanic processes is MLD. Classically, the vertical structure of the upper ocean is schematically divided in two layers: a near surface layer where temperature and salinity are well mixed, and the deeper stratified ocean (*de Boyer Montégut et al.*, 2007). The distribution of near-surface mixed layer illustrates the active air-sea interaction, where the wind generates turbulence, cooling, or processes such as evaporation or sea ice formation from which result in an increase in salinity. The definition of the MLD based on a stratification criterion: the base of the mixed layer is usually defined as the top of pycnocline. Temperature stratification is commonly used to assume that the top of the thermocline and halocline have the same depth and thus together define that of the pycnocline (*de Boyer Montégut et al.*, 2007). However, this view is a simplified definition in comparison to the complex real ocean. There are some processes that affect the MLD. The MLD is deepened by the densification process in the ocean surface or mechanical energy input from wind. A deepening of the MLD is achieved by processes of the upper ocean stratification, whereas a shallowing of the MLD is achieved by increased upper ocean stratification because either surface warming or freshening, decreased surface wind speed and decreased winter cooling.

Regarding the three periods of the AMOC resumption, the 20-year averaged annual MLD difference patterns exhibit changes during Period A and C compared to the CTRL simulation (Figure 4.5: lower panel). In the CTRL simulation, A deep MLD is pronounced during the fall to winter in the North Pacific east of Japan and west California coast and shallows during spring (not shown). In summer, the MLD maximum occurs in the South Pacific near Circum Polar water. Those feature are in association with seasonal wind stress (not shown) in particular with the zonal component. During Period A, MLD apparently tends to be shallower up to 30 meters in the subpolar region, e.g., in the North Pacific east of Japan towards the north of the Bering Sea. A deepening MLD is found in the Gulf of Alaska (up to 10 meter),

eastern North Pacific (10 meter) and deeper up to about 50 meters in the subtropical region north off-equatorial tropics together with enhanced wind stress activity. Shallowing of MLD in the east of Japan may be caused by weakening atmospheric circulation, since the maximum wind activity displaced towards Aleutian Islands and generates a deeper MLD around Gulf of Alaska. This is also true for the equatorial western Pacific, where the model exhibits a deepening MLD in the area of subtropical gyre extended to the western tropical Pacific. However, the strongly increasing (up to 50 meters) MLD in the tropical North Pacific (10°N-30°N) is accompanied by an anomalous shallow mixed layer in the central Pacific down to 10 meters. Period B and C show no significant differences in regard to the CTRL simulation. We suggest that the deepening MLD in the North Pacific is associated with a sea level pressure drop in the Aleutian region (deepening Aleutian low) which in turn generates a strengthening wind stress over the sub-polar region (westerlies).

4.2 Response of Atmosphere

Sea Level Pressure, Wind 850 hPa, and Precipitation

The consistency of the North Pacific response in freshwater simulation is also shown in the sea level pressure (SLP), atmospheric circulation and precipitation. During the maximum perturbation, the deepening of the Aleutian low is intensified during winter and is displaced to the Gulf of Alaska (Figure 4.6). It is accompanied by enhancement of a cyclonic vortex over Aleutian basin (Figure 4.7). The location of this vortex is more visible and largest during the fall - winter, while spring and summer represent the circulation over the south subtropical gyre easterlies flow. In the southern Pacific Ocean, the atmospheric flow is dominated by westerly winds and anomalies are largest during boreal summer around Antarctica circum polar region where westerlies are strong. Those interhemispheric situations display a distinct seasonal dependence. An examination of the individual monthly means show that those circulations typically appear in September-October and persist through March-April. These features remain unchanged through the three periods, except the narrowing of North Pacific subtropical vortex during spring in Period A. Besides the deepening Aleutian low, anomalous high pressure that develops during Period A in the Caribbean Sea is expected to be responsible for enhancement of the easterly trade winds in the eastern tropical Pacific as mentioned earlier. This anomalous high pressure does not appear in the other periods. The tropical North Atlantic cooling induces anomalous high pressure around the Caribbean Sea that extends westward into the eastern tropical North Pacific, thereby intensifying northeasterly trade winds across the Central American Isthmus. These cross-Isthmus winds advect anomalously cold and dry air from the Atlantic and decrease SST in the eastern tropical North Pacific (*Okumura et al.*, 2009). It could be highlighted that the seasonality of the Aleutian low becomes stronger during Period A (not shown). However, the North Pacific's SST cooling, in contrast, does not show changes in its seasonality, while tropical SSTs show a somewhat stronger seasonal variation.

Climatologically, in the CTRL simulation (not shown), the total (large scale and convective) precipitation showed a high rate over the west Pacific and maritime-continent with two

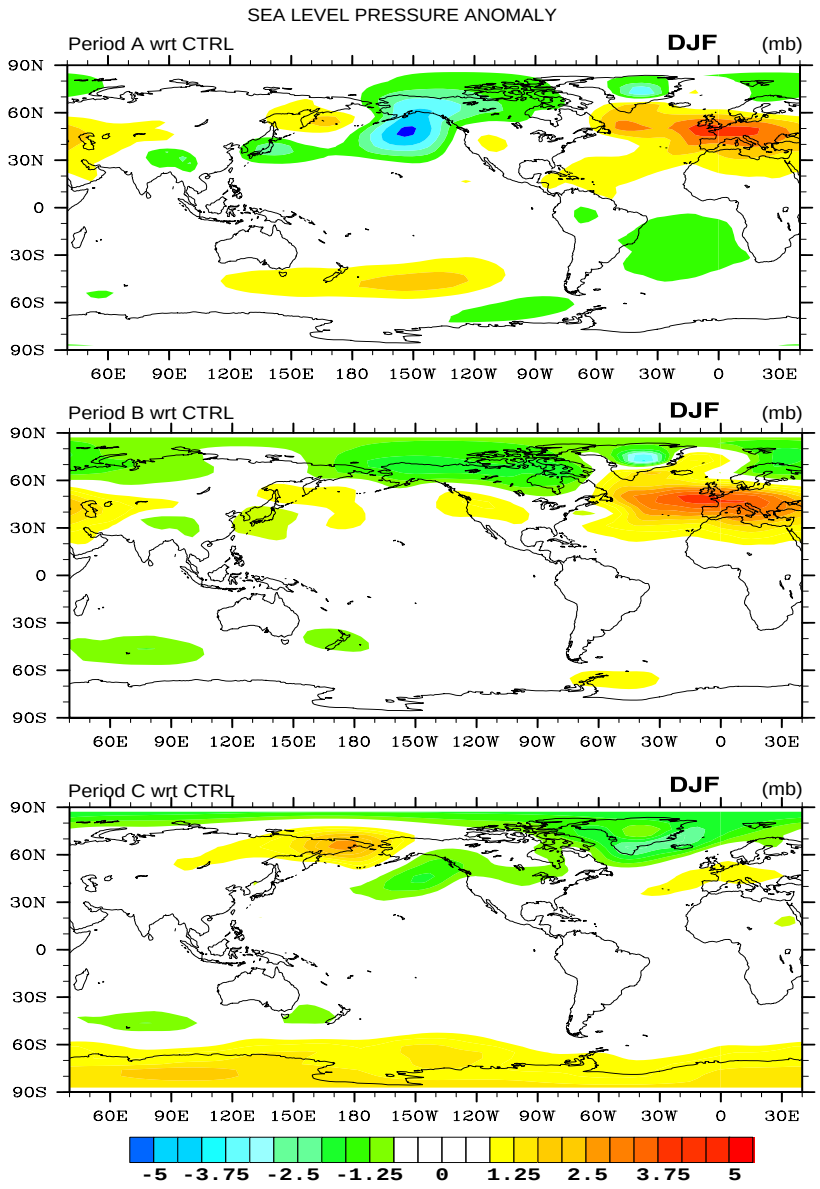

Figure 4.6: Sea level pressure differences between Period A (top), Period B (middle), and Period C (bottom) and the CTRL simulation, respectively. Anomalies less than 1 mb in magnitude are not plotted.

branches of zonal band extension north and south equator, which is associated with the location of Intertropical Convergence Zone (ITCZ) and in the subarctic front of the North Pacific, which is associated with large scale precipitation. The zonal bands of precipitation anomalies move north and south following the migration of ITCZ in the north and south equatorial Pacific. The eastern Pacific precipitation anomalies become more asymmetric about the equator during winter. This structure is stable for all seasons except in spring. During Period A, those structures are slightly disturbed where the zonal band of precipitation anomalies over equatorial Pacific is quite robust south of the equatorial line (Figure 4.7). Increased precipitation

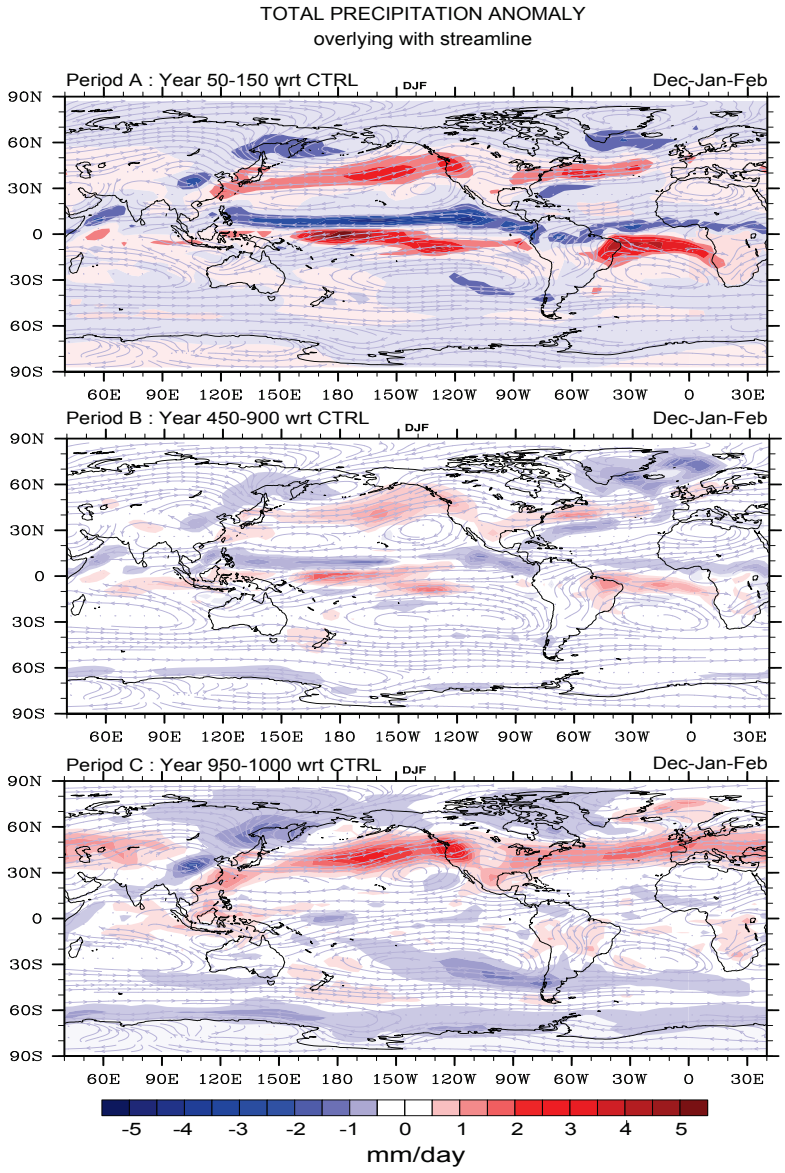

Figure 4.7: Total precipitation differences between Period A (top), Period B (middle), and Period C (bottom) and the CTRL simulation, respectively. Seasonal averaged streamline at 850 mb are overlied during Period A, B, C, respectively. The anomalies less than 0.5 mm.day^{-1} in magnitude are not plotted.

rate anomalies are also shown in the North Pacific region, namely, the east coast of China to the west coast of Canada. However, this increased in large scale precipitation is stronger in Period A and C than Period B. Additional changes are also visible i.e., a reduction of convective precipitation rate in the western equatorial Pacific due to enhancement of divergence wind over this area. The same is true in the location where easterly trade winds across the Isthmus central America. The convective precipitation is then centered and high in the south off-equatorial line extends from the maritime-continent, west Pacific to east Pacific along Pe-

ruvian coast. This indicates southward displacement of ITCZ in the eastern Pacific in the cold climate when the AMOC slows down.

4.3 Response of Pacific Climate Modes

4.3.1 Changes in ENSO properties and characteristics of El Niño/La Niña anomalies

Tropical Indo-Pacific SST variability responses to freshwater discharge in the North Atlantic: changes in the background state of SST

The leading EOF modes of tropical Indo-Pacific annual mean SST anomalies for the three periods are shown in Figure 4.8. In general, all patterns show an ENSO characteristic as described in Chapter 3, and the zonal extent of the SST pattern is similar with CTRL simulation. The 1^{st} and the 2^{nd} EOF patterns in Period A show a predominant Central Pacific and Eastern Pacific ENSO modes, respectively. The 1^{st} EOF which accounts for 43% of the total variance exhibits an SST variability centered in the Central Pacific. The associated time series of PC1 shows that up to year 150, the SST variability stays in a cold ENSO background state and rises again afterward. It seems that there is a "climate regime shift" around year 150 from cold to warm condition over the tropical SST during Period A. The temporal behavior of the PC1 time series (ENSO CP type) exhibit an interannual-decadal oscillations. The amplitude of the cooling SST is about 1.3°C on average. The following period (model year 150-210) shows that the background of state of the SST variability tends to stay in the warm ENSO.

The 2^{nd} mode with 17% explained variance describes a pattern of "cold tongue" in the eastern Pacific (EP ENSO type). This mode shows 8% more explained variance than in the CTRL simulation. The associated time series shows that the CT ENSO type is characterized by annual-inter-annual as well as a multidecadal variation (60-year for cold/warm episode). The amplitude of the SST anomaly reaches about 0.4°C. The 3^{rd} EOF which explains about 8.4% shows the tripole SST structure in the central Pacific, south and north of the eastern Pacific.

During Period B, similar patterns as in the CTRL simulation are found with high SST variability still in the central and eastern Pacific. However, the amplitude of the SST anomaly is decreased in the 2^{nd} mode and the explained variance of the leading mode is increased. The 1^{st} EOF accounted for about 47% of the total variance with a pattern very similar to the leading mode in the CTRL simulation. The center of action of this mode is located within the central Pacific but rather to the west. The amplitude of the SST anomaly in this region is about 0.7°C. The associated PC1 time series exhibits an inter-annual-bidecadal variation with more regular oscillations. However, it is also shown that there is a shift in the background state of SST in the year around 700. From model year 450 - 700, the SST variability is dominated by a cold background state, while in the year 700-900 it is dominated by a warm background state. The 2^{nd} EOF mode, which explains about 10% of the total variance, represents SST variability over the eastern Pacific (EP ENSO type). The center of action of this EOF pattern

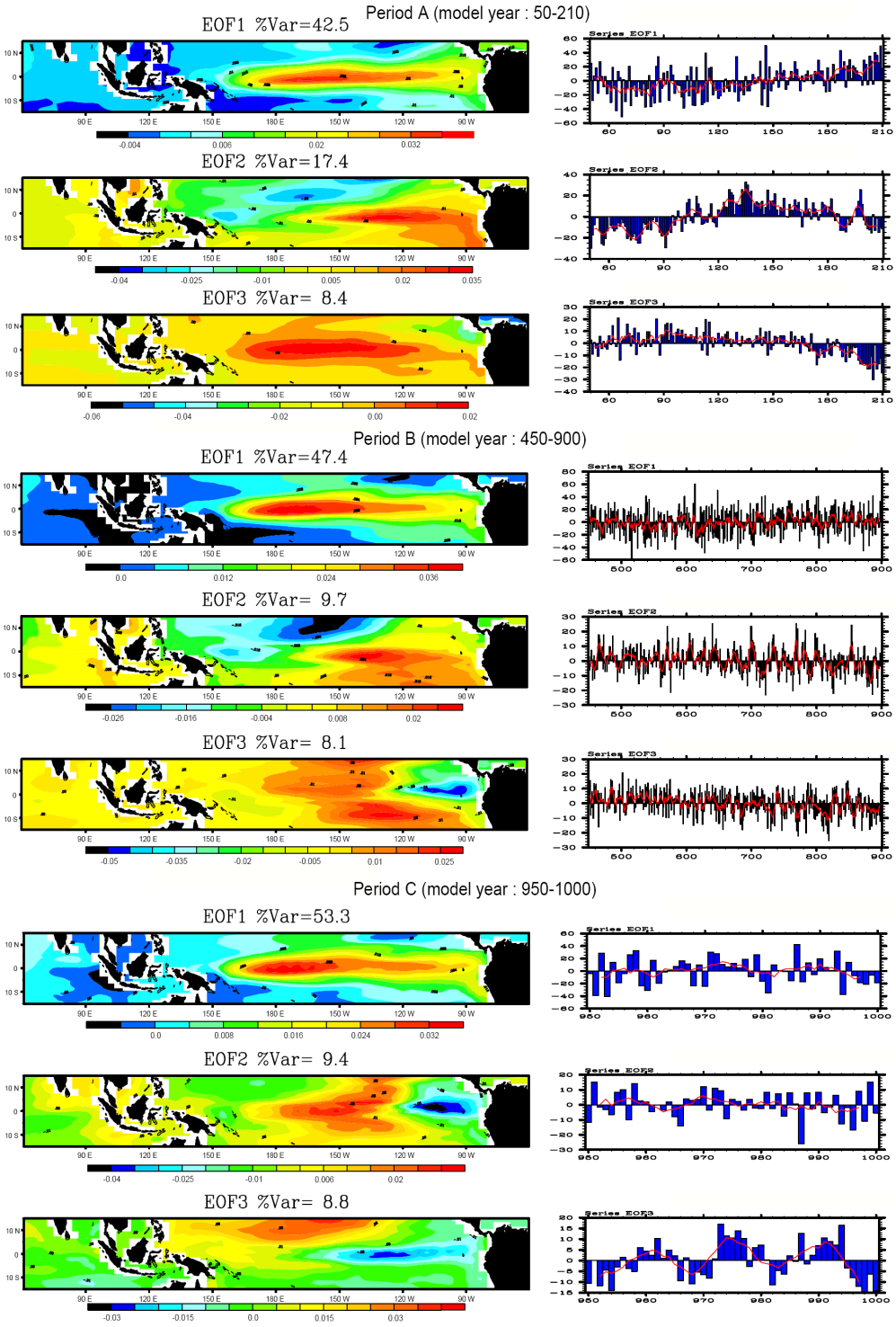

Figure 4.8: Left column : the three leading EOFs of annual mean tropical Indo-Pacific SST for each Period A, B, and C, respectively. The EOFs is computed via a covariance matrix and presented as normalized eigenvector with contour interval 0.01. Right column : the associated PC time series (blue bar) are displayed with two year running average (red line).

is located more in the east-central Pacific rather than eastern Pacific compared to the 2^{nd} EOF mode in Period A. The PC2 time series shows interannual-bidecadal variation. The 3^{rd} EOF exhibits no significant changes relative to the CTRL simulation, and it accounts for less than 10% of the total variance.

In Period C, the leading EOF shows a similar pattern with a central Pacific ENSO mode. The SST variability over the domain explains 53% of the total variance, which is significantly increased in comparison to Period A and B. The temporal behavior of the PC time series exhibits inter-annual to decadal variability. The 2^{nd} and the 3^{rd} EOF account for less than 10% explained variance. Note that the 3^{rd} mode of CTRL simulation became the 2^{nd} mode in Period A and B. As the explained variance of the 2^{nd} and the 3^{rd} EOF is similar and small, thus, this switch does not contain relevant information.

The standard deviation of SST within the domain 20°N-20°S, 140°E-80°W is used to examine furthermore the amplitude and spatial extent of SST and zonal wind stress variance. The standard deviation has been calculated for the entire time series for each period and is displayed in Figure 4.9. It can be seen that during Period A and B, the SST variability is significantly extended along the equatorial Pacific in comparison to the CTRL and Period C, while reduced in the eastern tropical Pacific. Moreover, a second maximum of 2.4°C during Period A reaches almost Papua New Guinea. The center of action of the high standard deviation appeared in the eastern Pacific cold tongue region and in the west central Pacific region which is collocated with the leading EOF in Figure 4.8. In Period B, this structure is reduced and eventually vanish in Period C. However, the variance of the eastern tropical SST increases in Period C. The standard deviation of zonal wind stress shows an enhancement amplitude in the central Pacific and becomes more zonal along the equator line during Period A. This confirms an increase of easterly component displayed in (Figure 4.3a).

To examine the tropical SST due to ENSO characteristics during Period A , the simple statistic of El Niño (warm) and La Niña (cold) events has been analyzed for a century and are presented in Table 4.1. The definition of El Niño (La Niña) year refers to the year when the annual Niño3.4 SST index exceeds (below) the $+1\sigma$ (-1σ). Clearly, during Period A, La Niña (cold ENSO) dominates almost one third along a century, while El Niño only appears with fewer numbers. Period B and C show dominated El Niño (warm ENSO) but with no

Composite	El Niño event (average per-century)	La Niña event (average per-century)
$CTRL$	16	16
$Period-A$	7	37
$Period-B$	20	14
$Period-C$	20	8

Table 4.1: Number of El Niño and La Niña event percentury (100 years analysis) : CTRL vs Period A, B, C. The El Niño (La Niña) refers to the year when the Niño3.4 SST index exceeds (below) the +1.standard deviation, $1.\sigma$ ($-1.\sigma$). The criterion is based on the annual Niño3.4 SST index

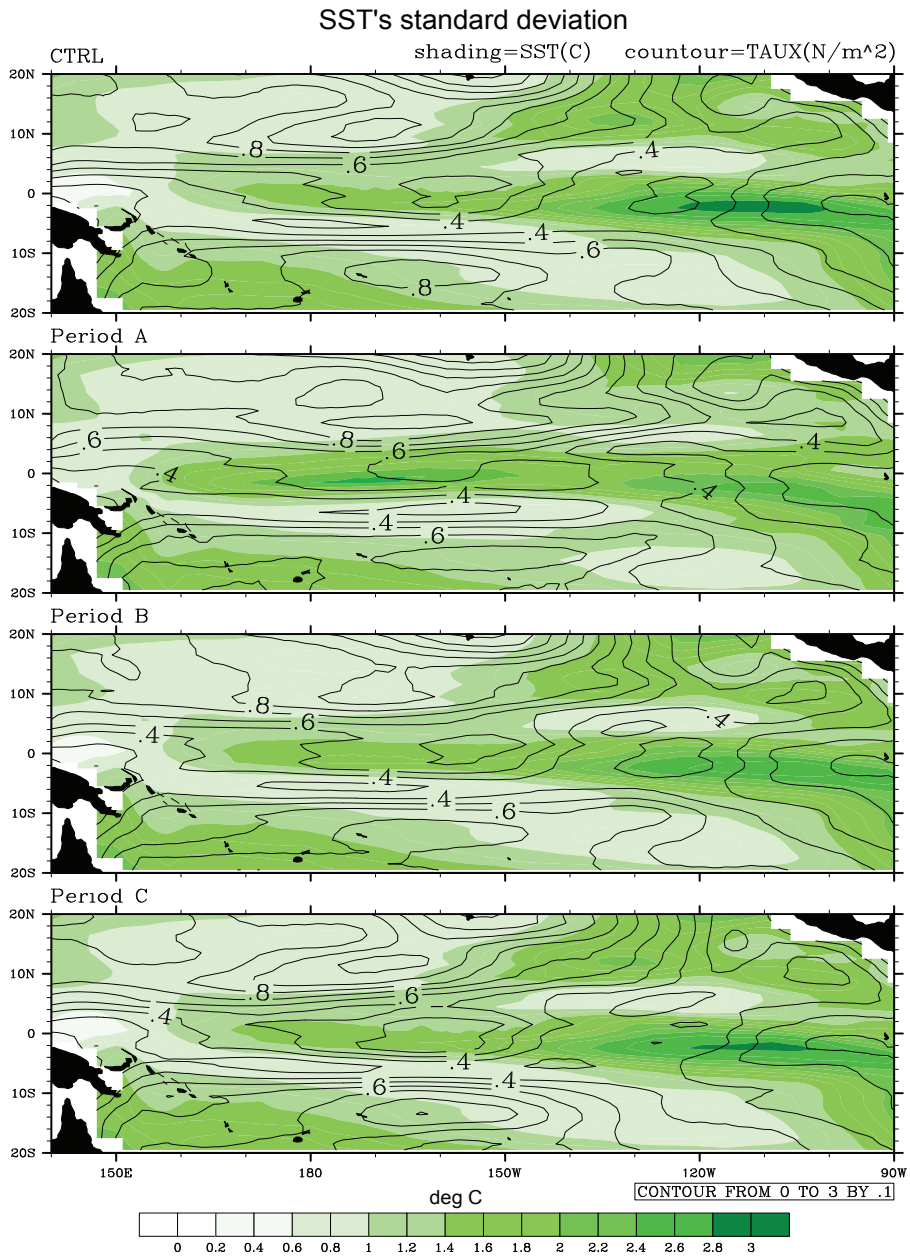

Figure 4.9: Tropical SST ($^{\circ}C$) and zonal wind stress ($N.m^{-2}$) standard deviation for the CTRL simulation and during Period A, B, and C of the FN20 simulation. Standard deviations are computed for SST (shading) and zonal wind stress (contoured) based on the monthly data and describes the population standard deviation as the square root of the average value of $(x-\mu)^2$. Color scales is given at the bottom of the map and is valid for SST standard deviation, and contour interval of 0.1 for wind stress standard deviation.

large quarrel. This analysis suggests that warm and cold ENSO still appears as the dominant variability in the tropical Pacific SST but has a cold or warm background of state.

Since the thermocline depth is an indicator that reflects the amount of heat stored in the upper ocean, the three leading EOFs of vertical profile ocean temperature are estimated for Period A, B, and C. The calculation is based on annual SST data up to 300 meters depth as shown in Figure 4.10. The first EOF which almost explains 50% of the total variance for each period shows a dominant structure of the upper ocean temperature between eastern and western equatorial Pacific. Generally, three periods of the CTRL simulation and the FN20 experiment show a variability of ocean temperature at depth of 150 meters in the west (around date line), in the central Pacific (around 140°W) at 100 meter depth, and variability at the surface ocean up to 50 meter depth in the east (90°W). Period A exhibits a different structure in comparison to the CTRL simulation, Period B and Period C. The PC1 time series shows a dominant 100 year cooling in the ocean surface from the eastern Pacific to the date line region and is followed by a warm domination after year 150. This confirms the shifting in the background climate state of the equatorial Pacific's SST as discussed previously from Figure 4.8. PC2 exhibits the time evolution as in PC1 but more explained variability for the central Pacific, however, it shows a shifting in the model year around 120. The PC3 shows the variability in the west Pacific. From those features on the ocean temperature patterns along longitude and its time series's evolution, thus imply a condition with the steepest thermocline depth in comparison to other periods and the CTRL simulation. This condition is favorable to La Niña (cold) conditions.

The La Niña domination is also confirmed by 20°C the isotherm (not shown) which is used as an indicator for thermocline depth. In the Period A, the seasonal and permanent thermocline depth is deeper (i.e., a deepening in eastern Pacific of 20 meters for the isotherm 20°C during fall and winter, while shallower (steeper slope, shoaling in the eastern Pacific of 15 meters for the isotherm 20°C) during spring and summer relative to Period B, C (which are both similar). The monthly mean vertical temperature consecutive for April (not shown) exhibits a steeper slope relative to other months, which means that April's ocean temperature is significant for the annual cycle of SST variability in eastern and central Pacific. It is also visible that during Period A, the subsurface water is upwelled further west and may be associated with Ekman transport dynamics. Those descriptions above indicate that during Period A the subsurface ocean shows typical La Niña conditions, which are depicted as well in the Niño3.4 SST index and EOF leading pattern. It is suggested that such a thermocline shoaling might lead to an increase in equatorial SST instability.

To determine whether the tropical Pacific SST anomaly in terms of ENSO variability reacts to freshwater hosing in the North Atlantic, the wavelet and power spectra of the monthly Niño3.4 index has been performed for entire FN20 simulation (Figure 4.11).

Changes in frequency, amplitude, and seasonality of ENSO (Niño3.4 region)

The wavelet spectrum of the monthly Niño3.4 index for the FN20 simulation shows a strong power spectrum associated with 28-months (2.3 years) cycle, mainly for the entire analyzed

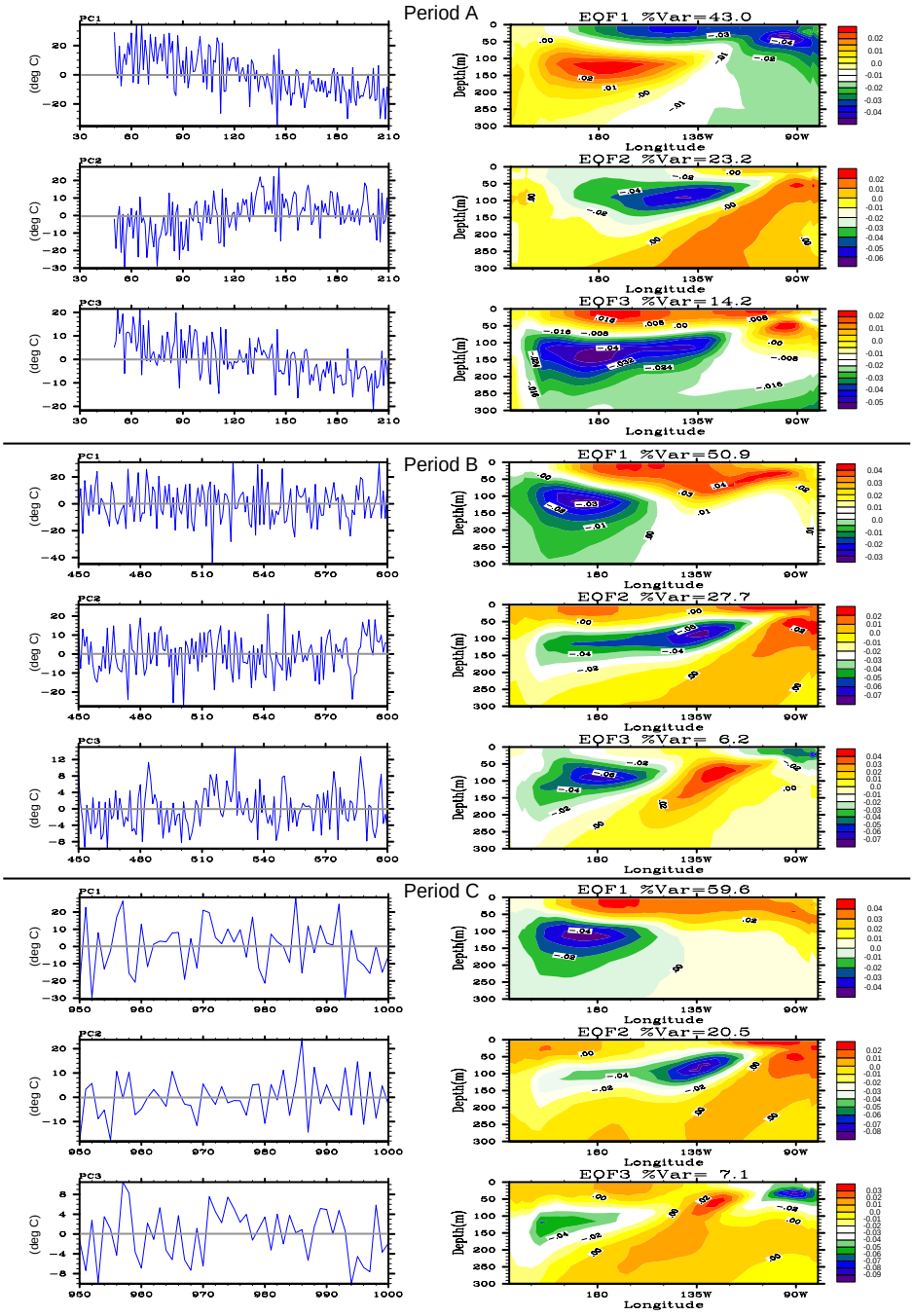

Figure 4.10: The three leading EOFs mode (right) and its PC time series (left) of zonal cross-section of the Equatorial Pacific ocean temperature vertical profile for Period A, B, C, respectively. The Equatorial Pacific is referred to domain area of 5°N-5°S, 120°E-80°W.

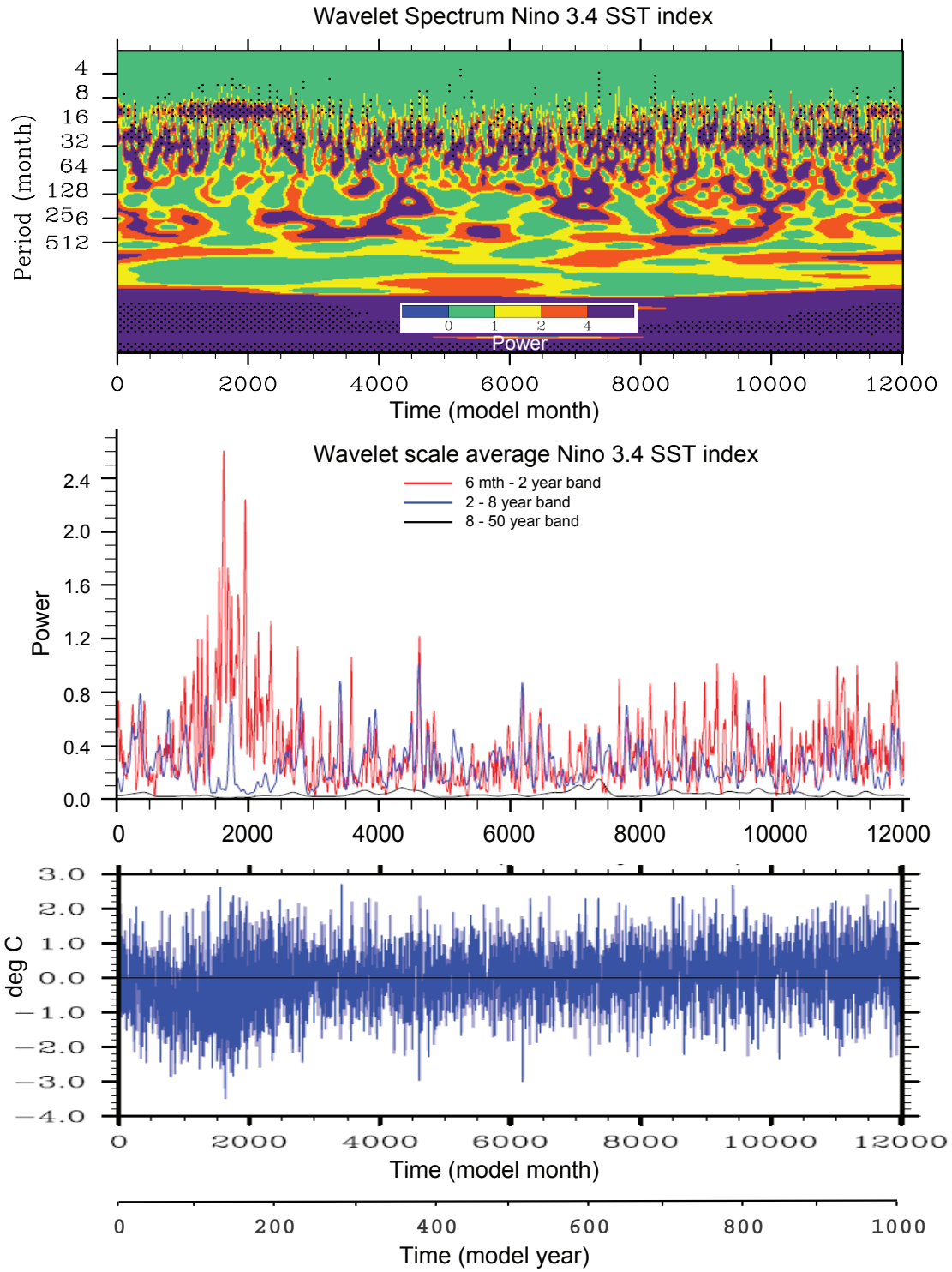

Figure 4.11: Wavelet spectrum, wavelet scale average and time series of Niño-3.4 SST index for entire FN20 simulation.

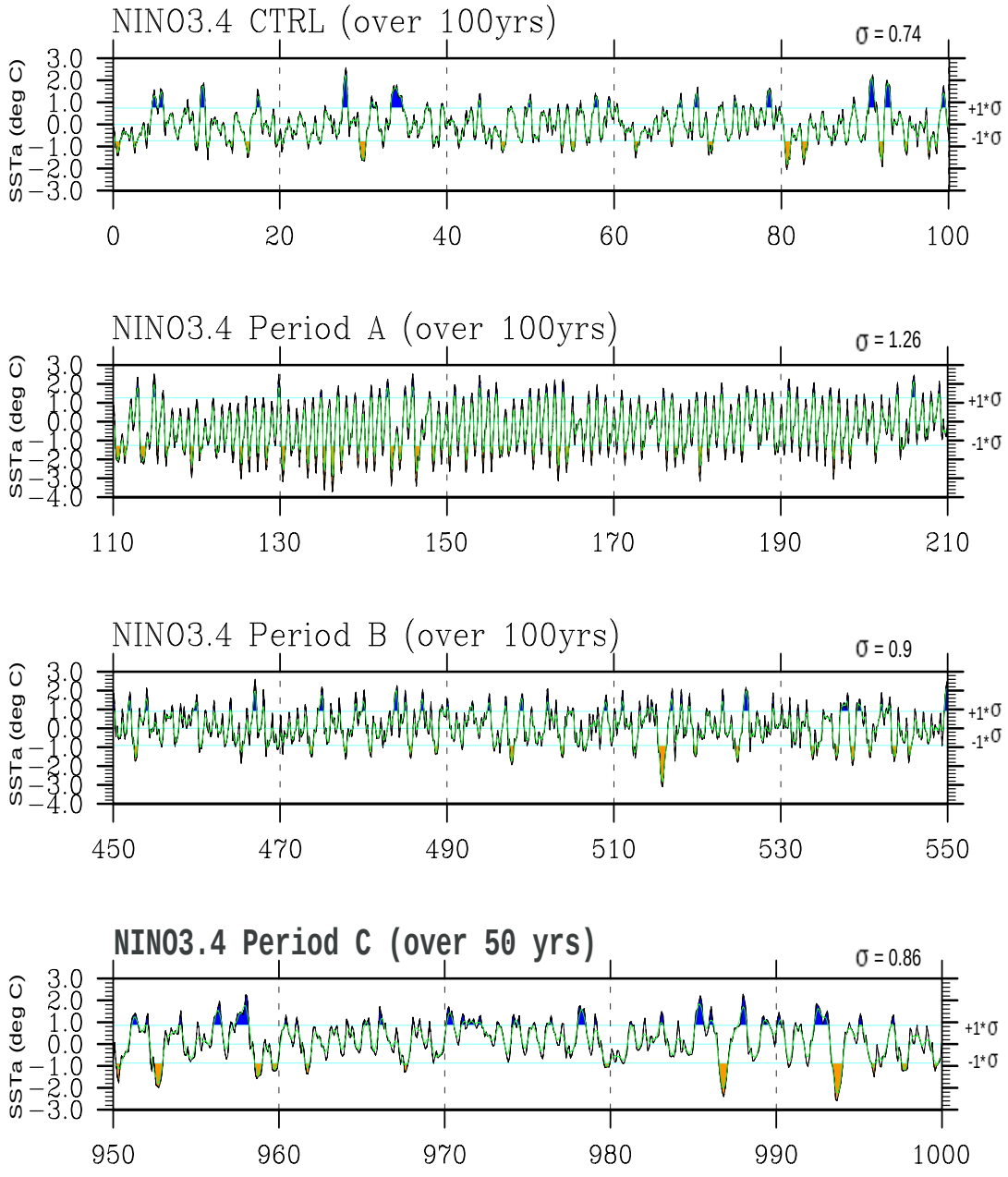

Figure 4.12: Time series of monthly Niño-3.4 SST index for CTRL and FN20 simulation. A 100-years segment is shown representing each period. The standard deviations are given as light blue line and 5-months running means are denoted by green lines. The blue (orange) shading classifies the warm (cold) ENSO years.

simulation. This periodicity is very similar to the ENSO variability in the CTRL simulation. Despite interannual variability, the low frequency variability with periods of 20-years also agree with the CTRL simulation. An interesting deviation is visible during model year 85 - 200 i.e., Period A. In this time window, the inter-annual ENSO cycle significantly shifts to higher frequencies of 12-months periodicity. Note that during Period A, the SST is generally decreased by 2° in the tropical Pacific. The scale-averaged wavelet, which is useful to examine the modulation of the time series over a range of scales (certain range of frequency bands) shows that the interannual (2-8 years band) and decadal variability (8 - 50 years band) are reduced during this period. Reduced interannual to decadal variability suggests that there is probably a changing in the seasonal or annual cycle that suppresses the interannual - decadal variability in the tropical Pacific SST. The average variance for the annual - subannual (<= 1 year) periodicity seems to get stronger and significant in the model year 135 - 168, around 30 years after the maximum perturbation. The particular wavelet for period B and C (not shown) exhibit a normal ENSO variability relative to the CTRL simulation. However multi-decadal variation has increased in variance during year 583 - 625 (Period B).

Looking at 100-year segments of the Niño3.4 SST index for each period and the CTRL simulation (Figure 4.12), high frequency of the Niño3.4 index in Period A is readily visible. This is also in agreement with the standard deviation during Period A, which is accounted for about 1.26°C in comparison to CTRL (σ=0.74°C) and the other periods (Period B σ=0.9°C, Period C σ=0.86°C). Moreover, it is also visible that during Period A, the cold ENSO (La Niña) is more pronounced rather the warm ENSO.

The power spectrum analysis of the Niño3.4 SST index (Figure 4.13) shows the dominant frequency in the FN20 simulation which is in agreement with wavelet analysis presented earlier. The dominant frequency is pointed out by sub-annual (4 and 6 months) and annual (1 year) cycle, which are shown by most three periods. Additionally, the power spectrum of the Niño3.4 SST index also broadly confirms the tendency found for EOF1 time series with increasingly more fractional power at a higher frequency.

The seasonal cycle of monthly mean SST and its standard deviation is shown in Figure 4.14. In general, the model shows an autumn-to-winter warming and spring time cooling interrupted by a fast small warming in the early summer, and then cooling again from summer to autumn. It seems that there are two peaks, one in winter (January) and another one (pseudo peak) in late spring (May). The three periods show different seasonal cycle. Period A exhibits a strong reaction where SST monthly mean drop during March to July with minimum temperature at about 25.2°C in April and maximum at about 28.1°C in December, whereas the annual cycle for other periods is more or less similar with CTRL simulation.

To assess the cause of the high frequency ENSO during Period A, lead and lag correlation analysis between the Equatorial Pacific SST (Nino3.4 SST index) with zonal wind stress anomaly and subsurface ocean temperature (at 50 meter depth) in the same area, as well as the SST anomaly over the North Pacific (20°N-30°S, 170°E-120°W) is performed as in Figure 4.15. Generally, between zonal wind stress anomaly and the North Pacific SST there is significant correlation of up to 0.8 of 2-3 months regard to equatorial SST, while 4 months for subsurface

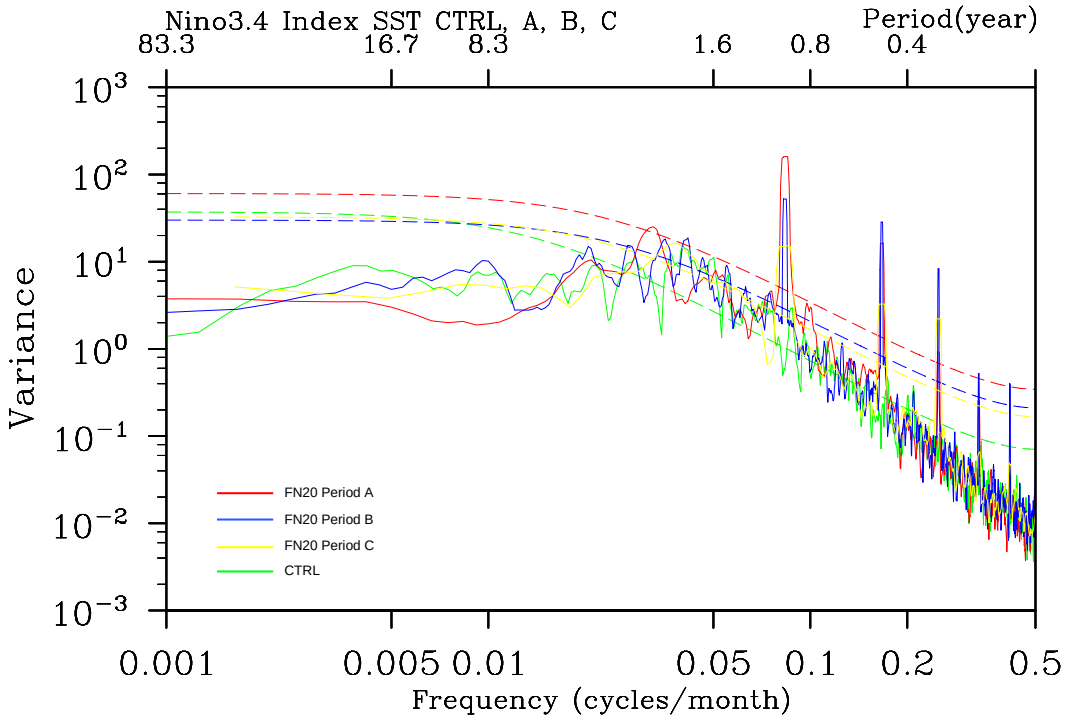

Figure 4.13: Power Spectrum of Niño-3.4 SST index for Observation, CTRL and Period A, B, C, respectively. The dashed line indicate 90% confidence level for each period respect to labeled color.

ocean temperature. The equatorial SST then leads to the wind stress, the North Pacific SST, and the subsurface ocean temperature for 8-10 months (lag). A drop of SST during April might lead to a local noise where the intrusion subsurface ocean water suppresses warm SST farther westward along southeastern off-equatorial Pacific. It seems that springtime cooling is an important contributor to a strengthening of the equatorial annual cycle. It partly relates to the local noise effects, for example, in intrusion of upwelled subsurface ocean water, which matters to the central equatorial Pacific, whereas the seasonal cycle of the mean thermocline depth is important to eastern equatorial Pacific cold tongue variability.

The seasonality changes in the ocean temperature over the equatorial Pacific relate to the enhancement of wind stress anomalies. In particular, strong annual mean northeasterly trade winds during spring time which induced SST cooling is related to the seasonal modulation of the air-sea coupling strength in the central and northeastern Pacific. Equatorial wind stress is associated with the trade winds emanating from subtropical highs in the eastern parts of the ocean basin, and converging on three main areas of convection, the ITCZ in a zonal band north of the equator, which is shown to be shifted southwards during Period A (see section

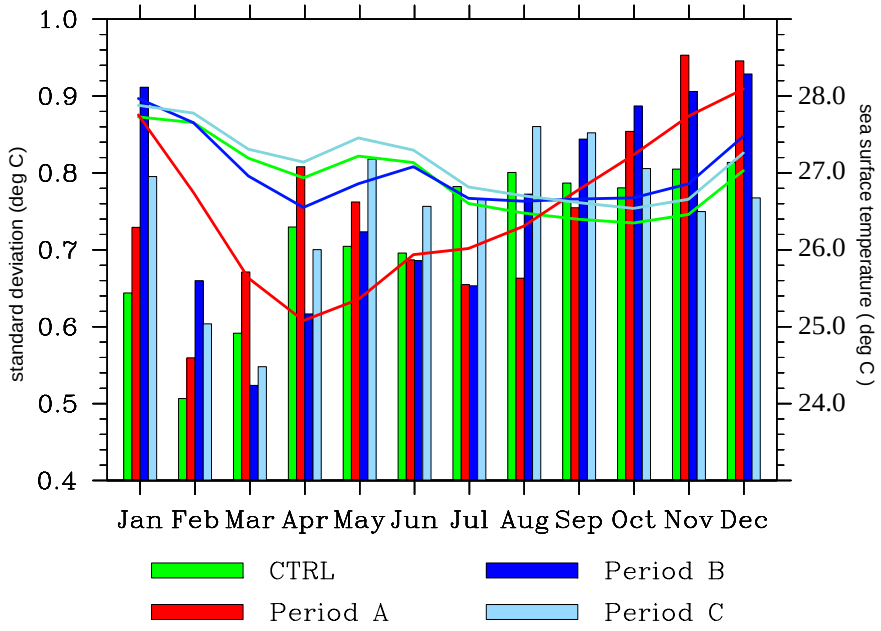

Figure 4.14: Monthly average (line) and monthly of standard deviation (bar) of SST within Niño-3.4 region for CTRL and each period in FN20. The left side Y-axis is for standard deviation in °C, and Y-axis in the right side is valid for SST.

4.2). During this period, there is an additional northeasterly contribution to the total wind stress in the central and eastern Pacific from the low level atmospheric circulation associated with an anticyclone over subtropical gyre retains northeasterly components. Additional contribution comes from intensified northeasterly trades across the Central American Isthmus extended westward into the eastern tropical North Pacific. These cross-Isthmus winds advect anomalously cold and dry air from the Atlantic and decrease SST in the eastern tropical North Pacific by enhancing surface turbulent heat fluxes mixing, and upwelling with a distinct seasonality (*Zhang and Delworth*, 2005; *Okumura et al.*, 2009). Air-sea interactions in the tropical Pacific subsequently, might develop an El Niño or La Niña-like SST anomaly pattern with an equatorial maximum (*Dong and Sutton*, 2002; *Wu et al.*, 2008).

According to *Yeh and Kirtman* [2009], the relatively fast time scale of ENSO in a coupled model might be caused by errors in the spatial structure of the atmospheric model responses to SST (*Kirtman and Schneider*, 1996); that are amplified by a coupled feedback (*Yeh and Kirtman*, 2009). Another effect which might be responsible for the change is that, since simulated ENSO in the CTRL simulation is dominated by biennial time scale variability (although shorter than the observation), it is probably still controlled by thermocline feedback (*van Oldenborgh*, 2005). In this study, the domination of annual and sub-annual variability as well as domination of Central Pacific ENSO type during Period A, the zonal advection feedback (*Neelin and Jin*, 1993; *Guilyardi et al.*, 2009) might be responsible for the changes in

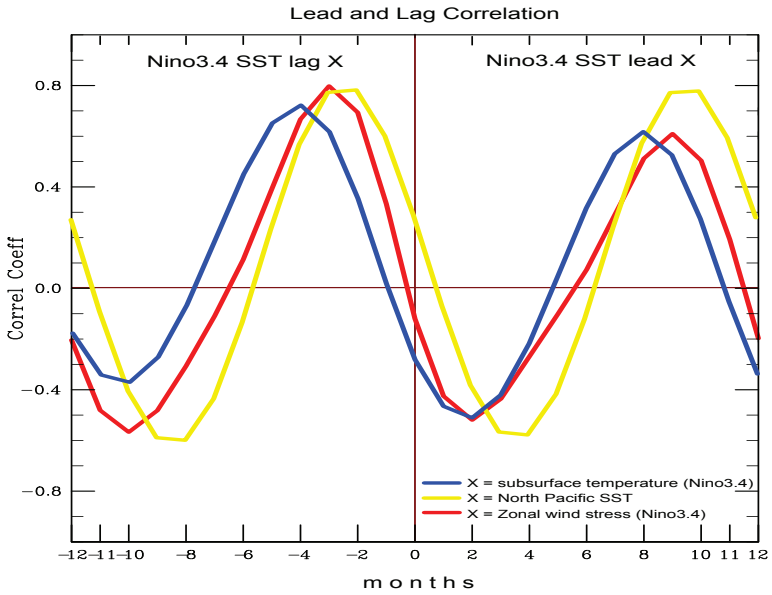

Figure 4.15: Lead and Lag correlation between equatorial Pacific SST (Niño3.4 region) and zonal wind stress (5°N-5°S, 120°E-90°W), North Pacific SST (20°N-30°S, 170°E-120°W), and subsurface ocean temperature (5°N-5°S, 120°E-90°W at 50 meter depth) during Period A.

seasonality due to increased wind stress anomalies along central and northeastern equatorial Pacific. However, this study is not intended to explore those modeling biases.

To assess the influence of ENSO to other regions in the Pacific, a regression map is presented as in Figure 4.16. A positive coefficient means that the SST variability in the Niño-3.4 region and SST or windstress field change in the same direction. A negative coefficient indicates the change in opposite directions. During Period A, the Niño3.4 index is strongly associated with a cyclonicanomaly in the North Pacific subpolar region emanating enhancement ofnortheasterly trade winds in the eastern Pacific and along equatorial Pacific, as well as the southerly component in the southwestern off-equatorial Pacific. In Period B and C, enhancement ofnortheasterly trade winds in the eastern Pacific and along equatorial Pacific is emanated from the subtropical cyclonicanomaly. This suggests that a deepening Aleutian Low during freshwater discharges is important in the ENSO development. Shifting in the climate regime which appeared in the 1^{st} EOF Indo-Pacific's SST pattern after model year 150 might be also related to shifting in the wind stress anomalies' regime. The regression coefficient of the Niño3.4 SST index with split of Period A wind stress field over Pacific basin indicated a different regime anomaly as well as the different response of SST field in the North Pacific and the Southern Ocean (Figure 4.16 bottom panel). In this case, Period A has been divided into two sub-period that is Period Aa (year 50-150) and Period Ab (year 150-210). From those regression maps, this study speculates that the cold regime ENSO which is ap-

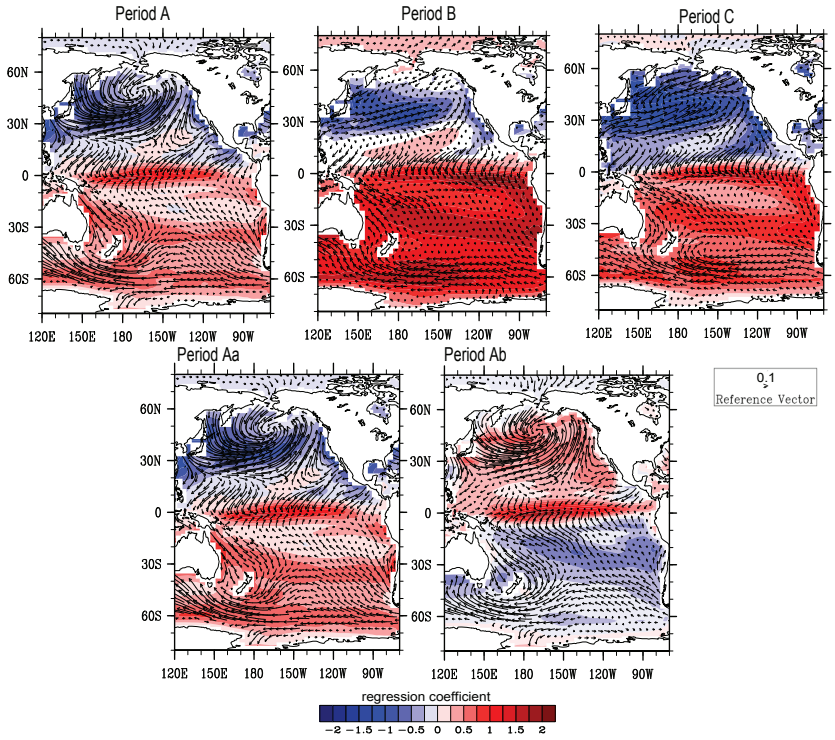

Figure 4.16: Regreesion map of the Niño-3.4 SST index with global SST and wind stress field for Period A, B, and C (upper panel). Period A has been divided into Period Aa (year 50-150) and Period Ab (year 150-210) (bottom panel). Regression coefficient with SST are given as color scales at the bottom of the map and Reference vector indicates 0.1 of regression coefficient.

peared a few decades after maximum perturbation are associated with wind stress anomalies from northeasterly off - trade winds and is associated to decreased SST in the North Pacific. In contrary, the sub-Period Ab, the warm regime ENSO might be driven by southerly component of wind stress anomalies off - trade winds in the west - central Pacific and is associated to increased SST in the North Pacific and decreased SST in the Southern Ocean. However, in both periods the Niño3.4 SST index is strongly related to a cyclonic anomaly in the North Pacific subarctic front region.

The interhemispheric wind stress anomaly and its relationship with Rossby wave mechanisms has been studied in *McGregor et al.* [2007]; *McGregor et al.* [2008]; *McGregor et al.* [2009]. In their papers, the authors investigated the role of Rossby wave to ocean exchanges in extratropical-to-tropical Pacific, in particular, on the variability of ENSO magnitude and its frequency. They revealed in their experiment, when the wind stress perturbation is applied in the Northern Hemisphere with reversed polarity (a cyclonic anomaly in the extratropical North Pacific), the surface wind stress pattern effectively raises the equatorial region pycnocline depth via Rossby and Kelvin wave adjustment. This can lead to stronger La-Niña events and weaker El-Niño events (*Fedorov and Philander*, 2001; *McGregor et al.*, 2009).

The Rossby wave and Kelvin wave mechanisms are explained as the westward-propagating extratropical Rossby waves driven by wind stress changes which reach on the Pacific ocean western land boundary where they create coastally trapped waves that propagate equator ward. Upon reaching the equator, those coastally trapped waves excite low-frequency equatorially trapped Kelvin waves that drive changes in the equatorial thermocline depth (*McGregor et al.*, 2007; *McGregor et al.*, 2008). Nevertheless, since we have seen that the SST variability in the equatorial Pacific is more pronounced in the central Pacific, specially during Period A where the equatorial Pacific seems to be locked in the cold ENSO for almost 90 years, it is speculated that enhancement of wind stress anomalies in the north eastern off-equatorial Pacific may restrain the eastward-propagating equatorial Kelvin waves and accelerate westward-propagation of Rossby waves.

4.3.2 Changes in the North Pacific mean climate

In this section, we examine whether changes in the tropical Pacific SST and ENSO properties are also connected to changes in the North Pacific SST pattern and atmospheric teleconnection. In doing so, we performed a set of EOF analyses for each period to estimate the PDO pattern and the related changes under freshwater discharge in the North Atlantic, while for atmospheric teleconnection we applied rotated EOF to 500 hPa geopotential height. The domain of interest for both analyses is the same as in Chapter 3.

Changes in PDO pattern

Figure 4.17 shows the three leading EOF patterns and its associated time series during Period A. The 1^{st} EOF which explains 35% of the total variance implies a similar structure with the leading mode (PDO mode) in the CTRL simulation with a correlation coefficient of 0.94 (Table 4.2). The associated PC1 time series shows enhanced decadal variability as well as centennial variation. Strong cooling in the North Pacific due to a response to the freshwater discharge has started in year 90 and is clearly visible in PC1. This is in agreement with the North Pacific SST reaction during the maximum perturbation period (in particular subpolar region). However, in comparison to CTRL simulation there is a reduction in explained variance of about 4%.

The 2^{nd} EOF which accounts for ∼15% seems to be similar to the 3^{rd} EOF in CTRL simu-

FN20/		Period A			Period B			Period C	
CTRL	EOF1	EOF2	EOF3	EOF1	EOF2	EOF3	EOF1	EOF2	EOF3
*EOF*1	0.94	0.01	0.15	0.99	–0.02	0.05	0.99	0.07	0.20
*EOF*2	–0.44	0.19	0.57	0.34	0.68	0.52	0.01	–0.89	0.22
*EOF*3	–0.05	–0.91	–0.06	–0.10	0.80	–0.47	–0.00	–0.31	–0.27

Table 4.2: Spatial pattern correlation of the EOF pattern North Pacific SST : CTRL vs Period A, B, C, respectively

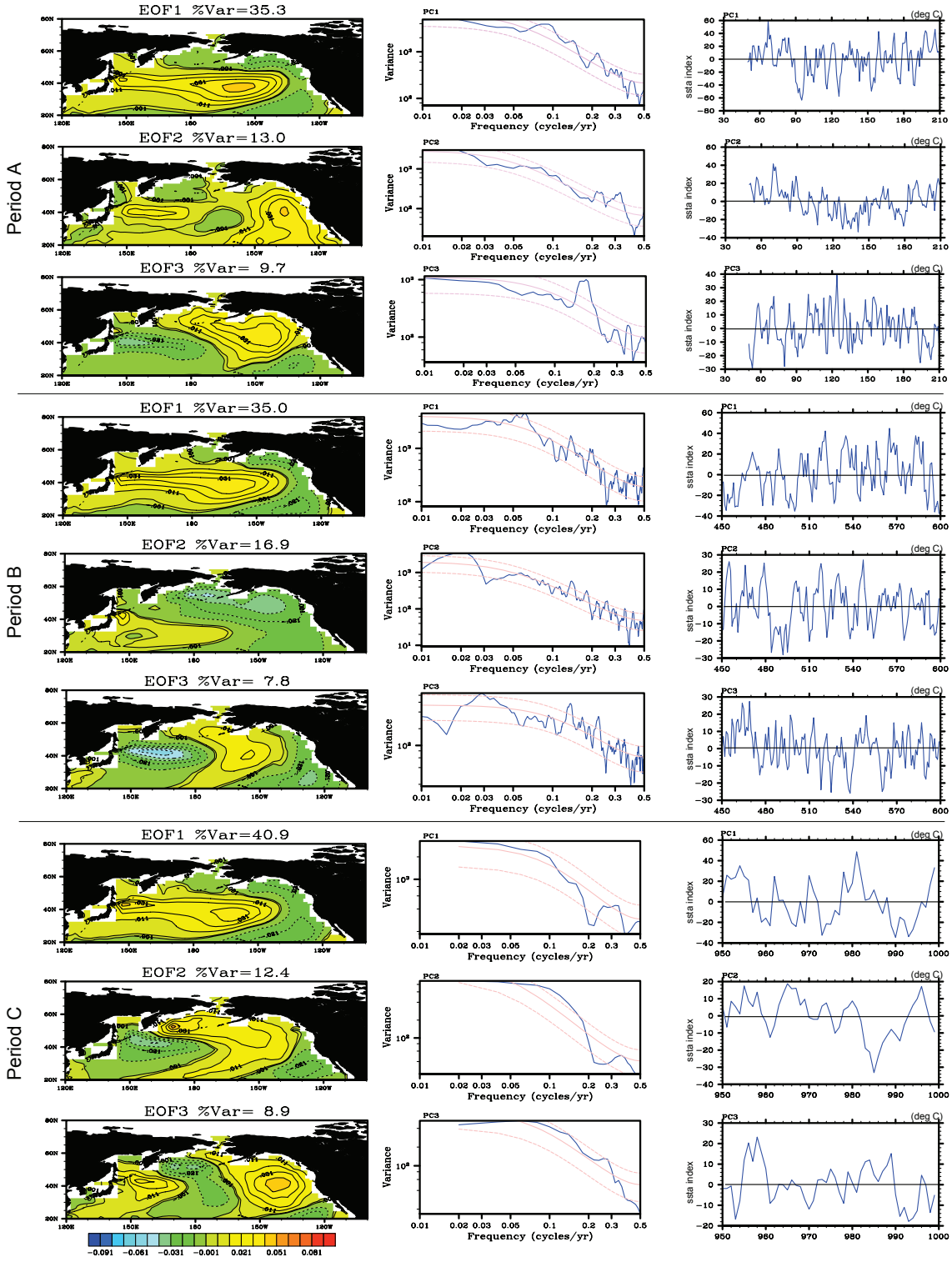

Figure 4.17: From left to right: North Pacific leading EOF pattern, power spectra of PC time series and PC time series of annual SST for Period A, B, and C. The EOF patterns are obtained as in Fig 3.2 with contour interval 0.01.

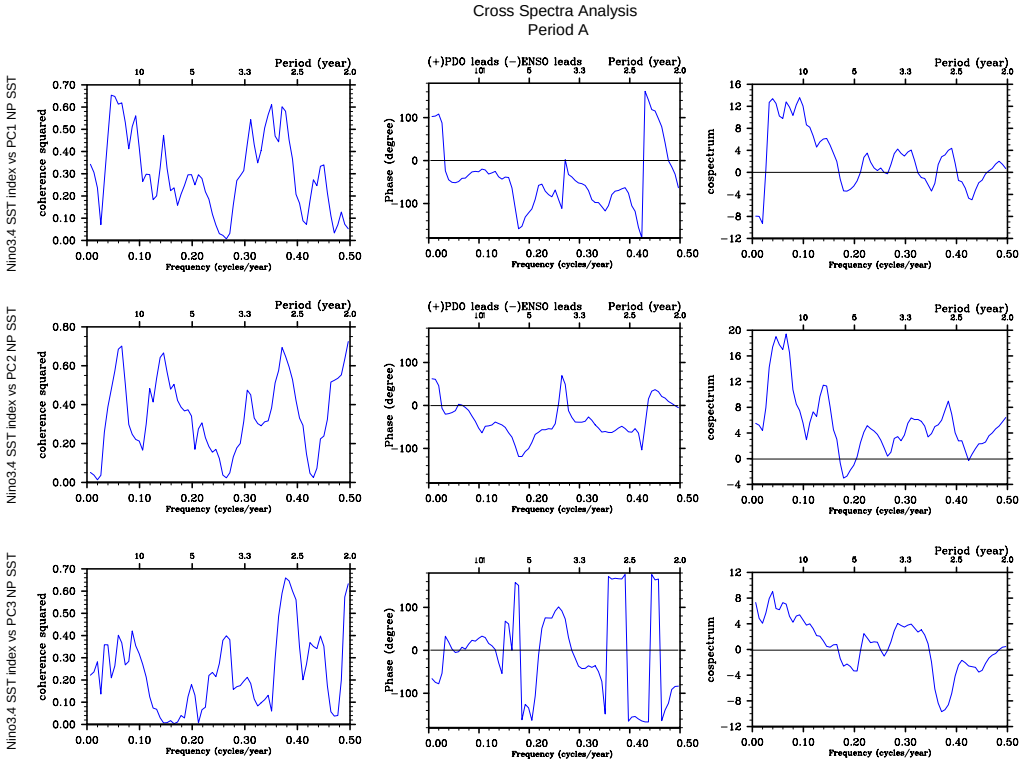

Figure 4.18: Cross spectra analysis of NP SST index vs ENSO indices for Period A. From left to right: coherence squared plot, phase analysis, and co-spectrum analysis. Coherence plot describes the square of the correlation coefficient as a function of frequency. Phase range is from –180° to 180°. Co-spectrum analysis measures the extent of the joint variability. It should be noted that in this case, the Niño3.4 SST index has been averaged to annual mean.

lation with correlation of about –0.91. This EOF pattern is associated to SST variability in the eastern North Pacific and subtropical region. There is an increase of variance by about 4% compared to the CTRL simulation. The temporal behavior of PC2 shows a low frequency (decadal to centennial) modulation. It can also be seen that the cool (warm) phase in the subarctic front region develops along with warm (cool) phase in the subtropical region. This behavior is also similar to the leading mode of Tropical Indo-Pacific SST discussed earlier.

The 3^{rd} EOF which explains about 10% of the total variance with a tripole pattern seems associated with variability in the Gulf of Alaska, west coast of America and west Pacific. This pattern has no significant correlation with the other pattern, however, it has a coefficient of –0.57 with the 2^{nd} EOF in the CTRL simulation. The temporal behavior of PC3 exhibits inter-annual variability modulation.

The EOF analysis for Period B and C exhibit a similar pattern as for CTRL simulation, although in Period B, the 2^{nd} EOF has a pattern correlation to the 3^{rd} EOF in the CTRL simulation, but it is also shared with the 2^{nd} EOF. Since, there are no large changes such as

in Period A, it will not be discussed further on.

As has been hypothesized, the changes of decadal variability in the North Pacific might be remotely driven by the decadal variability of the tropical ocean-atmosphere system through atmospheric teleconnection, just like the inter-annual ENSO variability (*Trenberth*, 1990; *Graham*, 1994). The so called 1976/1977 climate regime shift in the North Pacific, which has been discussed in chapter 3, supports this hypothesis. However, some ideas suggest that a decadal North Pacific mode is independent from the tropical variation (*Nakamura et al.*, 1997), i.e. winter SST variations along the subarctic front zone associated with the PNA pattern are independent of SST variations in the eastern tropical Pacific (*Luo and Yamagata*, 2003).

In this study, it is suggested that the analysis supports the first hypothesis, whereby the changes in the 2^{nd} EOF pattern of North Pacific's SST are due to changes in the tropical SST variability, namely changes in the ENSO frequency and its characteristics. To examine the potential connection between ENSO and North Pacific annual SST changes during Period A, a cross spectral analysis between the Niño3.4 SST index and PC1, PC2 and PC3 time series, respectively, is performed as shown in Figure 4.18. The coherence and phase analysis show that PDO and ENSO are coherent on inter-annual time scales (2-3 years) as well as on decadal time scales (10-20 years). Moreover, the co-spectrum plot shows that the decadal time scale (10-20 years) is dominant in both time series. From the phase analysis, the PC1 shows that North Pacific SST interannual variability of 2 to 2.5 years leads to interannual variability in the equatorial Pacific, while vice versa for the time scale of 2.5 to 6 years as inter-annual ENSO leads the PDO. However, the decadal oscillation is in the same phase among the two time series. This is quite similar to the findings of *Deser and Blackmon* [1995], who identified an inter-annual mode of observed SST variability in the North Pacific that is linked to ENSO, as well as an interdecadal mode that is independent of ENSO (which is different with this coherency analysis). The PC2 time series shows a coherency with the Niño3.4 SST index in time scales of 2 years, 2.8 years, 8 years and 20 years. The decadal oscillation is a more or less still in the same phase among them and dominant in both time series. However, interannual variability is shown by equatorial Pacific leads the North Pacific SST with phase of 90°. The PC3 time series shows a coherency with the Niño3.4 SST index in time scales of 2 years and 2.8 and dominant in this time scale. The decadal oscillation is a more or less still in the same phase. Regarding to the changes in the 2^{nd} leading North Pacific SST pattern during Period A, ENSO might be responsible in contributing decadal SST variability in the North Pacific.

Changes in Atmospheric teleconnection

The rotated EOF (REOF) of 100-year model simulations during Period A is depicted in Figure 4.19. The spatial pattern correlation between the CTRL simulation and Period A, B, and C of the FN20 simulation is also shown in Table 4.3. The 1^{st} EOF shows an AO-like pattern which is slightly different to the leading REOF of CTRL simulation. The changes in the 1^{st} EOF is shown also from the correlated spatial pattern between CTRL simulation and during Period A and B. The AO pattern in Period A shows a strong polar low (high) surrounded by a high (low) pressure belt, and a deep dipole pattern which represents two opposing atmospheric pressure patterns in northern middle and high latitudes. During this period, the 1^{st}

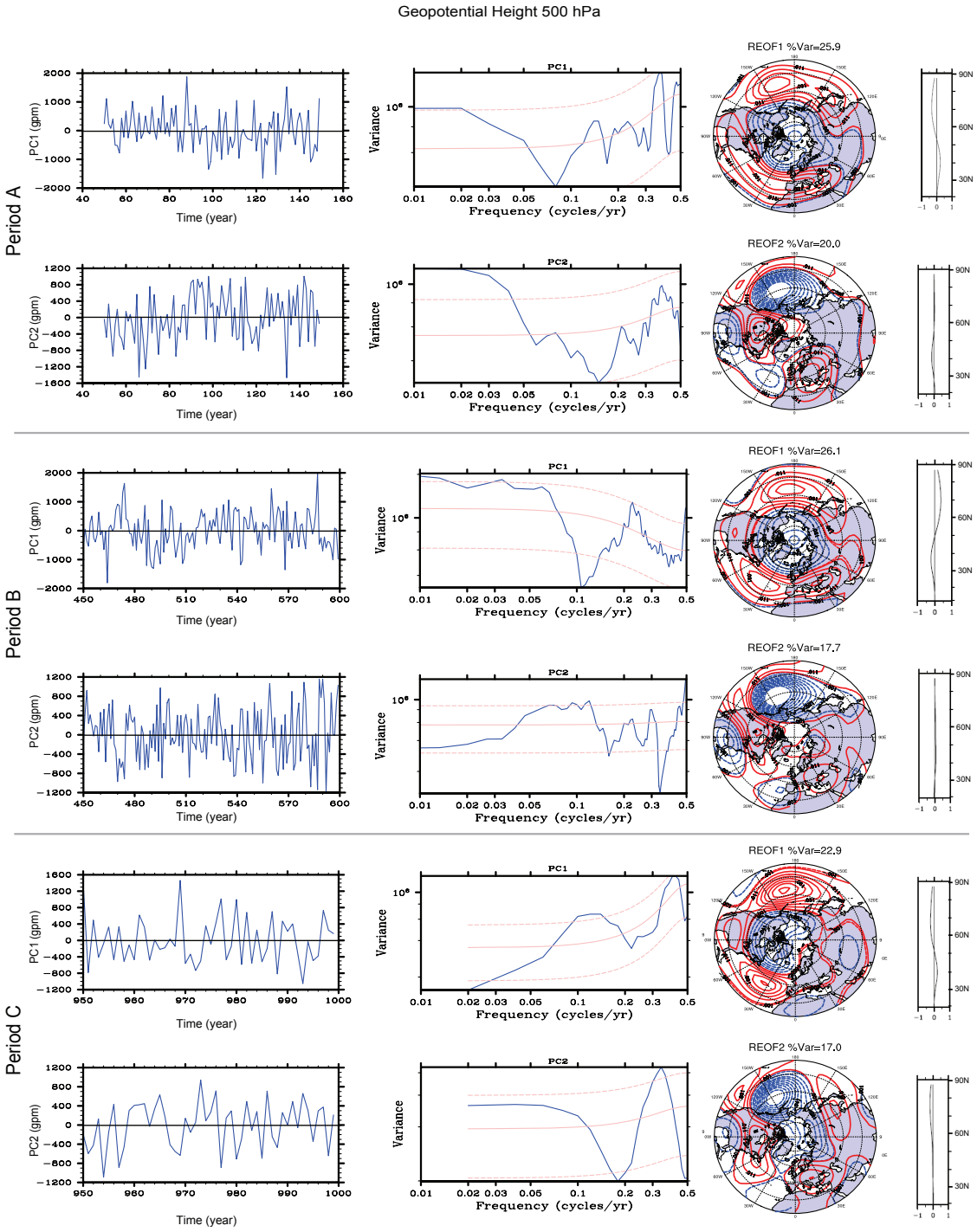

Figure 4.19: From left to right: PC time series, power spectral analysis, REOF pattern and zonal average of Northern Hemisphere winter 500 hPa geopotential height leading REOF for Period A, B, and C. The description is the same as in Fig 3.14.

FN20/ CTRL	Period A EOF1	EOF2	EOF3	Period B EOF1	EOF2	EOF3	Period C EOF1	EOF2	EOF3
*EOF*1	0.75	–0.18	–0.85	–0.73	0.20	0.83	0.85	–0.46	–0.54
*EOF*2	–0.29	0.93	0.20	0.14	–0.98	–0.08	–0.03	0.78	–0.34
*EOF*3	0.43	–0.16	0.06	0.59	–0.39	-0.42	–0.60	0.13	0.25

Table 4.3: Spatial pattern correlation of the Northern Hemisphere geopotential field REOF patterns between the CTRL simulation and Period A, B, and C of the FN20 simulation.

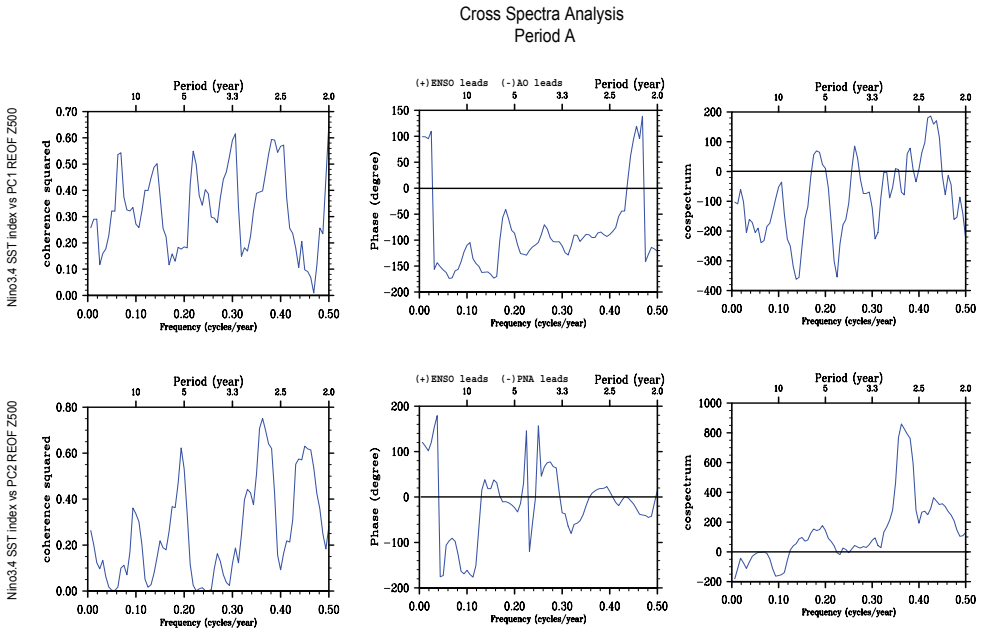

Figure 4.20: As in Figure 4.18 but for the the Niño3.4 SST index and PC1 and PC2 time series of NH Z500 during period A.

REOF time series exhibits a domination of weak oscillations of "positive phase" index from year 60 to 85 and followed by a strong oscillation index from year 85 - 160 which shows more to "negative phase". The features of the AO in its strong index phase is shown as the polarity in which the subpolar westerly winds are anomalously strong. This polarity is also shown by the zonal average of the AO pattern which is enhanced north of 55°N. This means that the atmospheric circulation tends to be more zonal than its average i.e., because of strengthening westerlies. In a strong oscillation index, a low pressure sits over the pole, surrounded by a belt of enhanced westerly winds at 55°N, which is accompanied by a slackening of the westerly around 35°N (*Wallace and Gutzler*, 1981).

Compared to the CTRL simulation, there is a relative increase in the explained variance to about 4% of geopotential height variability over the Arctic ocean, North Pacific and North Atlantic geopotential field with a periodicity of about 2.5 years (inter-annual) and 50 years (multidecadal), as well as a more zonal structure over the Eurasian continent. The 2^{nd} REOF with 20% explained variance shows the PNA pattern. The 3^{rd} REOF which explains 10% of the variability is similar to an NAO-like pattern with dominant periods of 2-4 years (not shown).

The two leading REOF patterns in Period B exhibit a similar feature as in Period A with an AO-like dominant pattern and PNA pattern as the second mode. However, the explained variance for the PNA pattern is reduced to 18%. A change in the leading mode is found in Period C, where the 1^{st} EOF exhibits an NAO-like mode which explains 23% of the total variance similar to the CTRL simulation. The PNA pattern remains the same with the explained variance of up to about 17%.

To examine the potential connection between ENSO and Northern Hemisphere winter atmospheric mode changes during freshwater perturbation, a cross spectral analysis between two indices (the Niño3.4 SST index and the PC1 and PC2) is also performed as shown in Figure 4.20. From coherence and phase analysis between the Niño3.4 SST index and the PC1, we find that the AO and ENSO have a relationship, as they show coherence on the inter-annual cycle (2.5-3.5 years) as well as on decadal variability ($\geq$ 10 years cycle). This is also the dominant joint variability as illustrated by the co-spectrum plot. The phase analysis between the Niño3.4 SST index and PC1 shows that ENSO leads the AO on the time scale of 2 - 2.5 years, and vice versa for longer time scale. The phase analysis between the Niño3.4 SST index and PC2 shows ENSO and AO is in the same phase on the time scale of 2 - 3.5 years. However, the decadal (10 years) oscillation is in anti-phase (AO/PNA lead ENSO) for both time series, and vice versa for the lower frequency (more than 20 years). It seems that the tropical SST variability contributes forcing the Northern Hemisphere atmospheric variability on interannual variability of 2-2.5 years for AO-like pattern and 4-5 years for PNA-like pattern. The opposite is true for the decadal variability (AO/PNA leads ENSO). This analysis is similar to the result of *Jia et al.* [2009] which shows that ENSO is responsible in the generation of the forced AO-like pattern (*Jia et al.*, 2009). The decadal variability of tropical SST anomalies forced by the AO-like variability may also play a role in the subsequent evolution of the conventional ENSO phenomena which is described in *Wu* [2010].

Chapter 5

Discussion and Conclusion

The model evaluation presented in Chapter 3, and the result from the freshwater experiments discussed in Chapter 4 focus on the teleconnection through oceanic and atmospheric mechanisms due to North Pacific cooling during the freshwater discharge experiment. A simplified schematic diagram illustrates the different oceanic and atmospheric processes (Figure 5.1). The schematic diagram tries to answer the questions raised in Chapter 1 and to describe the proposed possible mechanisms which play a role, especially during Period A. The importance of freshening and cooling of North Pacific SST and the importance of both seasonal tropical and extratropical conditions for a possible interrelationship between, and influence of the changes in ENSO behavior and North Pacific decadal variability will be further discussed. Tropical SST changes seem to initiate an atmospheric bridge between winter and early summer, and the resulting extratropical SST anomalies seem to be of importance as they persist enough to feed back to the atmosphere when the climatological background state is favorable. Therefore, it is important to consider together, in a global perspective, tropical and extratropical signals as they are not independent and contribute, by a cooperative and constructive interaction, to the variability of the ENSO and decadal variability of the North Pacific. It would be interesting, in particular, to test the ocean temperature - atmosphere link presented in this study from the complex coupled model integrations.

a. What is the origin of North Pacific cooling during AMOC slow downs?

Oceanic connection through the Bering Strait

The North Pacific is connected to the Arctic Ocean and ultimately, to the North Atlantic through the Bering Strait, a narrow and shallow passage between Alaska and Siberia (*Okumura et al.*, 2009). The Bering Strait is the only ocean gateway between the Pacific and Arctic, with a width of ∼85 km and a depth of ∼55 m. In the present-day climate, the Bering Strait throughflow is hydraulically controlled and directed northward (but can flow southward for a week or more) driven (supposedly) by anomalous pressure gradients between the Pacific and the Arctic oceans, opposed by the local winds, transporting warmer and fresher water from the North Pacific into the Arctic Ocean (*Woodgate and Weingartner*, 2006).

In the FN20 water-hosing experiment, a reduced surface salinity indicates the freshening of

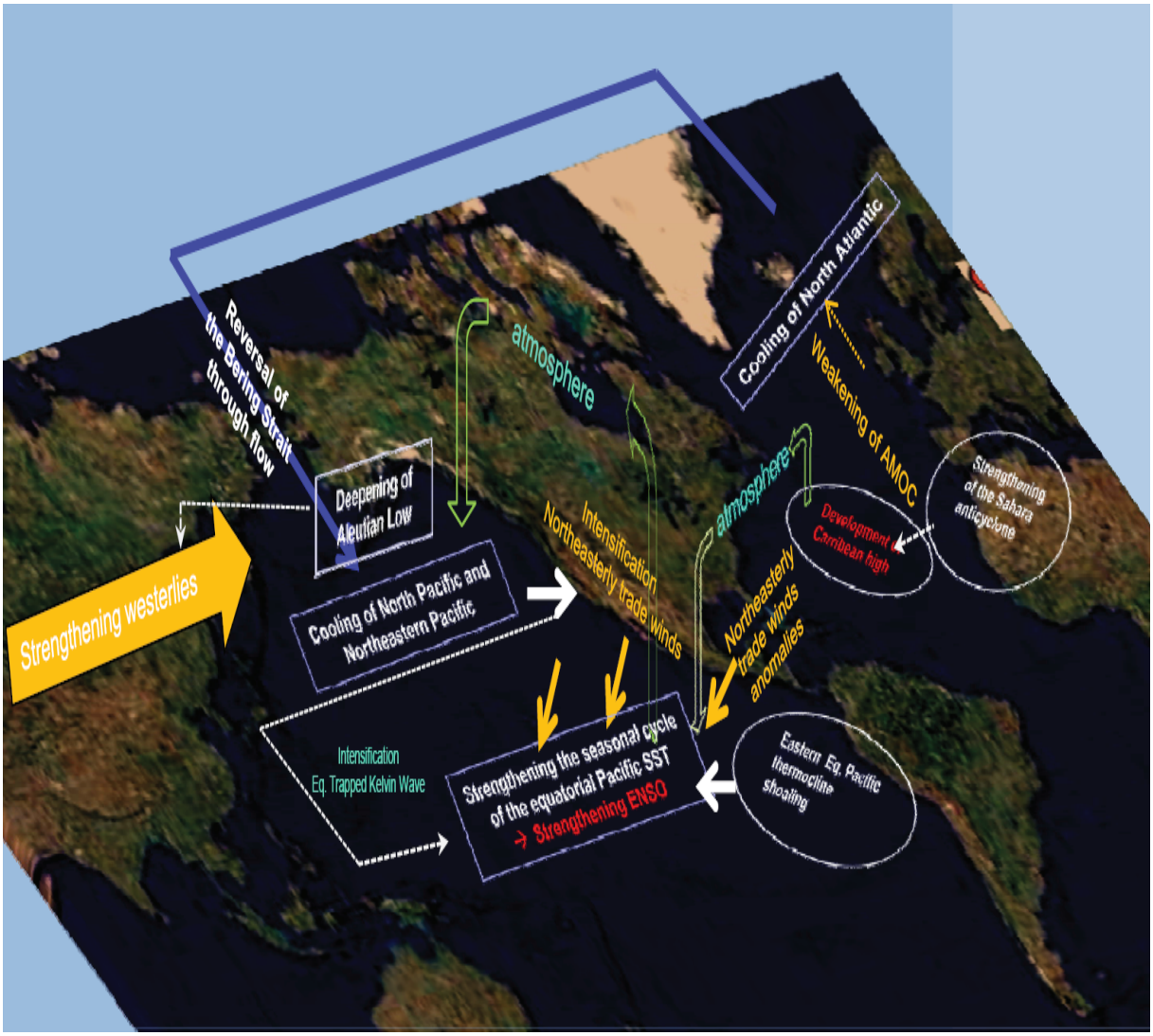

Figure 5.1: Schematic diagram of the summarized possible mechanisms of oceanic and atmospheric dynamic processes during AMOC slow downs

oceanic surface water. As in the water hosing experiment, a part of the freshwater applied in the North Atlantic can flows into the Arctic Ocean, raising the sea level there and weakening the throughflow. In our simulations, the Bering Strait throughflow is eventually reversed after a few decades from the maximum perturbation. The reversal of the Bering Strait throughflow significantly impacts the heat and salinity balance in the North Pacific. From the difference map between CTRL simulation and SST as well as SSS field for each period, negative SSS and SST anomalies extend from the eastern subarctic North Pacific to the west coast of the United States, and further into the subtropical basin, which indicates the impact of the throughflow

changes. The evolution of SSS and SST anomalies shows that the extended cooling and freshening of surface ocean is pronounced along the east coast of the Kamchatka Peninsula. During the second decade after maximum perturbation, the anomalies extend southeastward into the interior of the basin, following the mean ocean current. Upon reaching the west coast of the United States near the end of the second decade, the anomalies spread to the north and south along the coast with the southern branch penetrating into the subtropical basin. Thus, advection of temperature and salinity anomalies by the mean ocean current play an important role for the rapid North Pacific cooling by oceanic processes. While the advection of cold water directly affects the mixed layer heat balance, the advection of freshwater indirectly contributes to the cooling by increasing the upper ocean stratification and by reducing oceanic convection. Note that the FN20 experiment is forced by an uncompensated virtual salt (real water) flux and consequently, the response of the Arctic sea level and the Bering Strait throughflow does not depend on the form of the forcing. This sensitivity of North Pacific SSTs to changes in the Bering Strait throughflow and role of the Bering Strait in abrupt climate change has been discussed in some more detail in *Okumura et al.* [2009] and*Hu et al.* [2007].

The extratropical and subtropical cooling caused by oceanic advection intensifies the trade winds which in turn cools the tropical North Pacific via wind-evaporation-SST (WES) feedback (*Wu et al.*, 2008). Off the Pacific coast of the Central American Isthmus, negative SST anomalies are also found during Period A, indicating that the North Atlantic cooling and resulting cross-Isthmus wind anomalies play a major role in cooling this region (*Xie et al.*, 2008; *Okumura et al.*, 2009).

On the other hand, the intensification of the wind stress anomalies as a consequence of enhanced westerlies over the North Pacific can also lead to the SST variability over the tropical region. The results of this study suggest that the wind stress anomaly, mainly from northeasterly off-equatorial trade winds is associated with Rossby wave mechanisms proposed in *McGregor et al.* [2007]. The role of Rossby waves in influencing extratropical-to-tropical Pacific ocean exchanges depends on the variability of ENSO magnitude and its frequency (*McGregor et al.*, 2008; *McGregor et al.*, 2009). It is suggested here that the Northern Hemisphere wind stress raises the equatorial region pycnocline depth via Rossby and Kelvin wave adjustment. The westward-propagating extratropical Rossby waves driven by wind stress changes impinge on the Pacific ocean western land boundary. Further on, they create coastally trapped Kelvin waves that propagate equatorward. Upon reaching the equator, those coastally trapped waves excite low-frequency equatorially trapped Kelvin waves that drive changes in the equatorial thermocline depth (*McGregor et al.*, 2007; *McGregor et al.*, 2008). This can lead to stronger La Niña events and weaker El Niño events (*Fedorov and Philander*, 2001; *McGregor et al.*, 2009).

Inter-basin and Tropical-extratropical atmospheric teleconnection

The deepening of the wintertime Aleutian Low during Period A has been discussed in the previous chapter. The question as to what enhances the wintertime Aleutian Low when the AMOC slows down needs to be addressed. The SST anomalies in the North Pacific may affect

the atmospheric circulation through several pathways, including the excitation of preferred circulation variability patterns and the propagation of Rossby waves remotely forced by tropical precipitation changes. We investigate these pathways by analyzing the regression map of the Niño3.4 SST index and the geopotential field pattern of the Northern Hemisphere (not shown). The Aleutian Low deepens by 5 hPa during wintertime. The Northern hemispheric pattern of 500 hPa geopotential height during Period A closely resemble the Arctic Ocean pattern which is described in *Wallace and Gutzler* [1981] and *Thompson and Wallace* [1998]. This can be interpreted as the atmospheric signature of modulation in the strength of the polar vortex aloft. This supports the idea that the Atlantic and tropical Pacific together force a large part of the atmospheric circulation changes in the Northern Hemisphere (*Okumura et al.*, 2009).

Which part of the remote forcing is important for the Aleutian Low response? From the analysis in Chapter 4, we find that the North Pacific wind anomalies coincide with the deepening Aleutian Low. The regression map between tropical SST anomaly (represented by Nino 3.4 region) and the SLP field (not shown) confirms a relatively strong response of deepening Aleutian Low. The relative importance of the tropical Pacific SST anomalies to the Aleutian Low response undergoes substantial changes from late fall through early spring. Forced by tropical Pacific SST anomalies, the simulated monthly cycle of the Aleutian Low response (analysis not shown) to these SST anomalies contributes to a deepening of Aleutian Low. The tropical Pacific SSTs become more important in mid-winter (December-January). This seasonal sensitivity of the Aleutian Low to tropical Pacific SSTs is in agreement with studies of ENSO teleconnections (*Alexander et al.*, 2002).

In association with this subtropical cooling, the Pacific ITCZ shifts southward, contributing to the tropical Pacific precipitation changes during Period A. It has been reported that a southward shift of the Atlantic ITCZ is the most robust remote response to an AMOC weakening in both paleoclimate records and coupled GCMs (*Chiang et al.*, 2003; *Chiang*, 2009; *Stouffer et al.*, 2006; *Okumura et al.*, 2009). Anomalous trade wind intensity peaks in Period A and tends to build or reinforce the so-called oceanic interhemispheric SST gradient in the deep Tropics. The atmospheric response to the oceanic cross-equatorial gradient is maximum for late spring/summer months (May-September) and is characterized by a meridional displacement of the ITCZ towards the warmer hemisphere. Large-scale shifts in tropical atmospheric convection can dramatically affect the global circulation as revealed by atmospheric teleconnection studies related to ENSO (*Trenberth and Guillemot*, 1998). When the Pacific ITCZ is shifted southward, the Atlantic ITCZ is displaced to the south as well. The tropical Pacific SST anomalies are, in turn, forced by atmospheric teleconnections from the tropical Atlantic mainly shown by enhancement off the northeasterly trade wind across Central American Isthmus, implying an important role of the tropical Atlantic in association to the AMOC and North Pacific climate. Previous studies of inter-annual and interdecadal Pacific variability show that a southward shift of the Pacific ITCZ and weakening of the Walker circulation act to strengthen the Aleutian Low by forcing barotropic Rossby waves and triggering the Pacific/North American pattern (*Deser et al.*, 2006; *Okumura et al.*, 2009), consistent with results of this study. However, *Okumura et al.* [2009] stated that the relative importance of each remote forcing mechanism may be model-dependent in their study due to differences in the model's mean climate.

As it has been mentioned in the previous chapter, besides the deepening Aleutian Low, anomalous high pressure that develops during Period A in the Caribbean Sea is expected to be responsible for enhancement of the easterly trade winds in the eastern tropical Pacific. The tropical North Atlantic cooling induces anomalous high pressure around the Caribbean Sea that extends westward into the eastern tropical North Pacific, thereby intensifying north-easterly trade winds across the Central American Isthmus. This result is consistent with a previous study (*Timmermann et al.*, 2007). The presence of the Caribbean High during Period A is caused by SST cooling in the Caribbean Sea during freshwater discharge. In the present climate, the Caribbean Sea constitutes the so called Atlantic Warm Pool (AWP) with waters warmer than 28.5°C. The AWP is located to its northeastern side of the North Atlantic Subtropical High that produces the easterly trade winds in the tropics. The trade winds carry moisture from the tropical North Atlantic into the Caribbean Sea where the flow intensifies forming the Caribbean Low-Level Jet (*Wang and Lee*, 2007; *Wang et al.*, 2008). The absence of the Caribbean warm pool during this period and the mean precipitation which is less than 2 mm per day (Figure 4.7) in the western tropical North Atlantic (where a strong cooling occurs in response to an AMOC weakening) suggest that the mean SST is too low to sustain deep atmospheric convection. Additionally, in the tropical North Atlantic, the excitation of atmospheric Rossby waves is quite sensitive to the background SST and precipitation distributions, which are underestimated in most coupled GCMs (*Okumura et al.*, 2009). The atmospheric Rossby waves propagate along the South Asian jet and then propagate into the North Pacific (*Okumura et al.*, 2009). In addition to Rossby wave propagation, the structure of intrinsic circulation variability may also play an important role in shaping the anomaly pattern over the North Pacific. The regression map between SLP and the PC1 and PC2 of geopotential field rotated EOF (not shown) imply that the Aleutian Low response resembles the AO pattern and Pacific/North American pattern, which are shown as the 3^{rd} and the 2^{nd} leading mode in the CTRL simulation.

b. What is the impact of the North Pacific cooling to the ocean-atmosphere coupled modes and which processes and possible mechanisms are involved and play a role?

The main result of this study is changes on the the equatorial (ENSO) and North Pacific SST mode, as well as the enhanced AO-like pattern that has been mentioned in chapter 4. A shifted ENSO into high frequency has been discussed where the dominant frequency in the FN20 simulation is pointed out by sub-annual (4 and 6 months) and annual (1 year) cycle. The changes in frequency are shown by most three periods, with larger variance in Period A. It is apparently that the freshwater discharge in the North Atlantic yields instability in the seasonal cycle of the tropical Pacific SST as have been shown on the amplitude of spring-time SST. This means that the SST has fluctuated rather strongly and in more frequent cycles. The changes in the seasonality eventually enhance the frequency of ENSO. This study also found that during maximum perturbation, the SST variability in the equator Pacific is more pronounced in the central Pacific. This result suggests that enhancement of wind stress anomalies in the north eastern off-equatorial Pacific may restrain the eastward-propagating equatorial Kelvin waves and accelerate the westward-propagation of Rossby waves. The changes in ENSO characteristics represent changes in the tropical Pacific SST which is, in

turn, followed by changes on the 2^{nd} leading mode of SST in the North Pacific sector (the 3^{rd} mode in the CTRL simulation). In addition to these changes, the AO-like mode dominates the Northern Hemisphere atmospheric variability. This thesis proposes that the "atmospheric bridge" mechanism is responsible for those changes which are remotely driven by the variability changes in the tropical SST during Period A.

The far-below normal conditions during Period A which is shown by the dominated SST pattern over the tropical Pacific and the large deviation of monthly SSTs during spring time relative to the CTRL simulation in the Niño3.4 region are accompanied by anomalously warm waters in the west to central North Pacific, cold waters off the western North American coast (not shown) which can be defined as a "negative phase" of PDO. Indeed, the cold ENSO phase (La Niña) is more pronounced during the cool (negative) PDO phases (*Schoennagel et al.*, 2005). This result is consistent with the observed relationship between ENSO events and the SST field in the North Pacific which has been proven e.g., by the pronounced shift in the conditions of the North Pacific during 1976/1977 (*Lau and Nath*, 1996; *Lau and Nath*, 2001). The connection between SST variability in tropical and mid latitude was investigated by *Alexander* [1992] who used various models to examine the extratropical ocean driven by atmospheric anomalies related to ENSO. Moreover, global analysis by *Hsiung and Newell* [1983] and *Pan and Oort* [1983] indicated that ENSO variability in the tropical Pacific is correlated with a dipole-like structure in the SST anomaly field in the western North Atlantic. The cross spectral analysis which was presented earlier shows that inter-annual mode of simulated SST variability in the North Pacific is linked to ENSO. ENSO-related SST anomalies appear to be robust in the western North Pacific during summer (not shown). With regards to the atmospheric bridge driving SST anomalies, surface heat fluxes and Ekman transport creating SST anomalies in the central North Pacific are the key component of this mechanism (*Alexander et al.*, 2002). The atmospheric bridge not only influences SSTs on inter-annual time scales but also affects mixed layer depth (MLD), salinity, the seasonal evolution of upper-ocean temperatures, and North Pacific SST variability at lower frequencies (*Alexander et al.*, 2002). These model results indicate that a significant fraction of the dominant pattern of low-frequency (>10 year) SST variability in the North Pacific is associated with tropical forcing.

Atmosphere-ocean coupling outside of the tropical Pacific slightly modifies the atmospheric circulation anomalies in the Northern Hemisphere region but these modifications appear to depend on the seasonal cycle and air-sea interactions both within and beyond the North Pacific Ocean. During high frequency ENSO in Period A, an enhancement of AO-like atmospheric pattern as the leading modes of 500 hPa geopotential field and the Pacific-North American (PNA)-like as the second leading mode response to the perturbation. The AO-like (PNA-like) pattern appeared to be associated with a negative SST anomaly over the polar (the North Pacific) region during maximum perturbation. The energy from the western tropical Pacific forcing tends to propagate zonally to the North Atlantic because of the jet stream waveguide effect while the transport of the energy from the eastern tropical Pacific forcing mostly concentrates over the PNA area. Their results show that nonlinear processes are involved in the generation of the forced AO-like pattern (*Jia et al.*, 2009). Most recently, *Wu* [2010] confirmed this results, showing that the first maximum covariance analysis (MCA) mode of their analysis indicates a strong impact of tropical SST anomalies associated with ENSO on the extratropical atmosphere. The second MCA mode corresponds with coupling between Arctic

Oscillation (AO)-like atmospheric variations and tropical SST anomalies. An AO-like MCA mode appears to depict an atmosphere-to-ocean forcing, in which the tropical ocean responds to the higher extratropical AO-like atmospheric anomalies with an intraseasonal time lag. In winter, AO-like atmospheric variability is associated with the northern tropical Atlantic mode and the Central Pacific (CP) ENSO mode through enhanced or weakened trade winds. The above forced SST anomalies by the AO-like variability may also play a role in the subsequent evolution of the conventional ENSO phenomena (*Wu*, 2010).

c. How do those change effects the ocean circulation in the Pacific?

In response the freshwater perturbation, a strengthening of PMOC up to about 14 Sv is found, particularly in the tropical-subtropical region 20°S-20°N. The intensification of PMOC is also shown in the region of 50°-55°N, which is probably associated with the intensification of the subpolar gyre. During Period A, the North Pacific Subpolar gyre exhibits a deepening of mixed layer around the Gulf of Alaska. This deepening indicates a vigorous intensification of the Alaska current, while the shallowing MLD in the east of Japan might be related to weakening of Oyashio current and Kamchatka current. The deepening of the MLD in the subtropical gyre the north off-equatorial Pacific indicates an intensification of the North Equatorial current. The intensification of this ocean current is probably driven by intensified atmospheric circulation anomalies over the subarctic front (around 40-42°N) and in the north equator subtropical front which eventually increases the PMOC. This finding is similar to several studies which implied that the intermediate/deep water formation tends to resume in the North Pacific when the Atlantic MOC is suppressed (*Timmermann et al.*, 2007; *Krebs and Timmermann*, 2007; *Mikolajewicz et al.*, 2007).

Chapter 6

Outlook

Due to the limitation of time, the important issue which is not explored in this thesis is the role of sea ice and its interaction with the ocean and atmosphere. Sea ice, if present, acts as an insulator between the ocean and atmosphere, reducing the thermal damping of anomalously cold outflow from the Asian continent and thus amplifying the North Pacific cooling. *Cheng et al.* [2007] compared two sets of water-hosing experiments under different background states for the present day and Last Glacial Maximum (LGM)-the time of the maximum extent of the ice sheets during the last glacial (∼20 kyr ago). They found that the fundamental mechanisms for global adjustment to an AMOC weakening are similar between the two experiments. However, under the Last Glacial Maximum condition, the climatic impact is much more severe than that under the present-day condition primarily due to the more extensive distribution of sea ice and stronger ice-albedo feedback (*Cheng et al.*, 2007). The results of *Cheng et al.* [2007] and our analysis of the oceanic connection via the Bering Strait point to the importance of background states in determining the climate response to freshwater perturbations in the North Atlantic. Melting sea ice can freshen the ocean and reduce the density. Diminished sea ice also increases moisture fluxes into the atmosphere, which may increase fog and low cloud, adding further complexity to the net albedo change. Moreover, changes in the moisture fluxes will also drive changes in climate variability.

Besides the role of sea ice and its interaction with the ocean and atmosphere, the future investigation regards to this study is due to ocean dynamics and its properties. The suggested role of Rossby and Kelvin waves on ENSO variability need to be more explored, e.g., changes on pycnocline in the North Pacific and tropical Pacific region in response to freshwater discharge in the North Atlantic as well as general cooling in the North Pacific. The finding of the relationship between the climate shift in the tropical region which has also association to the Southern Ocean SST and wind stress field needs to be investigated.

It is also necessary to compare the Pacific climate variability (i.e. ENSO, PDO and Northern Hemisphere teleconnection pattern) during freshwater hosing (FN20) with the climate variability in the different equilibrium climate state such as in the LGM in association with AMOC slow downs in this experiment. *Toniazzo* [2006] using HadCM3 model showed that in his comparison of ENSO characteristics in the LGM, preindustrial period (CTRL), and in the greenhouse stabilization scenario (GHS), the SST variability pattern associated with ENSO is centered farther west, and the oscillation acquires a shorter dominant period from LGM to

CTRL, which are similar with the result of this thesis. Therefore, it is necessary to compare the result of this study with the climate state in the different climate conditions such as the Last Glacial Maximum or during Holocene period.

Chapter 7

Appendix

7.1 Empirical Orthogonal Function (EOF) and Rotated EOF

The Empirical Orthogonal Function (EOF) and the rotated EOF are two main methods for analyzing the spatial and temporal variability of geophysical fields. The EOF (or sometimes referred to as Principal Component Analysis (PCA) is a method of choice for analyzing the variability of scalar fields. The original purpose of EOFs was to reduce the large number of variables of the original data to a few variables, but without compromising much of the explained variance. Lately, however, EOF analysis has been used to extract individual modes of variability such as the Arctic Oscillation (AO), (*Thompson and Wallace*, 1998) known as teleconnections (*Bjerknes*, 1969; *Wallace and Gutzler*, 1981,etc.).

The EOF method finds the spatial patterns of variability, their time variation (time series), and gives a measure of the *importance* of each pattern (*Björnsson and S.A.*, 2007). Most authors refer to patterns as the *EOFs*, but some refer to them as the *Principal component leading patterns* or just the *principal components*. The time series referred to as *EOF time series* or *principal component time series*. For simplificity, this study will use EOF as the pattern term, and the time series are referred to as *principal components (PC)*.

An EOF analysis is a decomposition of a data set into a set of orthogonal functions which are determined from the data. These functions are chosen to account for as much variance as possible, and order in such a way, that the first EOF explains most variance. In spirit EOF method is similar to a Fourier analysis, but in the latter the orthogonal functions sin(x) and cos(x) are predefined and fixed. Similarity also exists to linear regression. Finding the EOFs requires computing the eigenvectors of the data covariance matrix whose elements are formed from the difference of the observations from their long-term means. The relative importance of any individual EOF to the total variance in the field is measured by its associated eigenvalue. Each EOF is associated with a series of time coefficients that describe the time evolution of the particular EOF. In this study, the EOF is used to examine variability of scalar (simple) fields only (such as SLP, SST, SAT, Z_{500}, etc).

Since EOF and rotated EOF are essentially matrix methods, which break the data into mode variability, it should be taken into account that these modes are primarily data modes, and

not necessarily physical modes. Whether they are physical will be a matter of interpretation (see *Newman and Sardeshmukh*, 1995 for a detailed discussion). A brief mathematical background of this method and climatic data processing will be shortly presented as following. More detailed information can be found in *Hannachi* [2004] as most of this part taken from his short note on EOF. For a comprehensive overview of EOF method, the reader is suggested to refer *Storch and Zwiers* [2002].

Gridded climate data normally come as an array containing for each vertical level a three-dimensional, two-dimensional in space and one-dimensional in time, field *F*. The latter is a function of time *t*, latitude θ, and longitude ϕ. Suppose that the horizontal coordinates are discretised to yield latitudes θ_j, $j = 1,\ldots, p1$, and longitudes ϕ_k, $k = 1,\ldots p2$, and similarly for time, i.e. t_i, i = 1,... *n*. This yields a total number of grid points $p = p1 \cdot p2$. The discretised field reads:

$$F_{ijk} = F(t_i, \theta_j, \phi_k), \tag{7.1}$$

with $1 \leq i \leq n$, $1 \leq j \leq p1$, and $1 \leq$ k $\leq p2$. To avoid a memory consuming to process three- and higher-dimensional arrays such as F, hence, it is needed to transform F into a two-dimensional array : *the data matrix X* where the two spatial dimensions are concatenated together.

Suppose a gridded data set composed of a space-time field $X(t,\ s)$ representing the value of the field X, such as SST, at time t and spatial position s. The value of the field at discrete time t_i and grid point s_j is noted x_{ijk} for $i = 1,\ldots,n$ and $j = 1,\ldots p = p1 \cdot p2$. The observed field is then represented by the data matrix:

$$X = \begin{pmatrix} a_{11} & a_{12} & \cdots & a_{1p} \\ a_{21} & a_{22} & \cdots & a_{2p} \\ \vdots & \vdots & \ddots & \vdots \\ a_{n1} & a_{n2} & \cdots & a_{np} \end{pmatrix}, \tag{7.2}$$

If the time average of the field[1] is denoted by $\overline{x}_j$ at the jth grid point, i.e.,

$$\overline{x}_j = \frac{1}{n} \sum_{k=1}^{n} x_{kj}, \tag{7.3}$$

then the climatology of the field is defined by $\overline{x} = (\overline{x}_1, \ldots, \overline{x}_p)$, and the anomaly field, or departure from the climatology is defined at $(t,\ s)$ by: $x'_{ts} = x_{ts}$ - $\overline{x}_s$, or in matrix form

$$X' = X - \overline{X} = \left(\mathbf{I} - \frac{1}{n} \mathbf{1}\mathbf{1}^T \right) X, \tag{7.4}$$

where $\mathbf{1} = (1, \ldots 1)^T$ is the (column) vector containing n ones, and $\mathbf{I}$ is the n $\times$ n identity matrix.

Area weighting

[1]The seasonal and other external, e.g.,diurnal cycles are supposed to have been removed from the data

Most climate data, whether observed or model-simulated, are in general non-uniformly distributed over the Earth surface. For example, if the data are provided on a grid with 3.75° × 3.75° resolution, then clearly the distribution of the data will be denser poleward. This non-uniform distribution influences the structure of the computed EOFs. In order to avoid the effect of this geometrical artifact we normally weight the data prior to the analysis. The simplest and most useful way is to weight each data point by the area. Hence each datum is weighted by the cosine of its latitude. Let us designate by θ_k the latitude of the kth grid point, $k = 1,\ldots p$, and D_θ the diagonal matrix:

$$D_\theta = Diag[\cos\theta_1, \ldots, \cos\theta_p] \tag{7.5}$$

Then the weighted anomaly matrix is $X_w = X'D_\theta$.

Once the anomaly data matrix or its weighted version is determined, the covariance matrix is then defined by:

$$\Xi = \frac{1}{n-1} X'^T X' \tag{7.6}$$

which contains the covariance between any pair of grid points. The aim of EOF/PCA is to find the linear combination of all the variables, i.e., grid points, that explains maximum variance. That is to find a direction $\mathbf{a} = (a_1, \ldots, a_p)^T$ such that $X'a$ has maximum variability. Now the variance of the (centered) time series $X'a$ is

$$var(X'a) = \frac{1}{n-1} \parallel X'a \parallel^2 = \frac{1}{n-1}(X'a)^T X'a = a^T \Xi a. \tag{7.7}$$

To make the problem bounded we normally require the vector a to be unitary. Hence the problem readily yields: $max(a^T \Xi a)$, so that $a^T a = 1$. This solution is already a simple eigenvalue problem (EVP):

$$\Xi a = \lambda a \tag{7.8}$$

By definition the covariance matrix Ξ is symmetric and therefore diagonalisable. The kth EOF is simply the kth eigenvector a_k of Ξ after the eigenvalues, and the corresponding eigenvectors, have been sorted in decreasing order. The covariance matrix is also semidefinite, hence all its eigenvalues are positive. The eigenvalue λ_k corresponding to the kth EOF gives a measure of the explained variance by a_k, $k = 1,\ldots p$. It is usual to write the explained variance in percentage as:

$$\frac{\lambda_k}{\sum_{k=1}^{p} \lambda_k} \cdot 100\%. \tag{7.9}$$

The projection of the anomaly field X' onto the kth EOF a_k, i.e., $c_k = X'a_k$ is the kth principal component (PC)

$$c_k(t) = \sum_{s=1}^{p} x'(t,s) a_k(s) \tag{7.10}$$

Because Ξ is diagonalisable the set of its eigenvectors forms an orthogonal basis of the p-dimensional Euclidean space, defined with the natural scalar product. So by construction, the Empirical Orthogonal Functions are orthogonal and the PCs uncorrelated. This completely

characterizes conventional EOFs. The orthogonality property provides a complete basis where the time-varying field can be separated as:

$$X'(t,s) = \sum_{k=1}^{M} c_k(t) a_k(s) \tag{7.11}$$

where the total variance contained in the M EOFs (dimensional space) equals to the total variance in the M time series.

The principal component attached to the corresponding EOF provides the sign and the overall amplitude of the EOF as a function of time. This provides a simplified representation of the state of the field at that time along that EOF. In other words EOFs do not change structure in time, they only change sign and overall amplitude to represent the state of the atmosphere(*Hannachi*, 2004).

Although EOFs represent patterns that explain most of the observed variability, their interpretation is not always simple. Physical interpretability especially can be controversial (see *Dommenget and Latif*, 2002), since physical modes are not necessarily orthogonal (*Simmons et al.*, 1983). The constraints imposed upon EOFs are purely geometric and hence can be non-physical. Furthermore, the EOF structure tends to be domain (area) dependent (*Richman*, 1986). The orthogonality constrains makes the physical interpretation difficult. These arguments constitute the main reasons for attempts to find ways around EOFs. The method of rotated EOFs, constitutes one way. Rotating means that another sub set of EOFs is found, where the PCs need not be orthogonal, i.e. they can be correlated with each other. The technique is also known in factor analysis as factor rotation and aims at getting simple structures, more local features, and be able to physically interpret the patterns (*Dommenget and Latif*, 2002).

In this study, rotated EOFs is applied by using Kaiser row normalization and the varimax criterion. The Kaiser varimax rotation is a common rotation performed on atmospheric or oceanographic data. Rotation of the spatial modes (i.e. EOFs) is called R-mode while rotation of the amplitude time series (expansion coefficients) is called Q-mode. The focus of Q-mode analysis is inter-object relationships. Q-mode analysis is not commonly used today due to the advent of cluster analysis. R-mode rotation focuses upon inter-variable relationships such as the covariance/correlation between stations or grid points.

Generally, it is R-mode rotation that is performed on atmospheric/oceanographic data. The objective of R-mode analysis is to derive simple structures. Under Kaiser varimax rotation this is accomplished by performing an orthonormal rotation on a user specified number of modes such that some values are near +/–1 with many near 0 values. The effect is to localize the main centers of action and maximize the regions of small weightings (*Trenberth et al.*, 2005). The result of varimax rotation upon standard EOFs are rotated EOFs that are orthonormal. However, the temporal patterns derived by projecting the rotated spatial patterns onto the data will not be orthogonal. This means that the there is some correlation between the time series expansion coefficients for each mode. The reverse is the case for Q-mode analysis.

7.2 Power Spectra Analysis

Since the collection of a variety of data, time series analysis has been one of the key tools for the investigation of climate dynamics. The variability of climate has thus been shown to occur on all time scales, with large cycles varying from diurnal, annual and astronomical cycles and the variations linked to plate tectonics over millions of years (*Peixoto and Oort*, 1992). Moreover, the analysis of time series has shown the irregular and chaotic spatio-temporal behavior of climate variations (*Ghil et al.*, 2002). The analysis of time series provides a bridge between phenomenological description through observation and the study of the underlying climate dynamics (*Ghil and Childress*, 1987). The power spectra analysis has been used in this study to examine a dominant timescale of the indices, such as Niño3.4 SST index and the PDO and decadal-ENSO indices for observation, control simulation run and during freshwater hosing experiment.

In this section the theory of power spectra will be briefly described based on the paper of *Hibler and LeShack*, 1972. For simplicity we will consider an infinite, continuous time series. In practice, of course, one has a finite digitized sample and a finite data window whose transform is convoluted with the desired "true" power spectrum. Suppose a given time series *X(t)*, the time average can be written as,

$$\rho(\tau) = \lim_{\tau\to\infty} \frac{1}{T} \int_{-\tau/2}^{\tau/2} \eta(t) \quad \eta(t+\tau)dt \tag{7.12}$$

where $\eta(t) = X(t) - \overline{X}(t)$ is called the auto-covariance function, with τ being called the lag time. The quantity,

$$C(f) = \int_{-\infty}^{\infty} \rho(\tau) \cos 2\pi f\tau d\tau \tag{7.13}$$

is called the power spectrum. Power-spectrum estimates for given time series are usually plotted in terms of relative amplitude per unit frequency versus incremental frequency bandwidths. The frequency units are denoted by wave-number with the highest wave-number corresponding to the Nyquist frequency $1/(2\Delta T)$ where ΔT is the sampling interval.

From the above definition of the power spectrum it is easily shown that $C(f)$ is also given by:

$$C(f) = \lim_{\tau\to\infty} \frac{1}{T} \mid \int_{-\tau/2}^{\tau/2} \eta(t) \quad e^{2\pi ift} dt \mid^2 \tag{7.14}$$

This expression is most useful for interpretation because the right-hand side is simply the square of the Fourier transform of $\eta(t)$. This procedure is, in fact, simply one way of carrying out a Fourier analysis. Since the auto-covariance function consists of an average over many data points, its spectrum more nearly represents the "true" spectrum (*Blackman and Tukey*, 1958; *Percival and Walden*, 1993) of the time series. Calculating the auto-covariance function is also a way of smoothing the data. From the general theory of power spectra one can predict, from the number of data points and the number of lags, the confidence limits

(*Blackman and Tukey*, 1958; *Jenkins and Watts*, 1968) of a given spectrum about the "ideal" spectrum assuming a stationary Gaussian process. The confidence limits may be determined from the equivalent degrees of freedom per spectral point. These confidence limits are quite useful in determining the significance of a given spectral peak.

7.3 Wavelet Analysis

The wavelet transform can be used to analyze time series that contain nonstationary power at many different frequencies (cf. *Torrence and Compo*, 1998). Assume that one has a time series x_n, with equal time spacing δt and $n = 0 \ldots N-1$. Also assume that one has a wavelet function, $\psi_0(\eta)$, that depends on a nondimensional time parameter η. To be admissible as a wavelet, this function must have zero mean and be localized in both time and frequency space (cf. *Torrence and Compo*, 1998).

A wavelet function (for example the Morlet wavelet), consisting of a plane wave modulated by a Gaussian

$$\psi_0(\eta) = \phi^{-1/4} e^{i\omega_0 \eta} e^{-\eta^2/2} \tag{7.15}$$

Where η is a normalized time and ω is the nondimensional frequency.
The continuous wavelet transformation of a discrete series x_n is defined as the convolution of x_n with a scaled and translated version of $\psi_0(\eta)$

$$W_n(s) = \frac{1}{N} \sum_{n=0}^{N-1} x_n \psi^* [\frac{(\eta' - \eta)\delta t}{s}] \tag{7.16}$$

where s is the wavelet scale. By varying the s and translating along the localized time index n, one constructs a picture showing both the amplitude of any feature verses the scale and how this amplitude varies with time. While this above equation can be used to calculate the wavelet transformation, it is much faster to do it in the frequency domain (Fourier Space).

To approximate the continuous wavelet transformation the above convolution would be done N times for each scale, where N is the number of data points in the record. By choosing N points the convolution theorem allows us to do all N convolutions simultaneously in Fourier space using a discrete transformation

$$\hat{x}_k = \sum_{n=0}^{N-1} x_n e^{-2\pi i k n/N} \tag{7.17}$$

Thus by the convolution theorem the wavelet transformation is the inverse Fourier transform of the product (note that the Fourier transform of a function $\psi(t/s) = \psi(sw)$)

$$W_n(s) = \sum_{n=0}^{N-1} \hat{x}_k \psi(s\omega_k) e^{iwk_n \delta t} \tag{7.18}$$

$$\omega_k = \begin{cases} \frac{2\pi k}{N\delta t} & \text{if } k \leq N/2 \\ -\frac{2\pi k}{N\delta t} & \text{if } k > N/2 \end{cases}$$

To ensure that the wavelet transform transformation at each scale are comparable the wavelet function needs to be normalized for each s so that it has unit energy.

$$\hat{\psi} s w_k = (\frac{2\pi s}{\partial t})\hat{\psi}_0(s\omega_k) \tag{7.19}$$

The wavelet functions are already normalized because

$$\int_{-\infty}^{\infty} \mid \hat{\psi}_0(w') \mid^2 \partial w' = 1$$

Using these normalizations, at each scale s one has $\sum_{k=0}^{N-1} \mid \hat{\psi}(s\omega_k) \mid^2 = N$. Thus the wavelet transform is weighted only by the amplitude of the function x_k and not by the wavelet function.

Like the Fourier transform, the wavelet transform is in general complex and is often characterized in terms of it's power. The transform can then be divided into the real part and imaginary part, or amplitude, and phase. Finally, one can define the wavelet power spectrum as $\mid W_n(s) \mid^2$. For real-valued wavelet functions such as the DOGs (derivatives of a Gaussian) the imaginary part is zero and the phase is undefined. For further explanation, the reader is suggested to refer *Torrence and Compo* [1998].

7.4 Correlation and Teleconnection Map

Basic idea of the correlation method is to correlate the time series of a particular variable at one particular location with the time series of another variable at every grid point of a particular region (i.e. Northern Hemisphere). For instance, a point correlation map of monthly mean sea surface temperature in Nino3.4 region with the mean surface pressure at every point in the northern and southern hemisphere. Teleconnection is achieved by repeating a correlation map for all points within a region (or worldwide) and select the value at the point with strongest negative correlation. Teleconnetion patterns refer to recurring and persistent, large-scale pattern of circulation anomalies.

List of Tables

List of Figures

Bibliography

Alexander, M. A., Midlatitude Atmosphere - Ocean Interaction during El Niño. Part I: The North Pacific ocean, *Journal of Climate, 5*(9), 944–958, 1992.

Alexander, M. A., I. Blad, M. Newman, J. R. Lanzante, N.-C. Lau, and J. D. Scott, The atmospheric bridge: The influence of ENSO teleconnections on air-sea interaction over the Global Oceans, *Journal of Climate, 15*(16), 2205–2231, 2002.

Ashok, K., S. K. Behera, S. A. Rao, H. Weng, and T. Yamagata, El Niño Modoki and its possible teleconnection, *J. Geophys. Res., 112*, 2007.

Barnett, T. P., An attempt to verify some theories of El Niño, *Journal of Physical Oceanography, 7*(5), 633–647, 1977.

Barnett, T. P., D. W. Pierce, M. Latif, D. Dommenget, and R. Saravanan, Interdecadal interactions between the Tropics and midlatitudes in the Pacific basin, *Geophys. Res. Let., 26*(5), 615–618, 1999.

Barnston, A. G., and R. E. Livezey, Classification, seasonality and persistence of low-frequency atmospheric circulation patterns, *Monthly Weather Review, 115*(6), 1083–1126, 1987.

Barreiro, M., A. Fedorov, R. Pacanowski, and S. G. Philander, Abrupt climate changes: How freshening of the Northern Atlantic affects the thermohaline and wind-driven oceanic circulations, *Annual Review of Earth and Planetary Sciences, 36*(1), 33–58, 2008.

Behl, R. J., and J. P. Kennett, Brief interstadial events in the Santa Barbara basin, NE Pacific, during the past 60 kyr, *Nature, 379*, 243–246, 1996.

Bjerknes, J., Atmospheric teleconnections from the equatorial Pacific, *Monthly Weather Review, 97*(3), 163–172, 1969.

Björnsson, H., and V. S.A., *A Manual of EOF and SVD Analysis of Climatic Data*, McGill University, 2007.

Blackman, R., and W. Tukey, J., *The measurement of power spectra from the point of view of communication engineering*, Dover Publications, 1958.

Blunier, T., and E. J. Brook, Timing of millennial-scale climate change in Antarctica and Greenland during the last glacial period, *Science, 291*, 109–112, 2001.

Blunier, T., J. Chappellaz, J. Schwander, A. Dällenbach, B. Stauffer, T. F. Stocker, D. Raynaud, J. Jouzel, H. B. Clausen, C. U. Hammer, and S. J. Johnsen, Asynchrony of Antarctic and Greenland climate change during the last glacial period, *Nature, 394*, 739–743, 1998.

Boccaletti, G., R. C. Pacanowski, S. George, H. Philander, and A. V. Fedorov, The thermal structure of the upper ocean, *Journal of Physical Oceanography, 34*(4), 888–902, 2004.

Bonan, G. B., and S. Levis, Evaluating aspects of the community land and atmosphere models (CLM3 and CAM3) using a dynamic global vegetation model, *Journal of Climate, 19*(11), 2290–2301, 2006.

Bonan, G. B., K. W. Oleson, M. Vertenstein, S. Levis, X. Zeng, Y. Dai, R. E. Dickinson, and Z.-L. Yang, The land surface climatology of the community land model coupled to the ncar community climate model, *Journal of Climate, 15*(22), 3123–3149, 2002.

Bond, G., W. Broecker, S. Johnsen, J. McManus, L. Labeyrie, J. Jouzel, and G. Bonani, Correlations between climate records from North Atlantic sediments and Greenland ice, *Nature, 365*, 143–147, 1993.

Boville, B. A., P. J. Rasch, J. J. Hack, and J. R. McCaa, Representation of clouds and processes in the community atmosphere model (CAM3), *Journal of Climate, 19*, 2184–2198, 2006.

Broecker, W., D. M. Peteet, and D. Rind, Does the ocean-atmosphere system have more than one stable mode of operation?, *Nature, 315*, 21–25, 1985.

Broecker, W. S., Thermohaline circulation, the Achilles heel of our climate system: Will man-made CO_2 upset the current balance?, *Science, 278*, 1582–1588, 1997.

Broecker, W. S., and G. H. Denton, The role of ocean-atmosphere reorganizations in glacial cycles, *Geochim. Cosmochim. Acta, 53*, 2465–2501, 1989.

Carton, J. A., G. Chepurin, X. Cao, and B. Giese, A simple ocean data assimilation analysis of the global upper ocean 1950-95. Part I: Methodology, *Journal of Physical Oceanography, 30*(2), 294–309, 2000.

Cheng, W., C. M. Bitz, and J. C. H. Chiang, Adjustment of the global climate to an abrupt slowdown of the atlantic meridional overturning circulation. ocean circulation: Mechanisms and impacts, *Geophys. Monogr.,* (173), 295–314, 2007.

Chiang, J. C., The Tropics in paleoclimate, *Annual Review of Earth and Planetary Sciences, 37*(1), 263–297, 2009.

Chiang, J. C. H., M. Biasutti, and D. S. Biasutti, Sensitivity of the Atlantic Inter-tropical Zone to Last Glacial Maximum boundary conditions, *Paleoceanogr., 4*, 529–541, 2003.

Clarke, G. K., D. W. Leverington, J. T. Teller, and A. S. Dyke, Superlakes, megafloods, and abrupt climate change, *Nature, 301*, 922–923, 2003.

Clement, A., R.Seager, and M. Cane, Orbital controls on the El Niño Southern Oscillation and the tropical climate, *Paleoceanography, 15*, 441–456, 1999.

Clement, A. C., and L. C. Peterson, Mechanisms of abrupt climate change of the last glacial period, *Rev. Geophys., 46*(RG4002), 2008.

Collins, W. D., C. M. Bitz, M. L. Blackmon, G. B. Bonan, C. S. Bretherton, J. A. Carton, P. Chang, S. C. Doney, J. J. Hack, T. B. Henderson, J. T. Kiehl, W. G. Large, D. S. McKenna, B. D. Santer, and R. D. Smith, The Community Climate System Model Version 3 (CCSM3), *Journal of Climate, 19*, 2006.

Collins, W. D., P. J. Rasch, B. A. Boville, J. J. Hack, D. L. McCaa, D. L. Williamson, C. M. Briegleb, S. J. Bitz, S. J. Lin, and M. Zhang, The formulation and atmospheric simulation of the community atmosphere model: CAM3, *Journal of Climate, 19*, 2144–2161, 2006.

Corti, S., F. Molteni, and T. N. Palmer, Signature of recent climate change in frequencies of natural atmospheric circulation regimes, *Nature, 398*, 799802, 1999.

Danabasoglu, G., W. G. Large, J. J. Tribbia, P. R. Gent, B. P. Briegleb, and J. C. McWilliams, Diurnal coupling in the tropical oceans of CCSM3, *Journal of Climate, 19*, 2347–2365, 2006.

Dansgaard, W., S. J. Johnsen, H. B. Clausen, D. Dahl-Jensen, N. S. Gundestrup, C. U. Hammer, C. S. Hvidberg, J. P. Steffensen, A. E. Sveinbjörnsdóttir, J. Jouzel, and G. Bond, Evidence for general instability of past climate from a 250-kyr ice-core record, *Nature, 364*, 218–220, 2003.

de Boyer Montégut, C., J. Mignot, A. Lazar, and S. Cravatte, Control of salinity on the mixed layer depth in the world ocean: 1. General description, *Journal of Geophysical Research (Oceans), 112*, 6011, 2007.

Denton, G. H., R. F. Anderson, J. R. Toggweiler, R. L. Edwards, J. M. Schaefer, and A. E. Putnam, The last glacial termination, *Science, 328*(5986), 1652–1656, 2010.

Deser, C., and M. L. Blackmon, On the relationship between tropical and North Pacific sea surface temperature variations, *Journal of Climate, 8*(6), 1677–1680, 1995.

Deser, C., A. Capotondi, R. Saravanan, and A. S. Phillips, Tropical Pacific and Atlantic climate variability in CCSM3, *Journal of Climate, 19*, 2451–2481, 2006.

Dommenget, D., and M. Latif, A cautionary note on the interpretation of EOFs, *Journal of Climate, 15*(2), 216–225, 2002.

Dong, B. W., and R. T. Sutton, Adjustment of the coupled ocean-atmosphere system to a sudden change in the thermohaline circulation, *J. Geophys. Res., 29*, 1728, 2002.

EPICA Community Members, One-to-one coupling of glacial climate variability in Greenland and Antarctica, *Nature, 444*, 195–198, 2006.

Fedorov, A. V., and S. G. Philander, A stability analysis of tropical oceanatmosphere interactions: Bridging measurements and theory for El Niño, *Journal of Climate, 14*(14), 3086–3101, 2001.

Frankignoul, C., and K. Hasselmann, Stochastic climate models, Part II: Application to sea-surface temperature anomalies and thermocline variability, *Tellus, 29*, 289–305, 1977.

Ghil, M., M. R. Allen, M. D. Dettinger, K. Ide, D. Kondrashov, M. E. Mann, A. W. Robertson, A. Saunders, Y. Tian, F. Varadi, and P. Yiou, Advanced spectral methods for climatic time series, *Rev. Geophys., 40*(1), 1363–1392, 2002.

Ghil, M., and S. Childress, *Topics in Geophysical Fluid Dynamics: Atmospheric Dynamics, Dynamo Theory, and Climate Dynamics*, Volume 60, Applied Mathematical Sciences, 1987.

Giese, B. S., and J. A. Carton, Interannual and decadal variability in the tropical and midlatitude Pacific ocean, *Journal of Climate, 12*(12), 3402–3418, 1999.

Gill, A. E., *Atmosphere Ocean Dynamics*, Volume 30, International Geophysics Series, 1982.

Graham, N. E., Decade-scale climate variability in the tropical and North Pacific during the 1970s and 1980s: Observations and model results, *Clim. Dyn., 10*, 135–162, 1994.

Gu, D., S. G. H. Philander, and M. J. McPhaden, The seasonal cycle and its modulation in the eastern tropical Pacific ocean, *Journal of Physical Oceanography, 27*(10), 2209–2218, 1997.

Guilyardi, E., P. Braconnot, F.-F. Jin, S. T. Kim, M. Kolasinski, T. Li, and I. Musat, Atmosphere feedbacks during ENSO in a coupled gcm with a modified atmospheric convection scheme, *Journal of Climate, 22*(21), 5698–5718, 2009.

Hannachi, A., *A Primer for EOF Analysis of Climate Datas*, Department of Meteorology, University of Reading, 2004.

Hare, S. R., and N. J. Mantua, Empirical evidence for North Pacific regime shifts in 1977 and 1989, *Progress in Oceanography, 47*(2-4), 103–45, 2000.

Hasselmann, K., Stochastic climate models, Part I: Theory, *Tellus, 28*, 473–485, 1976.

Hemming, S. R., Heinrich events: Massive late Pleistocene detritus layers of the North Atlantic and their global climate imprint, *Reviews of Geophysics, 42*, 2004.

Hibler, W. D., and L. A. LeShack, Power spectrum analysis of undersea and surface sea-ice profiles, *Journal of Glaciology, 11*(63), 345–356, 1972.

Hsiung, J., and R. E. Newell, The principal nonseasonal modes of variation of global sea surface temperature, *Journal of Physical Oceanography, 13*(10), 1957–1967, 1983.

Hu, A., G. Meehl, and W. Han, Role of the Bering Strait in the thermohaline circulation and abrupt climate change, *Geophys. Res. Let., 34*, L05704, 2007.

Hu, A., B. Otto-Bliesner, G. A. Meehl, W. Han, C. Morrill, E. C. Brady, and B. Briegleb, Response of thermohaline circulation to freshwater forcing under present-day and LGM conditions, *J. Climate, 21*, 2239–2258, 2008.

Hu, S. F., D. M. Nelson, G. H. Clarke, K. M. Ruhland, Y. S. Huang, and D. S. Kaufman, Abrupt climatic events during the last glacial-interglacial transition in Alaska, *Geophys. Res. Let., 33*, 2006.

Hurrell, J. W., Y. Kushnir, G. Ottersen, and V. Martin, An overview of the North Atlantic Oscillation, in *The North Atlantic Oscillation: Climatic Significance and environmental impact.*, edited by Y. Hurrell, James W.and Kushnir, G. Ottersen, and M. Visbeck, Volume 134 of *Geophysical Monograph*, pp. 263–284, Am. Geophys. Union, Washington, D. C., 2003.

IPCC, *Summary for Policymakers in Climate Change 2007 : The Physical Science Basis*, Cambridge University Press, Cambridge, United Kingdom and New York, NY, USA., 2007.

Jenkins, G. M., and D. G. Watts, *Spectral Analysis and its Application*, Holden-Day, 1968.

Jia, X. J., H. Lin, and J. Derome, The influence of tropical Pacific forcing on the arctic oscillation, *Journal of Climate, 32*(4), 495–509, 2009.

Jin, D., and B. P. Kirtman, How the annual cycle affects the extra-tropical response to ENSO, *J. Geophys. Res., 115*(DO6102), 2010.

Jones, P. D. T. J. O., K. R. Briffa, E. B. H. C. K. Folland, L. V. Alexander, D. E. Parker, and N. A. Rayner, Adjusting for sampling density in grid box land and ocean surface temperature time series, *J. Geophys. Res., 106*, 33713380, 2001.

Kao, H.-Y., and J.-Y. Yu, Contrasting eastern-Pacific and central-Pacific types of ENSO, *Journal of Climate, 22*(3), 615–632, 2009.

Katz, R. W., Sir Gilbert Walker and a connection between El Niño and statistics, *Statistical Science, 17*(1), 97112, 2002.

Kiehl, J., J. Hack, G. Bonan, B. Boville, D. Williamson, and P. Rash, The National Center for Atmospheric Research community climate model: CCM3, *Bull. Amer. Meteor. Soc., 11*, 1131–1149, 1998.

Kiehl, J. T., and P. R. Gent, The Community Climate System Model, version 2, *Journal of Climate, 17*, 3666–3682, 2004.

Kienast, S. S., and J. L. McKay, Sea surface temperatures in the subarctic Northeast Pacific reflect millennial-scale climate oscillations during the last 16 kyrs, *Geophys. Res. Let., 28*, 1563–1566, 2001.

Kirtman, B. P., and E. K. Schneider, Model-based estimates of equatorial Pacific wind stress, *Journal of Climate, 9*(5), 1077–1091, 1996.

Kleeman, R., J. McCreary, Julian P., and B. A. Klinger, A mechanism for generating ENSO decadal variability, *Geophys. Res. Let., 26*(12), 1743–1746, 1999.

Knutson, X., and S. Manabe, Model assessment of decadal variability and trends in the tropical Pacific ocean, *Journal of Climate, 11*, 2273–2296, 1998.

Krebs, U., and A. Timmermann, Tropical Air-Sea interactions accelerate the recovery of the Atlantic meridional overturning circulation after a major shutdown, *Journal of Climate, 20*(19), 4940–4956, 2007.

Kug, J.-S., J. Choi, S.-I. An, F.-F. Jin, and A. T. Wittenberg, Warm pool and cold tongue El Niño events as simulated by the GFDL 2.1 coupled GCM, *Journal of Climate, 23*(5), 1226–1239, 2010.

Kuhlbrodt, T., A. Griesel, M. Montoya, A. Levermann, M. Hofmann, and S. Rahmstorf, On the driving process of the Atlantic meridional overturning circulation, *Rev. Geophys., 45*, RG2001, 2007.

Larkin, N. K., and D. E. Harrison, On the definition of El Niño and associated seasonal average u.s. weather anomalies, *Geophys. Res. Let., 32*(13), 2005.

Latif, M., and T. P. Barnett, Decadal climate variability over the North Pacific and North America: Dynamics and predictability, *Journal of Climate, 9*(10), 2407–2423, 1996.

Lau, N.-C., and M. J. Nath, The role of the Atmospheric Bridge in linking tropical Pacific ENSO events to extratropical SST anomalies, *Journal of Climate, 9*(9), 2036–2057, 1996.

Lau, N.-C., and M. J. Nath, Impact of ENSO on sst variability in the North Pacific and North Atlantic: Seasonal dependence and role of Extra-tropical sea-air coupling, *Journal of Climate, 14*(13), 2846–2866, 2001.

Leduc, G., L. Vidal, K. Tachikawa, F. Rostek, C. Sonzogni, and e. a. Beaufort, L., Moisture transport across Central America as a positive feedback on abrupt climatic changes, *Nature, 445*, 908–911, 2007.

Levitus, S., T. Boyer, M. Conkright, D. Johnson, T. O'Brien, J. Antonov, C. Stephens, and R. Gelfeld, Introduction, Vol. 1, World Ocean Database 1998, NOAA Atlas NESDIS 18, pp. 346, 1998.

Li, C., L. Wu, Q. Wang, L. Qu, and L. Zhang, An intimate coupling of ocean-atmospheric interaction over the extra-tropical North Atlantic and Pacific, *Clim. Dyn., 32*, 753–765, 2009.

Liu, Z., and S. G. H. Philander, How different wind stress patterns affect the tropical-subtropical circulations of the upper ocean, *Journal of Physical Oceanography, 25*(4), 449–462, 1995.

Lund, D. C., and A. C. Mix, Millennial-scale deep water oscillations: Reflections of the North Atlantic in the deep Pacific from 10 to 60 ka, *Paleoceanography, 13*, 10–19, 1998.

Luo, J.-J., and T. Yamagata, A model study on the 1988-89 warming event in the northern North Pacific, *Journal of Physical Oceanography, 33*(8), 1815–1828, 2003.

Luo, Z., and M. Alexander, Atmospheric bridge, oceanic tunnel, and global climatic teleconnections, *Rev. Geophys., 45*, RG2005, 2007.

Lysne, J. A., and C. Deser, Wind-driven thermocline variability in the Pacific: A model-data comparison, *Journal of Climate, 15*(8), 829–845, 2002.

Manabe, S., and R. J. Stouffer, Two stable equilibria of a coupled ocean-atmosphere model, *Journal of Climate, 1*, 841–866, 1988.

Mantua, N., and S. Hare., The Pacific Decadal Oscillation, *Journal of Oceanography, 58*(1), 35–44, 2002.

Mantua, N. J., S. R. Hare, Y. Zhang, J. M. Wallace, and R. C. Francis, A Pacific interdecadal climate oscillation with impacts on salmon production, *Bulletin of the American Meteorological Society, 78*(6), 1069–1079, 1997.

McAfee, S. A., and J. L. Russell, Northern Annular Mode impact on spring climate in the western united states, *Geophys. Res. Let., 35*(L17701), 2008.

McCreary, J. P., and P. Lu, Interaction between the Subtropical and Equatorial ocean circulations: The subtropical cell, *Journal of Physical Oceanography, 24*(2), 466–497, 1994.

McGregor, S., N. J. Holbrook, and S. B. Power, Interdecadal sea surface temperature variability in the equatorial Pacific ocean. Part I: The role of off-equatorial wind stresses and oceanic rossby waves, *Journal of Climate, 20*(11), 2643–2658, 2007.

McGregor, S., N. J. Holbrook, and S. B. Power, Interdecadal sea surface temperature variability in the equatorial Pacific ocean. Part II: The role of equatorial off-equatorial wind stresses in a hybrid coupled model, *Journal of Climate, 21*(17), 4242–4256, 2008.

McGregor, S., N. J. Holbrook, and S. B. Power, The response of a stochastically forced ENSO model to observed off-equatorial wind stress forcing, *Journal of Climate, 22*(10), 2512–2525, 2009.

McManus, J. F., R. Francois, J. M. Gherardi, L. D. Keigwin, and S. Brown-Leger, Collapse and rapid resumption of Atlantic meridional circulation linked to deglacial climate change, *Nature, 428*, 834–837, 2004.

Mikolajewicz, U., T. J. Crowley, A. Schiller, and R. Voss, Modelling teleconnections between the North Atlantic and North Pacific during the Younger Dryas, *Nature, 387*, 384–387, 1997.

Mikolajewicz, U., M. Groger, E. Maier-Reimer, G. Schurgers, M. Vizcaino, and A. M. E. Winguth, Long-term effects of anthropogenic CO_2 emissions simulated with a complex earth system model, *Clim. Dyn., 28*, 599–633, 2007.

Minobe, S., A 50-70 year climatic oscillation over the North Pacific and North America, *Geophys. Res. Let., 24*, 683–686, 1997.

Moelg, T., M. Renold, M. Vuille, N. J. Cullen, T. F. Stocker, and G. Kaser, Indian Ocean Zonal Mode activity in a multicentury-integration of a coupled AOGCM consistent with climate proxy data, *Geophys. Res. Let., 33*, L18710, 2006.

Nakamura, H., G. Lin, and T. Yamagata, Decadal climate variability in the North Pacific during the recent decades, *Bulletin of the American Meteorological Society, 78*(10), 2215–2225, 1997.

Neelin, J. D., and F.-F. Jin, Modes of interannual tropical oceanatmosphere interactiona unified view. Part II: Analytical results in the weak-coupling limit, *Journal of the Atmospheric Sciences, 50*(21), 3504–3522, 1993.

Newman, M., and P. D. Sardeshmukh, A caveat concerning Singular Value Decomposition, *Journal of Climate, 8*(2), 352–360, 1995.

Nof, D., Is there a meridional overturning cell in the Pacific and Indian oceans?, *Journal of Physical Oceanography, 32*(6), 1947–1959, 2002.

North GRIP Members, High resolution climate record of the northern hemisphere reaching into the last glacial interglacial period, *Nature, 431*, 147151, 2004.

Oka, A., and H. Hasumi, Effects of model resolution on salt transport through northern high-latidude passages and Atlantic meridional overturning circulation, *Ocean Modelling, 13*, 126–147, 2006.

Okumura, Y. M., C. Deser, A. Hu, A. Timmermann, and S.-P. Xie, North Pacific climate response to freshwater forcing in the subarctic North Atlantic: Oceanic and atmospheric pathways, *Journal of Climate, 22*(6), 1424–1445, 2009.

Otto-Bliesner, B. L., and E. C. Brady, The sensitivity of the climate response to the magnitude and location of freshwater forcing: last glacial maximum experiments, *Quaternary Science Reviews, 29*(1-2), 56 – 73, 2010.

Pan, Y. H., and A. H. Oort, Global climate variations connected with sea surface temperature anomalies in the eastern equatorial Pacific ocean for the 195873 period, *Monthly Weather Review, 111*(6), 1244–1258, 1983.

Peixoto, J. P., and A. H. Oort, *Physics of Climate.*, Volume 6, Amer. Inst. Phys., 1992.

Percival, D., and A. Walden, *Spectral analysis for physical applications–Multitaper and conventional univariate techniques*, Cambridge University, 1993.

Peterson, W. T., and F. B. Schwing, A new climate regime in northeast Pacific ecosystems, *Geophys. Res. Let., 30*(17), 1896, 2008.

Philander, S. G., *El Nino, La Niña and the Southern Oscillation*, Academic Press Inc., 1990.

Pierce, D. W., T. P. Barnett, and M. Latif, Connections between the Pacific ocean tropics and midlatitudes on decadal timescales, *Journal of Climate, 13*(6), 1173–1194, 2000.

Ramage, C. S., Preliminary discussion of the meteorology of the El Niño, *Bulletin of the American Meteorological Society, 56*(2), 234–242, 1975.

Rasmussen, T., E. Thomsen, and L. L. Van Weering TCE, Rapid changes in surface and deep water conditions at the faeroe margin during the last 58 000 years, *Paleoceanography, 11*, 757–771, 1996.

Renold, M., 2007, *Simulations using the CCSM3 comprehensive AOGCM : Mechanisms of abrupt climate change and natural variability during the last centuries*, Ph. D. thesis, 170pp.

Renold, M., C. Raible, M. Yoshimori, and T. Stocker, Simulated resumption of the North Atlantic meridional overturning circulation - slow basin-wide advection and abrupt local convection, *Quaternary Science Reviews, 29*(1-2), 101 – 112, 2010.

Richman, M. B., Rotation of pricipal components (review article), *Journal of Climate, 6*, 293–335, 1986.

Rooth, C., Hydrology and Ocean Circulation, *Prog. Oceanogr., 11*, 131–149, 1982.

Sadler, J. C., Comments on A Study of the Southern Oscillation and Walker Circulation Phenomenon, *Monthly Weather Review, 108*(6), 825–828, 1980.

Saravanan, R., and J. C. McWilliams, Stochasticity and spatial resonance in interdecadal climate fluctuations, *Journal of Climate, 10*(9), 2299–2320, 1997.

Schmidt, M. W., M. J. Vautravers, and H. J. Spero, Rapid subropical North Atlantic salinity oscillations across Dansgaard-Oeschger cycles, *Nature, 443*, 561–564, 2006.

Schneider, N., and B. D. Cornuelle, The forcing of the Pacific Decadal Oscillation, *Journal of Climate, 18*(21), 4355–4373, 2005.

Schoennagel, T., T. T. Veblen, W. H. Romme, J. S. Sibold, and E. R. Cook, ENSO and PDO variability affect drought-induced fire occurrence in rocky mountain subalpine forests, *Ecological Applications, 15*(6), 2000–2014, 2005.

Simmons, A. J., J. M. Wallace, and G. W. Branstator, Barotropic wave propagation and instability, and atmospheric teleconnection patterns, *Journal of Atmospheric Sciences, 40*(6), 1363–1392, 1983.

Smith, R. D., and P. R. Gent, Anisotropic Gent-McWilliams Parameterization for Ocean Models, *Journal of Physical Oceanography, 34*(11), 2541–2564, 2004.

Spencer, H., R. Sutton, and J. M. Slingo, El Niño in a coupled climate model: Sensitivity to changes in mean state induced by heat flux and wind stress corrections, *Journal of Climate, 20*(10), 2273–2298, 2007.

Stocker, T. F., Past and future reorganizations in the climate system, *Quat. Sci. Rev., 19*, 301–319, 2000.

Stocker, T. F., and S. J. Johnsen, A minimum thermodynamic model for the bipolar seesaw, *Paleoceanography, 18(4)*, 1087, 2003.

Stocker, T. F., R. Knutti, and G.-K. Plattner, The future of the thermohaline circulation - a perspective, in *The Oceans and Rapid Climate Change: Past, Present, and Future*, edited by D. Seidov, B. J. Haupt, and M. Maslin, Volume 126 of *Geophysical Monograph*, pp. 277–293, Am. Geophys. Union, Washington, D. C., 2001.

Stocker, T. F., A. Timmermann, M. Renold, and O. Timm, Effects of salt compensation on the climate model response in simulations of large changes of the atlantic meridional overturning circulation, *Journal of Climate, 20*(24), 5912–5928, 2007.

Stocker, T. F., D. G. Wright, and W. S. Broecker, The influence of high-latitude surface forcing on the global thermohaline circulation, *Paleoceanogr., 7*, 529–541, 1992.

Stommel, H., Thermohaline convection with two stable regimes of flow, *Tellus, 13*, 224–241, 1961.

Stoner, A. M. K., K. Hayhoe, and D. J. Wuebbles, Assessing general circulation model simulations of atmospheric teleconnection patterns, *Journal of Climate, 22*(16), 4348–4372, 2009.

Storch, H. v., and F. W. Zwiers, *Statistical Analysis in Climate Research*, Cambridge University Press, 2002.

Stott, L., C. Poulsen, S. Lund, and R. Thunell, Super ENSO and global climate oscillations at millennial time scales, *Science, 297*, 222–226, 2002.

Stouffer, R. J., D. Seidov, and B. J. Haupt, Climate response to external sources of freshwater: North Atlantic versus the southern ocean, *Journal of Climate, 20*(3), 436–448, 2007.

Stouffer, R. J., J. Yin, J. M. Gregory, K. W. Dixon, M. J. Spelman, W. Hurlin, A. J. Weaver, M. Eby, G. M. Flato, H. Hasumi, A. Hu, J. H. Jungklaus, I. V. Kamenkovich, A. Levermann, M. Montoya, S. Murakami, S. Nawrath, A. Oka, W. R. Peltier, D. Y. Robitaille, A. Sokolov, G. Vettoretti, and S. L. Weber, Investigating the causes of the response of the thermohaline circulation to past and future climate changes, *Journal of Climate, 19*, 1365–1387, 2006.

Straus, D. M., and J. Shukla, Does ENSO force the PNA?, *Journal of Climate, 15*(17), 2340–2358, 2002.

Talley, L. D., Potential vorticity distribution in the North Pacific, *Journal of Physical Oceanography, 18*(1), 89–106, 1988.

Talley, L. D., Shallow, intermediate, and deep overturning components of the global heat budget, *Journal of Physical Oceanography, 33*(3), 530–560, 2003.

Talley, L. D., Freshwater transport estimates and the global overturning circulation: Shallow, deep and throughflow components, *Progress In Oceanography, 78*(4), 257 – 303, 2008.

Talley, L. D., Y. Nagata, M. Fujimura, T. Iwao, T. Kono, D. Inagake, M. Hirai, and K. Okuda, North Pacific intermediate water in the Kuroshio/Oyashio mixed water region, *Journal of Physical Oceanography, 25*(4), 475–501, 1995.

te Raa, L. A., G. J. Oldenborgh, H. A. Dijkstra, and S. Y. Philip, Frequency-dependent effects of the Atlantic meridional overturning circulation on the tropical Pacific ocean, *Ocean Science Discussions, 6*, 477–490, 2009.

Thompson, C. J., and D. S. Battisti, A linear stochastic dynamical model of ENSO. Part II: Analysis, *Journal of Climate, 14*(4), 445–466, 2001.

Thompson, D. W. J., and J. M. Wallace, The arctic oscillation signature in the wintertime geopotential height and temperature fields, *Geophys. Res. Let., 25*(9), 1297–1300, 1998.

Timmermann, A., S.-I. An, U. Krebs, and H. Goosse, ENSO suppression due to weakening of the North Atlantic Thermohaline Circulation, *Journal of Climate, 18*(16), 3122–3139, 2005.

Timmermann, A., F.-F. Jin, and J. Abshagen, A nonlinear theory for El Niño bursting, *Journal of the Atmospheric Sciences, 60*(1), 152–165, 2003.

Timmermann, A., Y. Okumura, S.-P. Xie, S.-I. An, A. Clement, B. Dong, R. Sutton, E. Guilyardi, A. Hu, J. H. Jungclaus, M. Renold, T. F. Stocker, R. J. Stouffer, and J. Yin, The influence of a weakening of the Atlantic meridional overturning circulation on ENSO, *Journal of Climate, 20*(19), 4899–4919, 2007.

Toniazzo, T., A study of the sensitivity of ENSO to the mean climate, *Advances in Geoscience, 6*, 111–118, 2006.

Torrence, C., and G. P. Compo, A practical guide to wavelet analysis, *Bulletin of the American Meteorological Society, 79*(1), 61–78, 1998.

Trenberth, K. E., Recent observed interdecadal climate changes in the Northern Hemisphere, *Bulletin of the American Meteorological Society, 71*(7), 988–993, 1990.

Trenberth, K. E., The definition of El Niño, *Bulletin of the American Meteorological Society, 78*(12), 2771–2777, 1997.

Trenberth, K. E., and C. J. Guillemot, *Global energy and water cycles (Chapter 7.1): Estimating evaporation-minus-precipitation as a residual of the atmospheric water budget*, Cambridge University Press, 1998.

Trenberth, K. E., B. Moore, T. R. Karl, and C. Nobre, Monitoring and prediction of the Earths climate: A future perspective, *Journal of Climate, 19*(20), 5001–5008, 2006.

Trenberth, K. E., D. P. Stepaniak, and L. Smith, Interannual variability of patterns of atmospheric mass distribution, *Journal of Climate, 18*(15), 2812–2825, 2005.

Tziperman, E., H. Scher, S. E. Zebiak, and M. A. Cane, Controlling spatio-temporal chaos in a realistic El Niño prediction model, *Phys. Rev. Lett., 79*(6), 1034–1037, 1997.

van Oldenborgh, G. J., Comments on predictability of winter climate over the North Atlantic European region during ENSO events, *Journal of Climate, 18*(14), 2770–2772, 2005.

Vellinga, M., and R. A. Wood, Global climatic impacts of a collapse of the Atlantic Thermohaline Circulation, *Clim. Change, 54*, 251–267, 2002.

Vellinga, M., R. A. Wood, and J. M. Gregory, Processes governing the recovery of a perturbed thermohaline circulation in HadCM3, *Journal of Climate, 15*, 764–780, 2002.

Vimont, D. J., The contribution of the interannual ENSO cycle to the spatial pattern of decadal ENSO-like variability, *Journal of Climate, 18*(12), 2080–2092, 2005.

Vimont, D. J., J. M. Wallace, and D. S. Battisti, The seasonal footprinting mechanism in the Pacific: Implications for ENSO, *Journal of Climate, 16*(16), 2668–2675, 2003.

Wallace, J. M., and D. S. Gutzler, Teleconnections in the geopotential height field during the Northern Hemisphere winter, *Monthly Weather Review, 109*(4), 784–812, 1981.

Wallace, J. M., and D. W. J. Thompson, The Pacific center of action of the Northern Hemisphere Annular Mode: Real or artifact?, *Journal of Climate, 15*(14), 1987–1991, 2002.

Wang, C., and S.-K. Lee, Atlantic warm pool, Caribbean low-level jet, and their potential impact on atlantic hurricanes, *Geophys. Res. Let., 34*(L02703), 5, 2007.

Wang, C., S.-K. Lee, and D. B. Enfield, Climate response to anomalously large and small atlantic warm pools during the summer, *Journal of Climate, 21*(11), 2437–2450, 2008.

Wang, Y. J., H. Cheng, R. L. Edwards, J. Y. An, C. C. Shen, and J. A. Dorale, A high-resolution absolute-dated Late Pleistocene monsoon record from Hulu Cave, China., *Science, 294*, 2345–2348, 2001.

Weaver, A. J., J. Marotzke, P. F. Cummins, and E. S. Sarachik, Stability and Variability of the Thermohaline Circulation, *Journal of Physical Oceanography, 23*, 39–60, 1993.

Weng, W., and J. Neelin, On the role of ocean-atmosphere interaction in midlatitude interdecadal variability, *Geophys. Res. Let., 25*, 167–170, 1998.

Woodgate, R. A., K. A., and T. J. Weingartner, Interannual changes in the Bering Strait fluxes of volume, heat and freshwater between 1991 and 2004, *Geophys. Res. Let., 33*, 2006.

Wu, L., F. He, Z. Liu, and C. Li, Atmospheric teleconnections of tropical Atlantic variability: Interhemispheric, tropical-extratropical, and cross-basin interactions, *Journal of Climate, 20*(5), 856–870, 2007.

Wu, L., C. Li, C. Yang, and S.-P. Xie, Global teleconnections in response to a shutdown of the Atlantic meridional overturning circulation, *Journal of Climate, 21*(12), 3002–3019, 2008.

Wu, L., and Z. Liu, Decadal variability in the North Pacific: The eastern North Pacific Mode, *Journal of Climate, 16*(19), 3111–3131, 2003.

Wu, L., Z. Liu, R. Gallimore, R. Jacob, D. Lee, and Y. Zhong, Pacific decadal variability: The tropical Pacific mode and the North Pacific mode, *Journal of Climate, 16*(8), 1101–1120, 2003.

Wu, Q., Forcing of tropical SST anomalies by wintertime AO-like variability, *Journal of Climate, 23*(10), 2465–2472, 2010.

Wunsch, C., D. Hu, and B. Grant, Mass, heat, salt and nutrient fluxes in the south Pacific ocean, *Journal of Physical Oceanography, 13*(5), 725–753, 1983.

Xie, S.-P., Y. Okumura, T. Miyama, and A. Timmermann, Influences of atlantic climate change on the tropical Pacific via the Central American Isthmus, *Journal of Climate, 21*(15), 3914–3928, 2008.

Yeager, S. G., C. A. Shields, W. G. Large, and J. J. Hack, The Low-Resolution CCSM3, *Journal of Climate, 19*, 2545–2566, 2006.

Yeh, S.-W., and B. P. Kirtman, Internal atmospheric variability and interannual-to-decadal ENSO variability in a CGCM, *Journal of Climate, 22*(9), 2335–2355, 2009.

Yoshimori, M., C. C. Raible, T. F. Stocker, and M. Renold, Simulated decadal oscillations of the Atlantic meridional overturning circulation in a cold climate state, *Clim. Dyn., 34*, 101–121, 2010.

Yukimoto, S., M. Endoh, Y. Kitamura, A. Kitoh, T. Motoi, A. Noda, and T. Tokioka, Interannual and interdecadal variabilities in the Pacific in an MRI coupled GCM, *Clim. Dyn., 12*, 667–683, 1996.

Zhang, C., Atmospheric intraseasonal variability at the surface in the tropical western Pacific Ocean, *Journal of the Atmospheric Sciences, 53*(5), 739–758, 1996.

Zhang, D., and M. J. McPhaden, Decadal variability of the shallow Pacific meridional overturning circulation: Relation to tropical sea surface temperatures in observations and climate change models, *Ocean Modelling, 15*(3-4), 250 – 273, 2006.

Zhang, R., and T. L. Delworth, Simulated Tropical response to a substantial weakening of the Atlantic Thermohaline Circulation., *Journal of Climate, 18*, 1853–1860, 2005.

Zhang, Y., J. M. Wallace, and D. S. Battisti, ENSO-like interdecadal variability: 1900-93, *Journal of Climate, 10*(5), 1004–1020, 1997.